THE UNIVERSITY *of* EDINBURGH

Towards Intelligent Mechanical Ventilation Guided by Electrical Impedance Tomography

Zhixi Zhang

A thesis submitted for the degree of Doctor of Philosophy

The University of Edinburgh

August 2022

Declaration

I hereby declare that the work presented in this thesis is my own unless otherwise acknowledged. This thesis has not been submitted for any other degree or professional qualification except to The University of Edinburgh for the degree of Doctor of Philosophy.

Zhixi Zhang

Date: 31/08/2022

Acknowledgements

First of all, I would like to express my sincere gratitude to my principal PhD supervisor, Dr. Jiabin Jia, for giving me the opportunity to work on such an exciting project, and for all his insightful guidance and support throughout my PhD research. I am grateful to him for providing me with very valuable guidance to my studies and life, and for giving me the opportunity to explore scientific research freely. His encouragement and advice played a vital role in giving me the confidence to continue my academic career when I was at a loss. None of my achievements would have been possible without his patience, help and advice. His passion for academia, the pursuit of research, and dedication to his research career have deeply influenced me. It has been the privilege of my life to work with him over the past four challenging years.

I would also like to thank my assistant supervisor, Prof. Aristides Kiprakis, for all of his guidance and suggestions in control engineering. I will never forget his valuable advice for my research topics. I have learned a lot from his profound knowledge of control systems and instrumentation.

In addition, I am grateful to all current and previous Agile Tomography Group colleagues, especially Dr. Hancong Wu, Dr. Yuan Chen, Hao Yu, Delin Hu, Zhou Chen for their kind encouragement and assistance in both my academic and personal lives. Thank you for brightening my life.

Last but most importantly, I would like to express my deepest thanks and best wishes to my parents. Thank you for always encouraging and supporting me, giving me the confidence to face difficulties. It is your selfless love and support that enable me to go through hard times, pursue my dreams, and surpass myself. Finally…

...to my father Mr Lizhi Zhang and my mother Mrs Junfeng Ma...

Lay Summary

Electrical impedance tomography (EIT) is an imaging technique that allows the monitoring of conductivity distribution in confined spaces. Compared to other imaging techniques, EIT has the advantages of being non-invasive, low cost, easily portable, high temporal resolution and no radiological side effects. Therefore, it is widely used in medical imaging, such as monitoring lung ventilation, functional brain imaging and breast cancer screening. The aim of this thesis is to validate the feasibility of EIT in guiding mechanical ventilation towards an intelligent medical device. Mechanical ventilation is a technical modality that can effectively control or replace a person's normal physiological breathing in order to increase ventilation and improve respiratory function. However, during long-term use, ventilator-induced lung damage may further lead to acute respiratory distress syndrome. Around this critical challenge, this thesis develops a new method for long-term, real-time monitoring of lung tidal volume and control of mechanical ventilation based on EIT. The analysis of the device is demonstrated in terms of high-resolution image reconstruction algorithms, control system design and the development of a feedback system for models with different characteristics. The results of this thesis help to advance the development of intelligent new medical devices in monitoring and control technology.

Table of contents

Abstract

Mechanical ventilation (MV) occupies a critical position in the field of modern clinical medicine. MV is an effective mean to artificially replace, control, or change spontaneous breathing movement and ventilation function. Therefore, it has been widely used in respiratory failure caused by various reasons, breathing management of anesthesia during major surgery, supportive respiratory care and emergency resuscitation. However, most the traditional ventilators can only provide one-dimensional information such as pressure. Such comprehensive information cannot analyze the local lung injury.

Electrical impedance tomography (EIT) is a very promising imaging technique. After the electric field is applied, the induced boundary voltages can be measured to image the spatial conductivity distribution of the sensing region bounded by electrodes. EIT has the advantages of high speed, high temporal resolution, low-cost, non-invasive, and radiation-free, etc., which makes it arouse wide attention and interest in the field of biomedical imaging. Well-studied biomedical clinical applications of EIT include breast and prostate cancer screening, functional brain imaging, thoracic imaging, and lung ventilation monitoring. Therefore, it shows excellent potential in organ characterization, where experimental samples have the same electrical properties as tissues of the human body. This PhD work mainly explores the possibility of more emerging biomedical applications of EIT in pulmonary ventilation monitoring.

The combination of EIT and ventilator realized real-time pulmonary monitoring and control, expanded the dimension of useful information and clearly saw the volume change of the lung, which could help doctors better analyze the quality of lung function. This work aims to construct a novel and intelligent EIT-guided mechanical ventilation modality, to evaluate the possibility of this medical device qualitatively and quantitatively, and to improve its performance in real-time 3D monitoring. Around this topic, the contributions of this thesis can be summarized from the aspects of

mechanical ventilation system combined with ultrasonic sensor design, real-time and effective EIT reconstruction algorithm for monitoring respiratory status, EIT-based automated ventilation system and deep learning-based EIT reconstruction algorithm.

A control system study was first developed to complete a single-variable-controlled mechanical ventilation device. Firstly, three-dimensional lung imaging was studied through single-layer electrodes. Compared to traditional algorithms, this 3D algorithm proposed in the work achieved a correlation coefficient of 0.8. In addition, the tidal volume information was extracted from the 2D and 3D reconstructed images as the feedback input of the control system to realize closed-loop control. The simulation has been implemented and the results show that the error is controlled to within 3%. In the work, an active disturbance rejection control method with excellent anti-interference ability was designed to improve the stability of the system. According to the simulation results, the rise time of the system can be improved by 12.8%. At the same time, the error of the experimental results can be reduced by 22.2%. The evaluation results show that the proposed EIT-guided MV system is a powerful tool for real-time 2D and 3D biomedical imaging. The quality of tomographic images is vital for qualitative or quantitative analysis in biomedical applications. Finally, in order to achieve high-quality conductivity imaging, two deep learning-based image reconstruction algorithms were proposed. The RP-UNet algorithm has a structural similarity of 96.99% and a correlation coefficient of 97.27%. The proposed algorithm exhibits excellent spatial resolution and better noise reduction performance in reconstructed images. In conclusion, the work presented in this thesis validates the feasibility of the proposed image reconstruction algorithm using the developed EIT-guided mechanical ventilation system. It also demonstrates the potential of EIT for biomedical research and medical devices.

List of Figures

List of Tables

Abbreviations

1D, 2D, 3D	1 Dimensional, 2 Dimensional, 3 Dimensional
ADC	Analog-to-Digital Converter
ADRC	Active Disturbance Rejection Control
ALI	Acute Lung Injury
APT	Applied Potential Tomography
ARDS	Acute Respiratory Distress Syndrome
BI	Batch Normalization
BI-EIM	Breast Imaging-Electrical Impedance Mammography
CC	Correlation Coefficient
CEM	Complete Electrode Model
CG	Conjugate Gradient
CT	Computerised Tomography
dB	Decibel
DSA-UNet	Depthwise Separable Convolution Self Attention UNet
DSC	Depthwise Separable Convolution
FC	Fully Connection
EELV	End-Expiratory lung Volume
EIT	Electrical Impedance Tomography
FEM	Finite Element Method

fMRI	Functional Magnetic resonance imaging
FPGA	Field Programmable Gate Arrays
GI	Global Inhomogeneity
ICU	Intensive Care Units
LADRC	Linear Active Disturbance Rejection Control
LBP	Linear Back-Projection
LESO	Linear Extended State Observer
LoG	Laplacian of Gaussian
LPV	Lung Protective Ventilation
LSEF	Linear State Error Feedback
MAT	Mean absolute error
MIT	Magnetic Induction Tomography
MRI	Magnetic resonance imaging
MV	Mechanical Ventilation
NRDS	Neonatal Respiratory Distress Syndrome
PEEP	Positive End-Expiratory Pressure
PID	Proportion Integration Differentiation
RE	Relative Errors
PCV	Pressure Control Ventilation
PSA	Parallel Polarized Self Attention

RM	Recruitment
ROIs	Regions of Interest
RP-UNet	RepVGG Parallel Polarized Self Attention UNet
SNR	Signal to Noise Ratio
SSIM	Structure Similarity Index Measure
SV	Stroke Volume
TV	Total variation
UART	Asynchronous Receiver/Transmitter
UNet	U-shape Network
VCV	Volume Control Ventilation
VILI	Ventilator-Induced Lung Injury
VT	Tidal Volume

List of symbols

u	Electric potential
$\boldsymbol{\Omega}$	Connected domain
$\boldsymbol{n}$	The unit normal vector
S	Boundary
$\boldsymbol{J}$	Current density
$\boldsymbol{\phi}$	Electric potential of the boundary
l	Total number of electrodes
E_i	The i^{th} electrode
z_i	The contact impedance of the i^{th} electrode
U_i	Electrical potential
I_i	Injected current
V	Measured electrode potentials
F	Nonlinear forward operator
$\boldsymbol{e}$	Additive noise and measurement error
ΔV	Change of the boundary voltage measurement
$\boldsymbol{\sigma}$	Conductivity
$\Delta\boldsymbol{\sigma}$	Conductivity distribution vector
$\boldsymbol{J}$	System sensitivity matrix (the Jacobian matrix)
$\boldsymbol{J}_{mn}(x, y)$	Sensitivity value at pixel (x, y)

R	Regularisation function incorporating a priori knowledge
λ	Regularisation parameter
$\boldsymbol{I}$	Identity matrix
$\boldsymbol{L}$	Four-connected region second-order Laplacian operator matrix
$\boldsymbol{\Phi}$	Orthogonal matrix
$\boldsymbol{a}$	Coefficient vector
$\|\Delta\boldsymbol{\sigma}\|_{TV}$	TV norm of the conductivity variation distribution
P	Number of pixels
φ	Potential distribution
$\Delta\widehat{\boldsymbol{\sigma}}_k$	Reconstructed variation of conductivity
$\Delta\boldsymbol{\sigma}_k$	True conductivity
$\boldsymbol{\mu}_m$	Mean of conductivity of reconstructed image
$\boldsymbol{\mu}_n$	True conductivity value
k^2	Kernel size
h	Height
w	Width
D	Distance
C	Number of the output node
z_i	Output value of i^{th} node
L_{MSE}	Loss function of the DSA-UNet

K	Number of real conductivities
σ_{pred}	Estimated conductivity under the DSA-UNet
σ_{max}	Maximum conductivity of the reconstructed image
σ_{min}	Minimum conductivity
σ_{ave}	Average conductivity of the valid pixel
v	Speed of ultrasonic waves at room temperature
t	Time difference between emission and reception
N	Number of flips per second
n_c	Number counted by counter
C_{Air}	Speed of ultrasonic
T_c	Room temperature in Celsius degree (by default, 25 Celsius degree)
D	Distance between water surface to the ultrasound sensor
V_{lung}	Estimated volume of lung
A_{lung}	Estimated valid area of the cross-section of the lung
N_{pixel}	Total number of the valid pixel according to the threshold
h_{lung}	Height of the lung
z	Reference signal
ω_c	Bandwidth of the controller
b_0	Control gain of the system

$f(t)$	Disturbance to the system
V	Tidal volume
Q	Inspiratory flow
Q_{pat}	Airflow into the lungs
Q_{out}	Airflow out from the blower
Q_{leak}	Airflow leaked from connection hose
p_{out}	Output pressure of the blower
p_{aw}	Airway pressure in the hose
p_{lung}	Pressure in the lung
R_0	Residence of the hose before the airflow get into four lungs
R_{hose}	Resistance of hose
R_{lung}	Resistance before the inspiratory flow get into the lung
y_i	Actual output tidal volume data
x_i	Ideal reference data
n	Number of total data

Publication List

Journal papers

1. H. Yu, **Z. Zhang**, Y. Gao and J. Jia, "Multiscale Voltage Reconstruction with Attention-Based Network for Volume Fraction Prediction of Industrial Oil–Water Two-Phase Flow by EIT," in IEEE Transactions on Instrumentation and Measurement, vol. 71, pp. 1-9, 2022

2. **Z. Zhang**, J. Jia, "RP-UNet for Fast Lung Imaging Based on Electrical Impedance Tomography," in IEEE Transactions on Biomedical Engineering (to be submitted)

3. H. Yu, X. Wan, Z. Dong, **Z. Zhang**, J. Jia, “Estimation of Reference Voltages for Time-difference Electrical Impedance Tomography" in IEEE Transactions on Instrumentation and Measurement, vol. 71, pp. 1-10,2022

Conference papers

4. **Z. Zhang**, H. Yu, and J. Jia, "Deep Learning for Lung Imaging Based on Electrical Impedance Tomography," presented at *the BioMedEng22*, University College London, London, UK, 2022

5. **Z. Zhang**, H. Yu, and J. Jia, "3D Mechanical Ventilation Control System Based on Electrical Impedance Tomography," presented at *the International Conference on Bioelectromagnetism, Electrical Bioimpedance, and Electrical Impedance Tomography*, Kyung Hee University, Seoul, Korea, 2022

6. **Z. Zhang**, H. Yu, and J. Jia, "Control Strategies of EIT-Guided Mechanical Ventilation," presented at *the Global 10th World Congress on Industrial Process Tomography*, Virtual, 2021

7. **Z. Zhang**, H. Yu, and J. Jia, "Mechanical Ventilation Control System

Guided by Electrical Impedance Tomography," presented at *International Conference on Biomedical Applications of Electrical Impedance Tomography*, National University of Ireland Galway, Galway, Ireland, 2021

8. H. Yu, **Z. Zhang**, and J. Jia, "Light-weight CNNs with Dynamic Convolution for Lung EIT," presented at *the International Conference on Bioelectromagnetism, Electrical Bioimpedance, and Electrical Impedance Tomography*, Kyung Hee University, Seoul, Korea, 2022

Chapter 1 Introduction

1.1 Background and motivation

The ventilator is an essential medical device used to increase the pulmonary ventilation, reduce the consumption of the respiratory function, maintain normal physiological breathing of a patient, and improve the respiratory function. As an effective mean of artificial replacing spontaneous ventilation, the ventilators have been widely used in the following three fields:

a) Respiratory failure caused by respiratory diseases: such as chronic obstructive pneumonia, pulmonary infection, asthma, etc.

b) Surgery: including respiratory management during anesthesia for major surgery, ventilation support during and after pediatric surgery, etc.

c) Sleep apnea: such as snoring, sleep-disordered breathing, etc.

The current ventilation mainly replies on open-loop control methods of pressure or volume, which obtains one-dimensional information through sensor measurement for the doctors to adjust the equipment manually. However, the one-dimensional information obtained does not provide a visual representation of the location and extent of the injured lung. Furthermore, the open-loop system is also unable to change the control strategy in real time depending on the patient's condition, which may further affect the condition. At the same time, it is impossible to observe tidal volume changes in the lungs in real-time.

Appearing in the early 1980s [1, 2], electrical impedance tomography (EIT) is an electrical tomography imaging modality that allows the non-invasive visualization of absolute values or changes in electrical conductivity within a region of interest [3-6]. Due to its high-speed, non-radiative, and non-invasive

sensing capabilities, EIT has been widely used in medical process imaging in recent years to estimate key process parameters or capture rapidly changing phenomena, such as images capturing the moment of brain unconsciousness and monitoring changes in lung ventilation and brain activity.

Real-time EIT was used to influence pulmonary protective ventilation in an animal model of acute respiratory distress syndrome [7]. The study was conducted using electrical impedance tomography-derived variables to improve the outcome of acute lung injury. Electrical impedance tomography-guided ventilation improved respiratory mechanics, gas exchange, and reduced histological evidence of ventilator-induced lung injury. Thus, EIT-Ventilator is a form of lung protective ventilation (LPV) that protects the lung from injury [8]. However, this study relied heavily on CT images as an adjunct to EIT, as it is difficult to detect the contours and precise deformation of the lung with little visualization of EIT imaging results. What is more, in this study, it was the positive end-expiratory pressure (PEEP) values that were altered by recruitment, which did not really form a complete closed control loop. More importantly, the process of controlling pressure can easily result in an uneven distribution of tidal volume, which may further affect lung injury.

Although the progress of EIT to date is encouraging, the following limitations must still be overcome before it can be used in practical applications, particularly in medical scenarios:

a) In comparison to other tomography modalities, such as computed tomography (CT), EIT is application scope is enhanced by its high temporal resolution, such as about 1000 frames per second [4], but constrained by its comparatively low spatial resolution, such as 10% of the sensor diameter [9].

b) In addition, in order to generate information-rich tomographic images in real-time, high-resolution and fast image reconstruction algorithms are required.

c) Furthermore, a visual ventilator that can be automatically adjusted is required to achieve a greater degree of intelligence and reduce medical costs, for example, the number of doctors and the price of medical equipment.

1.2 Aims and objectives

The main goal of this thesis is to explore and develop the EIT technique for medical applications, especially the monitoring of wearable medical devices such as mechanical ventilation. Precisely, it is mainly dedicated to developing a digital technology based, fast, adaptable, reliable and real-time closed-loop control system and image reconstruction method. Furthermore, it could be used to real-time monitoring of tidal volume changes in the lung and the injury condition of different regions of the lung under different kinds of breathing cases. In order to achieve the primary targets, the following objectives are established:

- Research on novel 2D/3D image reconstruction algorithms based on time or frequency difference measurement data for efficient reconstruction of conductivity changes in irregularly shaped objects, which are the main reconstruction targets encountered in medical mechanical ventilation systems.

- Numerical and experimental studies are carried out on real-time monitoring of lung breathing cycles from the perspective of the position, shape, and health of the detected object.

- Advanced EIT-guided mechanical ventilation device platform implementation, with configurable electrodes, controllable excitation mode, programmable control system, real-time, stable and accurate capture of continuous lung dynamics; in addition, real-time control tidal volume based on feedback closed loop.

1.3 Main contributions

This thesis provides pioneering research on the development and optimisation of EIT-Ventilator for intelligent monitoring and controlling. The main contributions of this thesis are summarised as follows:

- The closed control system can track the breathing state in real-time, which will use the EIT image as a feedback signal, to visually observe the volume changes of lungs. When the patient uses a ventilator, the pressure will affect the shape of the lung regardless of whether the patient is lying flat or on the side, which may cause lung damage. However, the system in this project can clearly distinguish the lungs from injury, and confirm the damaged area and location.

- By adjusting the state of the ventilator in time, it is possible to reduce or control the damage to the lungs. Real-time 3D reconstruction images can be realized by following changes of the lung breathing cycle.

- An Active Disturbance Rejection Control (ADRC) method with excellent anti-interference ability is designed to improve the stability of the system. The evaluation results show that the proposed EIT-guided MV system is robust.

- Two deep learning image reconstruction algorithms are also proposed to obtain high-quality conductivity imaging. The proposed algorithms show better spatial resolution and better denoising performance in the reconstructed image. These properties are urgently needed in biomedical imaging.

.

1.4 Overview of the thesis

The thesis is composed of seven chapters and the remaining part is structured as follows:

Chapter 1 provides background on lung disease and mechanical ventilators. In the meanwhile. The potential challenges in the measurements using EIT are discussed. After that, the primary motivation and contribution of this thesis are shown. Finally, a brief structure of this thesis is listed.

First of all, an introduction about the historical background and development of EIT is presented in Chapter 2. Then, EIT theory as well as EIT system including different measurement modalities are reviewed. After that, the conventional image reconstruction algorithms for EIT are discussed. In addition, the applications of EIT in the medical field are summarised. On the other hand, lung diseases and some special scenarios requiring ventilators are presented. The traditional control strategy of mechanical ventilation for different patients is discussed. Their pros and cons are reviewed. The common methods based on tomography for lung monitoring are briefly introduced. Finally, different methods for lung monitoring in literature and this thesis are compared.

In chapter 3, the image reconstruction algorithm is updated from 2D to 3D. Excitation is added to the electrodes in the center layer, and image reconstruction is performed on multiple layers to obtain a three-dimensional image. And the optimal parameter settings, such as the number of iterations, are discussed. This imaging approach paves the way for the implementation of an EIT-guided mechanical ventilation device in Chapter 6 and can be used to monitor the tidal volume of the lungs in real time.

In chapter 4, the main purpose is to optimize the reconstructed image of the EIT through machine learning methods, which makes the EIT images have a higher resolution and more accurate. Two different deep learning based models of UNet are presented to improve the performance of the network, and

enhance the resolution of the reconstructed images as well as the speed of imaging. This chapter will also show the results of lung damage detection, where three different diseases are reconstructed in the lung, including pneumothorax, pulmonary oedema and pleural effusion.

In Chapter 5 an ultrasound-based hardware control system has been developed and a complete closed-loop control system is demonstrated. In the experiment, the lung was mimicked by a balloon, while the trachea was replaced by a syringe, and the chest cavity was replaced by a cylindrical water tank. The volume change in the balloon can be measured by the drainage method. Ultrasound sensor can measure the rising height of the water surface to calculate the volume change, which is fed back to the control system as a feedback signal. This section's analyses the feasibility of a volume-based control strategy for mechanical ventilation systems with ultrasound sensor.

In Chapter 6, a closed-loop control system for mechanical ventilation is implemented using EIT image results as feedback, which is the first time that a closed-loop system based on volume control has been proposed and validated combined with EIT. The automation of mechanical ventilation can be further improved by connecting the EIT system to the control system as a feedback loop. Two reconstruction algorithms to estimate volume based on EIT are presented and compared. The results show that the EIT can monitor the changes of tidal volume in real time and has the ability to act as a feedback loop to the control system. Furthermore, repeated validation and analysis of different breathing conditions and lung models demonstrate the generality and robustness of the system.

Chapter 7 summarizes the main findings of this thesis and discusses the limitation of the research. The potential work for the future is also discussed based on the novel developments produced in the thesis.

Chapter 2 Literature review

2.1 Introduction

As mentioned in the introduction chapter, EIT has a wide range of applications, mainly in clinical medicine and industrial fields. In medical applications, there are mainly lung imaging, brain injury detection, bioimpedance analysis, breast cancer screening and so on. In 1989 Eyuboglu [10] demonstrated that EIT was sensitive enough to monitor pulmonary blood flow because it could detect changes in tissue conductivity brought on by blood perfusion. Current applications include imaging of relative changes in cerebral blood volume during aortic arch replacement surgery [11], local lung perfusion analysis [12], non-contact magnetic induction tomography (MIT) [13] and many other aspects. In this chapter, the foundation and principles of EIT will be introduced, as an emerging technique. On this basis, the EIT system used in the experiment will be introduced and different image reconstruction algorithms will be reviewed. Furthermore, mechanical ventilation is comprehensively introduced from the perspective of the principles of control, the mathematical calculation and the lung diseases. Finally, there is a brief introduction of existing EIT medical applications.

2.2 Review of EIT

2.2.1 Foundation of EIT

The principle of EIT is to use the boundary measurement data to solve the internal conductivity distribution function of the object. In the measurement, current is injected into the object through electrodes added to the surface of the object, and the voltage distribution on the surface of the object is measured,

and then the reconstruction algorithm is used to obtain the internal conductivity distribution of the object. For example, in the direction of medical imaging technology, different tissues of the human body have different conductivities. When certain tissues are diseased, the resistivity will also change accordingly. Therefore, according to the different electrical conductivity of different human body tissues under different physiological and pathological conditions. Various methods are used to apply safe excitation current or voltage to the human body, and the internal conductivity distribution or the image of conductivity's change of the human body is reconstructed through the measurement response information of the excitation current or voltage in the human body. According to Maxwell's equations, assuming that at low frequencies and small field strengths, an approximate conductivity equation can be obtained, as shown in Equation 2.1.

$$\boldsymbol{\nabla} \cdot \big(\sigma(x,y)\boldsymbol{\nabla} u(x,y)\big) = 0, (x,y) \in \boldsymbol{\Omega} \tag{2.1}$$

where σ denotes the conductivity inside $\boldsymbol{\Omega}$, and u is the electric potential inside Ω, Ω is a simple connected domain.

The Neumann boundary condition, as shown in Equation 2.2, and the Dirichlet boundary condition, as shown in Equation 2.3 are commonly applied associated with Equation 2.1, in order to deliver a unique solution, based on the Complete Electrode Model (CEM) [5]. CEM is the most accurate electrode model for EIT, which can be realised physically. However, on the surface of the excited motor, the current density injected into the field through the electrode surface is unknown, so its integral form is required. According to Equation 2.1, the other equations of CEM are given by Equation 2.4:

$$\sigma \nabla \boldsymbol{\phi} \cdot \boldsymbol{n}|_S = \sigma \frac{\partial \boldsymbol{\phi}}{\partial \boldsymbol{n}}|_S = \boldsymbol{J} \tag{2.2}$$

where $\boldsymbol{n}$ denotes the unit normal vector of the boundary S, $\boldsymbol{J}$ is the current density, and $\boldsymbol{\phi}$ is the electric potential of the boundary.

$$\phi|_S = U \tag{2.3}$$

where s is the field boundary.

$$u + z_i \sigma \frac{\partial u}{\partial n} dS = U_i \text{ (on the electrode } E_i, i = 1,2, \dots, l) \quad (2.4a)$$

$$\int_{E_i} \sigma \frac{\partial u}{\partial n} dS = I_i \text{ (on the electrode } \mathrm{E_i}, \mathrm{i} = 1,2, \dots, l) \quad (2.4b)$$

$$\sigma \frac{\partial u}{\partial n} = 0 \ (between\ electrodes) \quad (2.4c)$$

where l denotes the total number of electrodes and E_i is the i^{th} electrode. z_i stands for the contact impedance of the i^{th} electrode. U_i and I_i represent respectively the electrical potential and injected current on the i^{th} electrode. n denotes the unit norm vector.

Based on Kirchhoff's law, the current injected to the sensing area and the boundary voltages on the electrodes would follow the following rules:

$$\sum_{i=1}^{i} I_i = 0 \quad (2.5a)$$

$$\sum_{i=1}^{i} U_i = 0 \quad (2.5b)$$

For some physical processes or phenomena, if the distribution of the physical process is known, the change law of the entire system state variable can be determined according to certain specific conditions of the system state variable, which is called the forward problem. The relation between the conductivity inside the simple connected domain and the boundary voltages on the electrodes can be further described by the nonlinear deterministic observation model, as shown in the Equation 2.6.

$$\boldsymbol{V} = F(\boldsymbol{\sigma}) + \boldsymbol{e} \quad (2.6)$$

where V represents the measured electrode potentials, F stands by the nonlinear forward operator and e represents the additive noise and measurement error.

The approximate linearized relationship between the voltage measurement and the conductivity distribution is:

$$\Delta \boldsymbol{V} \approx \boldsymbol{J} \Delta \boldsymbol{\sigma} \tag{2.7}$$

where $\Delta \boldsymbol{V}$ is the change of the boundary voltage measurement, and $\Delta \boldsymbol{\sigma}$ is the small conductivity distribution vector. $\boldsymbol{J}$ denotes the system sensitivity matrix (the Jacobian matrix) that maps the voltage measurement with the conductivity distribution, which can be calculated by the Equation 2.8.

$$\boldsymbol{J}_{mn}(x, y) = \frac{\partial \boldsymbol{V}_{mn}}{\partial \boldsymbol{\sigma}_k} = -\int_{pixel\,k} \nabla \boldsymbol{u}(I^m) \cdot \nabla \boldsymbol{u}(I^n) dV \tag{2.8}$$

where $\boldsymbol{J}_{mn}(x, y)$ is sensitivity value at pixel (x, y) when electrode pairs m and n are selected as current injection and measurement electrodes respectively. $\boldsymbol{u}(I^m)$ and $\boldsymbol{u}(I^n)$ are the electrical potential distribution in the simple connected domain when the m^{th} and n^{th} electrode pairs are selected as current injection electrodes, respectively.

2.2.2 EIT system

The EIT equipment used in this article is designed by Yang et al. [14], which is a real-time online image reconstruction system [15]. It is mainly divided into three parts, namely EIT sensor, hardware acquisition and processing equipment, and imaging software, as shown in Figure 2-1. The main box is utilized for current injection and voltage measurement and there is a configurable multiplexer array for electrode switching. In addition, there is a medical power supply with safety isolation. The last part is a 2D/3D imaging software for real-time image reconstruction and data storage.

Figure 2-1: The EIT system.

The main box includes an adjustable multi-frequency current source to generate two discrete sinusoidal waveforms with different frequencies from 10 kHz to 1 MHz and two Analog-to-Digital Converter (ADC) to perform the data acquisition simultaneously. The maximum amplitude of the simulating current is 10 mA peak to peak in order to minimize the side effect on the objects under test.

The configurable multiplexer array is composed of a 32-channel switch array board. In the switch array board, there are 32 dual single pole single throw switches for current injection switching and two cascaded 8*16 crosspoint switch array to switch the voltage measuring electrode pairs. The switches are controlled by the imaging software based on the measurement principle of EIT.

A 2D/3D imaging software, Visual Tomography, is developed for system control, image reconstruction and data analysis. It includes a control panel to set the sensing mode and sensing parameters, in addition, there is a window to show the data or reconstructed images for the current measurement. The online image reconstruction is performed with a default sensitivity map and Tikhonov regularization method, which are already programmed in the software. For the further analysis with different sensitivity matrix or advanced reconstruction algorithms, the data can be logged to the computer in text files.

The frame rate is obtained based on a 16-electrode EIT sensor for the 2D cases (there were 104 independent measurements in a full scan). The maximum frame rate achieved by the serial mode is 546 frames per second (fps) at 625 kHz. Up to 1014 fps imaging could be supported by using the semi-parallel mode.

2.2.3 Image reconstruction algorithm

The image reconstruction of EIT is a typical inverse, ill-conditioned and ill posed problem, which attempts to inverse the forward problem to estimate the conductivity distribution from the boundary voltage vectors and the sensitivity matrix [16]. In-depth analyses of EIT image reconstruction issues have been described in recent years with regard to the improvement of image quality. Reviews in the literature provide an excellent summary of some of the most well-known EIT image reconstruction algorithms [3, 5, 14]. Below, a brief review of the image reconstruction algorithms is provided.

a) Tikhonov regularization

Based on the approximated linearized EIT model mentioned in Equation 2.7, the conductivity variation can be estimated by solving the constrained optimization problem or the equivalent unconstrained optimization problem, which is shown in Equation 2.9.

$$\Delta\boldsymbol{\sigma}_{reg} = arg_{\Delta\boldsymbol{\sigma}} \min\left\{\frac{1}{2}\|\boldsymbol{J}\Delta\boldsymbol{\sigma} - \Delta\boldsymbol{V}\|_2^2 + \lambda R(\Delta\boldsymbol{\sigma})\right\} \tag{2.9}$$

where R represents the regularisation function incorporating a priori knowledge, λ denotes the regularisation parameter.

Tikhonov regularization is one of the most commonly used methods for image reconstruction in EIT. The incorporation of the regularization term is based on the knowledge that the noise is dominated by high-frequency components with large amplitudes. According to Tikhonov regularization, the Equation 2.10 can be obtained as follow:

$$\Delta\boldsymbol{\sigma}_{reg} = arg_{\Delta\boldsymbol{\sigma}} \min\left\{\frac{1}{2}(\|\boldsymbol{J}\Delta\boldsymbol{\sigma} - \Delta\boldsymbol{V}\|_2^2 + \lambda\|\Delta\boldsymbol{\sigma}\|_2^2)\right\} \quad (2.10)$$

which can be calculated as:

$$\Delta\boldsymbol{\sigma}_{reg} = (\boldsymbol{J}^T\boldsymbol{J} + \lambda\boldsymbol{I})^{-1}\boldsymbol{J}^T\Delta\boldsymbol{V} \quad (2.11)$$

where $\boldsymbol{I}$ is the identity matrix.

The well-known single step Tikhonov regularization can be improved by introducing the Laplacian of Gaussian (LoG) [17] filter to the additional term to reduce the fringe effect in the reconstructed image, which is demonstrated in Equation 2.12:

$$\Delta\boldsymbol{\sigma}_{reg} = arg_{\Delta\boldsymbol{\sigma}} \min\left\{\frac{1}{2}(\|\boldsymbol{J}\Delta\boldsymbol{\sigma} - \Delta\boldsymbol{V}\|_2^2 + \lambda\|\boldsymbol{L}\Delta\boldsymbol{\sigma}\|_2^2)\right\} \quad (2.12)$$

which can be explicitly calculated as:

$$\Delta\boldsymbol{\sigma}_{reg} = (\boldsymbol{J}^T\boldsymbol{J} + \lambda\boldsymbol{L}^T\boldsymbol{L})^{-1}\boldsymbol{J}^T\Delta\boldsymbol{V} \quad (2.13)$$

where $\boldsymbol{L}$ is the four-connected region second-order Laplacian operator matrix [17].

b) Total variation (TV) regularization

Nonlinear iterative algorithms propose to iteratively find the global minimum of the objective function. At each step, the estimated conductivity distribution is updated to reduce the residual of the objective function until it meets the criteria. The common iterative regularizations are l1 regularization (or sparsity regularization) [18] and TV regularization [19].

Sparsity regularization is based on the knowledge that the conductivity distribution inside the sensing domain is sparse, which means most of the element are zero in the spatial or frequency domains [20]. This priori knowledge can be used to promote non-zero coefficients and suppress the

small noise in the estimated results. During the EIT image reconstruction, the function can be obtained:

$$\Delta\boldsymbol{\sigma}_{reg} = arg_{\Delta\boldsymbol{\sigma}} \min\left\{\frac{1}{2}(\|\boldsymbol{J}\Delta\boldsymbol{\sigma} - \Delta\boldsymbol{V}\|_2^2 + \lambda\|\boldsymbol{\Phi}^T\Delta\boldsymbol{\sigma}\|_l)\right\} \tag{2.14}$$

where $\Delta\boldsymbol{\sigma} = \boldsymbol{\Phi}\boldsymbol{a}$ and $\boldsymbol{a} = \boldsymbol{\Phi}^{-1}\Delta\,\boldsymbol{\sigma} = \boldsymbol{\Phi}^T\Delta\boldsymbol{\sigma}$, given $\boldsymbol{\Phi}$ is an orthogonal matrix, $\boldsymbol{a}$ denotes the sparse coefficient vector of the conductivity distribution under **a** certain basis $\boldsymbol{\Phi}$.

On the basis of several thoroughly researched techniques, including basis pursuit denoise methods, the Equation 2.14 can be solved effectively [21] and the least absolute selection and shrinkage operator [22].

TV regularization is another widely used iterative regularization algorithm for EIT image reconstruction [23-25].The introduction of the TV regular term makes it possible to limit the total variation to the minimum while obtaining the best image. Therefore, the horizontal or vertical boundary in the image will be well maintained. Use the TV regularization model to denoise, the effect is better and less blur. This is achieved by introducing the integral of the absolute gradient of the conductivity distribution to the original objective function as a regularization term.

$$\Delta\boldsymbol{\sigma}_{reg} = arg_{\Delta\boldsymbol{\sigma}} \min\left\{\frac{1}{2}(\|\boldsymbol{J}\Delta\boldsymbol{\sigma} - \Delta\boldsymbol{V}\|_2^2 + \lambda\|\Delta\boldsymbol{\sigma}\|_{TV})\right\} \tag{2.15}$$

where $\|\Delta\boldsymbol{\sigma}\|_{TV}$ is the TV norm of the conductivity variation distribution.

$$\|\Delta\boldsymbol{\sigma}\|_{TV} = \sum_{x,y}\sqrt{\left(D_{x,y}^{v}(\Delta\boldsymbol{\sigma})\right)^2 + \left(D_{x,y}^{h}(\Delta\boldsymbol{\sigma})\right)^2} = \|\nabla(\Delta\boldsymbol{\sigma})\|_l \tag{2.16}$$

where (x, y) represents the coordinate of a pixel inside domain. $D_{x,y}^{v}(\Delta\boldsymbol{\sigma})$ and $D_{x,y}^{h}(\Delta\boldsymbol{\sigma})$ are the derivatives of $\Delta\boldsymbol{\sigma}$ along the vertical and horizontal directions, respectively, as demonstrated below:

$$D_{x,y}^{v}(\Delta\boldsymbol{\sigma}) = \begin{cases} \Delta\boldsymbol{\sigma}_{x,y} - \Delta\boldsymbol{\sigma}_{x,y+1} & 1 \le y < P_v \\ 0 & y = P_v \end{cases} \tag{2.17}$$

$$D_{x,y}^{h}(\Delta\boldsymbol{\sigma}) = \begin{cases} \Delta\boldsymbol{\sigma}_{x,y} - \Delta\boldsymbol{\sigma}_{x+1,y} & 1 \le x < P_h \\ 0 & y = P_h \end{cases} \tag{2.18}$$

where P_v and P_h are the number of pixels in each direction respectively.

c) Conjugate Gradient Method

The Conjugate Gradient method is a method between the steepest descent method and the Newton method. It only needs to use the first-order derivative information, but it overcomes the shortcomings of the slowest convergence of the steepest descent method, and avoids the need to store and calculate the Hesse matrix and invert problem for the Newton method. The conjugate gradient method is not only one of the effective methods for handling big linear equations, but it is also one of the strongest nonlinear optimization algorithms.

2.3 Mechanical ventilation

When the patient's natural ventilation and oxygenation function are impaired, mechanical ventilation is a life-sustaining therapy for the patients with acute respiratory failure. It is a quite common modality in intensive care units (ICU) to restore effective ventilation and improve oxygenation, and indeed the advent of its use heralded the dawn of modern ICU. Since the ARDSNet investigators published a landmark article in the New England Journal of Medicine 15 years ago that emphasised the significance of a lung-protective ventilation strategy, interest in mechanical ventilation has substantially enhanced from both a research and a clinical perspective [26].

2.3.1 Lung diseases

Acute respiratory distress syndrome (ARDS) is a clinical syndrome caused by intrapulmonary and/or extrapulmonary causes and is characterized by refractory hypoxemia. It has attracted much attention due to its high mortality. The main indications are diseases dominated by ventilation dysfunction,

including obstructive ventilation dysfunction, such as acute exacerbation of chronic obstructive pulmonary disease, acute exacerbation, etc., and restrictive ventilation dysfunction, such as neuromuscular disease, interstitial lung disease, thoracic deformities, etc., and diseases mainly due to ventilation dysfunction. Mechanical ventilation is the mainstay of treatment for patients with acute respiratory distress syndrome. According to the different methods of mechanical ventilation, it can be divided into non-invasive ventilation and invasive ventilation. Non-invasive ventilation relies on mask ventilation, while invasive ventilation relies on tracheal intubation or tracheostomy tube for ventilation, so the choice of the two depends on the specific condition to determine the timing. At present, mechanical ventilation strategies for patients with acute respiratory distress syndrome mainly include the following: lung-protective ventilation strategies (low tidal volume ventilation, pressure-limited ventilation, permissive hypercapnia, inverse proportional ventilation, PEEP application etc.), lung opening strategies (specific techniques include: lung recruitment, optimal PEEP application and selection of mechanical ventilation modes, etc.), and mechanical ventilation adjuvant therapy (intra-airway medication, prone positioning, etc.) ventilation, extracorporeal model lung oxygenation technology, etc.).

Acute lung injury (ALI) is the result of various direct and indirect injury factors damaging capillary endothelial and alveolar cells, which causes diffuse pulmonary interstitial and alveolar edoema as well as acute hypoxic respiratory insufficiency. The pathophysiological features are decreased lung volume, lung compliance, and imbalance of ventilation/blood flow. ALI is one of the common clinical critical illnesses, which seriously affects the quality of life of patients. According to the diagnostic criteria of ALI/ARDS proposed by the European and American Joint Conference in 1994, the incidence rates of ALI and ARDS in the United States in 2005 were 79/100,000 and 59/100,000 respectively. The incidence of ALI/ARDS in severe infections can be as high as 25% to 50%. ALI or ARDS accounts for a quarter of acute respiratory failure events in ICUs.

Sleep apnea is a sleep disorder caused by symptoms of pauses in breathing or reduced breathing during sleep. The duration of each pause can vary from seconds to minutes and occurs several times throughout the night. To be diagnosed as sleep apnea, symptoms must occur more than five times in an hour to be established. There are currently three types of sleep apnea: obstructive sleep apnea, central neuropathic central sleep apnea, and mixed sleep apnea with both symptoms, including obstructive sleep apnea. Apnea is the most prevalent symptom. In obstructive sleep apnea symptoms, breathing is stopped due to airflow obstruction; while in sleep apnea of central neuropathy, breathing stops due to lack of breathing strength. The disease is more common in middle-aged men. The incidence of men is about 2 to 8 times that of women. On average, one in 20 adults suffers from it, and the incidence of the disease in the elderly is 10%.

Both of these common lung diseases can cause respiratory failure. Respiratory failure is a serious disorder of pulmonary ventilation and/or ventilation function caused by various reasons, and a clinical syndrome that causes a series of physiological functions and metabolic disorders. It results in ineffective gas exchange, resulting in hypoxia with/without carbon dioxide retention. Therefore, it is very necessary to use a ventilator to keep the patient's airway open and effective ventilation. In recent years, non-invasive positive pressure ventilation has expanded from the traditional treatment of obstructive sleep apnea-hypopnea syndrome to the treatment of a variety of acute patients, postoperative prevention and family rehabilitation have good therapeutic effects.

This study mainly discusses three abnormal breathing situations, including breathing under anesthesia, sudden changes in breathing, and breathing in neonates. In addition, these special conditions will be contrasted with normal breathing conditions.

Anesthesia Machine: After a patient is anesthetized during major surgery, the muscles around the tongue and throat relax and can block the airway. Therefore, to ensure a continuous supply of oxygen to the patient's lungs

during anesthesia, more oxygen is given to the lungs through the ventilator before the anesthesia begins. Manual ventilation requires the operator to continuously squeeze the storage bag to make the patient breathe. During a long operation, the operator is not only very tired, but also affects other work. Therefore, an automatic ventilator is often used to mechanically allow the patient to breathe. During anesthesia, the anesthesia machine provides a continuous cycle of oxygen and anesthetic gas. With the strengthening of the anesthesia effect, the oxygen provided by the ventilator will gradually increase, and finally replace the patient's spontaneous breathing function.

Abnormal breathing: The normal breathing rate is 16 to 20 cycles per minute, and the ratio to the number of heart beats is 1:4. Abnormal breathing, on the other hand, is a sudden change in the frequency, depth, or rhythm of breathing. Irregular breathing patterns are characteristic of increased intracranial pressure. Common clinical abnormalities include tidal breathing, shallow and fast breathing, and sobbing-like breathing. Irregular breathing and tidal breathing are more common in brainstem injury. Slow respiration is more common when there is a posterior fossa hematoma. Irregular breathing and tidal breathing are more common in brainstem injuries. Such as sudden respiratory arrest during steady breathing, or when the patient suddenly joins in irregular spontaneous breathing when the ventilator completely replaces spontaneous breathing. This is an early symptom of respiratory insufficiency due to respiratory disease or disease in the organs or tissues that control and affect breathing. If the condition is further aggravated, then there is respiratory distress or difficulty breathing, even respiratory failure, which is life-threatening.

Newborn breathing: A newborn's breathing rate is generally 40 to 60 breaths per minute, which is much different from an adult's breathing rate and depth. If it exceeds 60 breaths per minute, it is considered shortness of breath. Premature infants are prone to periodic breathing. For example, breathing is interrupted within 20 seconds, and the heart rate does not slow down, which is still 120 to 140 beats per minute. Once the neonatal respiratory rate fluctuates abnormally, it needs to be dealt with in time. Neonatal lungs may be

immature, resulting in respiratory distress, so it is particularly important to assist or temporarily replace neonatal breathing with a ventilator.

2.3.2 Control strategy

Mechanical ventilation in patients with acute lung injury (ALI) or acute respiratory distress syndrome (ARDS) can buy time for the lungs to recover, but ventilation is invasive and can damage the lungs. Whether the ventilator controls air pressure or restricts volume during each breath, it is uncertain whether ventilator-related injury can be reduced.

a) Volume control ventilation

Volume control ventilation (VCV) is that the ventilator performs ventilation with a preset ventilation volume. When the ventilator reaches the preset tidal volume, the ventilation is stopped and passively exhaled relying on the elastic recoil of the chest and lungs. In volume-controlled ventilation, minute ventilation, tidal volume, respiratory rate, and inspiratory time are all set. To ensure that each ventilation reaches the preset tidal volume, the ventilator needs the corresponding pressure to oppose the airway resistance, thoracic and lung tissue compliance. Since different diseases of different patients lead to different airway resistance, thoracic and lung tissue compliance, ventilators need to provide different pressure support to ensure appropriate minute ventilation and tidal volume. Therefore, during volume-controlled ventilation, minute ventilation is constant while airway pressure varies.

b) Pressure control ventilation

Pressure control ventilation (PCV) is a ventilator that ventilating with a preset airway pressure. When the ventilator quickly reaches the preset airway pressure and maintains the airway pressure for a period of time by decelerating the airflow, it is a kind of time-switched pressure control mode ventilation system. Airway pressure, ventilation flow rate, respiratory rate and inspiratory time are set in pressure-controlled ventilation mode. Tidal volume is affected

by airway pressure, inspiratory time, compliance of the respiratory system, and airway resistance. Under the premise of constant pressure and inspiratory time, the tidal volume and minute ventilation of mechanical ventilation are not constant due to the different compliance and airway resistance of the respiratory system of different patients. When the same patient is mechanically ventilated, changes in intrathoracic pressure due to spontaneous breathing will also lead to changes in tidal volume. Therefore, during PCV, the airway pressure of different patients is constant, while the tidal volume and minute ventilation are variable.

2.3.3 Ventilator-induced lung injury

Although many types of ventilators have demonstrated a strong ability to maintain breathing, current ventilators are mainly controlled by a single variable in an open loop. Both the volume control strategy and the pressure control strategy face a single information problem. When most patients have new breathing conditions and need to be corrected, they can only be adjusted manually by the doctor. Such procedure is high-risk, time-critical, and requires a lot of the doctor's experience. Because doctors cannot see the 2D/3D images of the lungs in a short period of time, they can only estimate the changes of the organs through experience based on the only vital signs and parameters.

Ventilator-Induced Lung Injury (VILI) is defined as damage to normal lung tissue or further exacerbation of damage to diseased lung tissue by mechanical ventilation, which is the result of a combination of direct mechanical lung injury, secondary biological injury and oxygen toxicity due to increased cross-pulmonary pressure and shear forces caused by mechanical ventilation.

The definition and classification of ARDS, ventilation parameters (tidal volume, respiratory rate, positive end-expiratory pressure, peak, plateau, driving and cross-pulmonary pressure, energy, mechanical power and intensity) as determinants of VILI, and the significance of prone position and muscle paralysis were all discussed by Cruz et al. in 2018 [27]. Nieman et al. analysed

the pathophysiology of ARDS leading to lung vulnerability to VILI in 2020 [28]. A perspective on ventilator-induced lung injury was presented by Santos et al. [29], with a focus on the mechanisms and clinical implications. Whether injurious ventilation per se can trigger cytokine-mediated lung inflammation in the absence of prior lung injury remains controversial. To address this question, an in vivo mouse model of acute lung injury produced by high tidal volume (VT) ventilation was developed by Wilson [30]. The anatomical and physiological framework in which ventilator-induced lung injury may occur was described by Gattinoni et al. in 2010 [31]. Differences in cross-pulmonary pressures, which are the outcome of an unbalance between pulmonary pressure and strain, are what predominantly cause to lung injury in both scenarios. Changes in lung structure and function due to this imbalance were focused on by Kuchnicka in 2013 [32]. According to recent studies, these patients may develop lung injury similar to that observed in mechanically ventilated patients with VILI. Therefore, in order to prevent the progression of a patient's self-induced lung injury, Brochard et al. [33] proposed in 2016 that the use of LPV (nowadays preferably used in conjunction with sedation and tracheal intubation) may be considered a prophylactic treatment rather than just a supportive treatment.

To offer evidence-based and experience-based therapeutic recommendations for the treatment of those patients with ARDS, Chiumello et al. [34] assessed the existing clinical evidence pertaining to ventilatory support and adjunctive therapy in 2017. The current evidence and indications for extracorporeal gas exchange were summarised by Moerer et al. [35]. According to the work of González-Pacheco et al. [36], once there are significant and severe histological lesions, then inflammation infiltrates the alveolar wall and alveolar lumen and there may be large areas of parenchymal solidity and alveolar hemorrhage. Hamlington et al. [37], demonstrated that atelectasis caused perforation, which was further enlarged by volumetric trauma. Grieco et. al. [38] discussed the role of pressure in assessing the impact of mechanical ventilation in patients with ARDS. According to the studies of Marini et al. [39], the duration of exposure, the number of intolerable high-energy cycles delivered per unit time (mechanical power), and the potential injury of the

inflation mode depends on tissue vulnerability were highlighted. Since alveolar dynamics in the intact lung remains largely a 'black box', the contribution of Grune to the mechanisms of VALI and VILI, as well as the effectiveness of optimised ventilation strategies is restricted to indirect parameters and endpoints of lung injury and mortality [40]. Emerging concepts in alveolar dynamics, including such alveolar expansion/contraction, stability/instability, and opening/collapse, were discussed in the review study by Grune [40].

In more severe forms of ARDS, where lung capacities are lower and more heterogeneous, there is an increased risk of VILI [41]. The lungs are more prone to strain and may cause volutrauma when inputting the optimal tidal volume. Additionally, due to different levels of inflation in different lung zones during inspiration, lung inhomogeneity leads to an increase in alveolar pressure between adjacent lung regions [42]. Lung ventilation patterns can shift dramatically as a result of airway recruitment or collapse [42]. Therefore, even when LPV is used, VILI still can occur significantly [43]. Current methods of mechanical ventilation can be easily obtained from the bedside and rely on measurements of indicators such as pressure, flow, oxygenation index, etc. However, it is challenging for existing mechanical ventilation techniques to account for lung structures and areas of lung injury. This can consequently result in certain lung lobes expanding excessively and causing damage [44]. An image-guided procedure is urgently needed for better mechanical ventilation control.

2.3.4 EIT-assisted ventilator

EIT has potentially significant advantages over conventional imaging modalities because the system is portable and non-radiological and can be applied to patients for extended periods of time. Therefore, EIT reconstructed time series can be utilised as a new diagnostic and counselling tool to effectively optimise mechanical ventilation in critically ill patients.

Despite the limitations of the EIT, studies have shown that the concentration of air in the lung leads to highly contrasting levels of conductivity in different

tissues [45]. Assessing the impact of the proportion of open lung area measured by EIT on the global inhomogeneity (GI) index was the focus of Zhao's work [46]. The contribution made by Bodenstein [47] was to demonstrate the applicability of the method in a model of mechanical ventilation of both healthy and sick pig lungs. EIT was used to monitor regional ventilation in the lungs [48], determine the mechanical ventilation settings, evaluate the distribution of the tidal volume and end-expiratory lung volume (EELV), and adjust the PEEP/VT combination [49]. Additionally, EIT can evaluate the efficacy of pressure control [50], quantify recruitment and overexpansion, provide a more realistic assessment of various ventilator modes or recruitment manoeuvres, and help identify responders and non-responders to such manoeuvres. A protocol for personalising PEEP and VT has been developed using EIT-derived information on pulmonary resuscitability, hyperexpansion and alveolar circulation. Furthermore, EIT can also direct fluid management in the intensive care setting and assist in the management of life-threatening lung diseases such as pneumothorax [51].

The advantage of these techniques is that EIT has high temporal resolution and can be utilised safely at the bedside for a long time [52]. A preliminary study was conducted in the Neuromuscular Clinic at Children's Hospital Colorado in six children with SMA-I to investigate the feasibility of using three-dimensional (3D) EIT images to estimate lung volumes before and after mechanical ventilation-exhaustion (MIE) to assess the effectiveness of MIEz [53]. In anaesthetized patients or while using mechanical ventilation in the ICU, this method can infer atelectasis and lung hyperinflation [54]. However, according to Henry et al., it is currently unclear how pixel compliance can be used to directly model the lung response to pressure control [42].

In patients with acute respiratory failure, EIT aids in evaluating the effectiveness and safety of mechanical ventilation [55]. The monitoring and assessment capabilities based on EIT images are the foundation of the existing applications, however, a closed control loop where the ventilator is controlled by image signals is not actually realized to date. EIT will therefore

be a monitoring and control tool for individualised ventilation therapy once these problems are resolved, which can enhance patient safety during mechanical ventilation.

2.4 Application of EIT in medical imaging

EIT offers a variety of benefits. This approach is suitable for bedside measurement and ICU monitoring since it is non-invasive, radiation-free, inexpensive, safe, and simple to use. Due to these benefits, there is currently a great deal of research and development being focused on this potential technology [56]. These various medical applications are summarised in this section.

2.4.1 Brain imaging

Due to its ability visualise variations in blood flow and volume that are known to occur during evoked brain activity, similar towards how functional MRI (fMRI) operates, EIT has the potential to imaging brain activity [57-60]. EIT images can be obtained and recorded continuously for days during the pre-surgical evaluation of patients with refractory epilepsy, allowing one to image the afflicted area and obviate necessity intracranial electrodes and the associated morbidity. When patients awaiting surgery to eliminate the epileptic trigger zone, EIT could provide a routine bedside method for continuous imaging generation that can detect the initiation of seizures [61].

2.4.2 Breast imaging

Several research teams have investigated breast imaging adopting EIT. Zain and Chelliah, [62], applied EIT technique on 150 mammography patients. Breast imaging - electrical impedance (BI-EIM) classification was used to visually interpret the images in order to identify a certain abnormality. A visual interpretation of the images was correlated with applying Chi-square to perform a quantitative assessment by comparing the breast average electric

conductivity with the norm. The quantitative evaluation of electrical impedance tomography was observed to be associated with the visual interpretation of breast imaging by the authors.

2.4.3 Lung imaging

Numerous research using the EIT approach for lung imaging have been completed and published [63, 64]. Meier et al. [65] investigated the efficacy of EIT in demonstrating acute lung injury in animal models. The contribution of Zhang et al. [66] is to examine the feasibility of EIT to assess the extent of obstructive ventilation defects at global and regional levels. Ventilation heterogeneity may be better described by time-based measures, and the EIT is high temporal resolution makes this assessment possible. Pulmonary edema is also researched by EIT.

2.4.4 Heart imaging

Throughout the cardiac cycle, the electrical conductivity of heart varies according to the volume of blood it contains. As a result, EIT can be used to evaluate the stroke volume (SV) [67-71]. To reconstruct a cross-section of the body, a single plane of electrodes is often applied. Electrodes attached to the surface of the body to obtain the electrical measurements. Systolic ejection volume can be monitored by portable EIT devices as PulmoTrace [72] and CardioInspect [73], Figure 2-2.

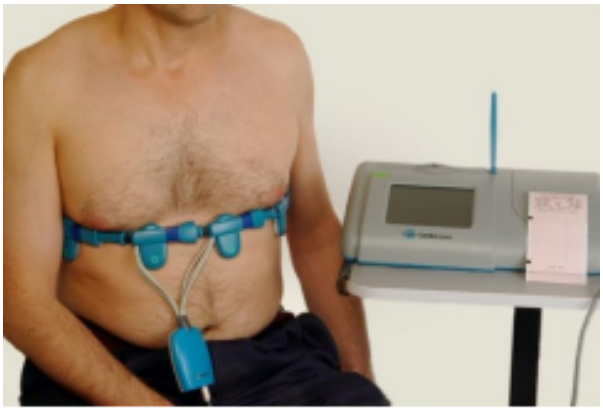

Figure 2-2: Cardiac monitoring by CardioInspect system [72].

2.4.5 Cancer detection

As early as 1926, Fricke and Morse [74] reported that tumor tissue exhibited different electrical properties from healthy tissue. Additional research resulted in the conclusion that these variations might serve as the foundation for an accurate diagnosis. In order to diagnose tumours via the measurement of bioimpedance, knowledge of the electrical conductivity of tissues is also required. The impedance of malignant cells differs from that of healthy cells. For example, Haemmerich [75] showed that at 1 MHz, healthy tissue had an electrical conductivity of $(4.61 \pm 0.42)x10^{-1}$ S/m while hepatic tumors had an electrical conductivity of (2.69 ± 0.91) S/m. This fact shows that the two types of tissue can be differentiated by their electrical conductivity. Measuring at different frequencies also makes it possible to distinguish between normal and cancerous tissues, for example in the breast, the skin or the prostate [76, 77]. As the electrical properties of cancerous and normal lesions depends on the frequency, the conductivity images obtained by the EIT would allow them to be objectively discriminated, thus ensuring an early diagnosis of cancer.

2.4.6 Hyperthermia treatment

Thermal monitoring of hyperthermia treatment also can be carried out by EIT. Poni et al. [78] presented a simulation study to investigate the feasibility of EIT as a low-cost, non-invasive technique for the monitoring and adaptation of hyperthermia treatments. EIT can reconstruct these changes in 3D in order to map temperature and perfusion non-invasively. A rise in tissue temperature causes changes in tissue conductivity and perfusion.

2.4.7 New-born cranial imaging

EIT has been applied for cranial imaging in the new-born [57]. A weighted back projection algorithm was suggested by the study as a sensitive way to obtain images of the resistivity distribution within a body segment in order to monitor the spatial distribution of electrical conductivity for cranial imaging in the new-born.

The abovementioned work highlights the potential of EIT for medical imaging and treatment. However, a great deal of challenges still remain unsolved before EIT can be recognised as a practical technique for medical imaging. These challenges include: a) High spatial resolution image reconstruction for conductivity variations of irregular objects; b) Combination of 2D/3D EIT imaging equipment with other medical equipment, c) Long-term real-time monitoring of organs or tissues, cross-validation and interpretation of results.

2.5 Summary

This chapter briefly reviewed the EIT technique from the perspectives of fundamental theory, EIT system, EIT image reconstruction algorithms and the recent advances of EIT in medical imaging. In addition, this chapter also reviewed the mechanical ventilation from two aspects of the lung diseases and control strategy. The purpose of the chapter is to help understand the ventilator based on EIT techniques, current clinical demands, its future development trends, and the emerging or potential applications with maximum utilization of the many merits of EIT. The innovative work and scientific contribution of the thesis from these perspectives will be demonstrated subsequently in the following chapters.

Chapter 3 Improved 3D lung imaging algorithm for EIT

3.1 Introduction

Electrical impedance tomography has been widely used in medical imaging for lung diseases. It has been the subject of quite intensive research for about 20 years but has yet to become established as a routine tool in healthcare [79] due to low spatial imaging resolution. One of the most prevalent diseases in the world today, particularly in undeveloped countries, is lung disease. Lung illness is very often fatal. It is crucial to have an effective method for lung disease diagnosis, treatment, evaluation of efficacy, and prognosis prediction. In Shi's review work [80], the research progress of the clinical applications of EIT in the treatment of lung pathology was discussed, including image reconstruction algorithms and hardware system design. Recent research on the use of lung EIT was summarised by Gong et al. [81], with a focus on reducing artefacts and better localising conductivity changes within the image domain. In order to help achieve this goal, Zifan et al. [82] introduced a pipeline for creating anatomically precise meshes for EIT forward and inverse models. A new form reconstruction framework built on the Boolean concept of electrical impedance tomography was suggested by Liu et al. [83]. The proposed method by Wu achieves high resolution and robust shape reconstruction with multiphase conductivity for EIT lung imaging, especially in the presence of measurement noise and interference [84]. The significance of EIT image reconstruction techniques was discussed in the work of Adam et al. [85].

Wagenaar [86] aimed to describe the modelling and performance of a 3D EIT with two electrode planes . To overcome the sensitivity to cardiac displacement and chest morphology, a 3D EIT configuration with 2 x 16 electrode planes and an object-specific reconstruction model was used [67]. Li [87] proposed a method to calculate GI based on 3D EIT reconstructed images to assess lung

injury. A 3D human chest modelling method for EIT image reconstruction to enhance the precision and optimize the existing finite element modelling methods was proposed by Huang [88]. Kao [89] described a 3D analytical reconstruction algorithm embedded in a prototype EIT system capable of reconstructing real-time images at roughly 20 frames per second to monitor impedance changes in the chest in real time. However, most existing algorithms are based on two or more layers of electrode planes, which would slow down the imaging speed. More importantly, the quality of the reconstructed images also can be improved. The studies in this section not only incorporate a more realistic lung model to facilitate accurate volume estimation, but the reconstructed images can also be used for real-time imaging to control the mechanical ventilation.

As mentioned in the chapter 2 many lung diseases rely on ventilator support, and the usage of ventilators might result in lung injury. However, the location and extent of lung damage can only be determined when the CT or MRI taken. Frequently, people do not aware they have the condition until it is already in advanced stages. Treatment for advanced stages is generally much more complicated than for early stages, and the likelihood of recovery is lower [90]. However, a comprehensive analysis of the patient's state is not possible with 2D EIT images, because the different heights of the lung planes provide difference information, such as over-expansion or collapse. Although 3D EIT imaging can provide more accurate information, there are still many technical challenges to be overcome, such as image reconstruction of complex models, or high-precision real-time imaging. It is necessary to construct an appropriate 3D lung model in order to resolve the EIT forward problem. The majority of research on 3D EIT lung image reconstruction has used simple and regular geometric models to simulate. Yet, it is evident that the actual contours of the human lung and chest are much more complex and challenging to simulate using simple geometric models. Details that are missed can cause unanticipated mistakes and reduce the reliability of the modelling results. In addition, another significant difficulty for medical applications of EIT with 3D

imaging is how to speed up imaging process while retaining spatial resolution because the time cost of 3D imaging is higher than that of 2D imaging.

In this Chapter, as a more developed model of stimulation based on a realistic lung model, the feasibility study of EIT for image reconstruction of lung tissue is presented. The ultimate aim of this thesis is to achieve EIT control of mechanical ventilation by way of estimating the volume of the lungs. However, the total volume will be estimated by means of the area of a multi-layered lung section. Therefore, accurate reconstructed images and clear boundaries are important for the estimation of volume. To improve the reliability of the study, this study brings the model closer to the real lung by fusing information from CT images. Furthermore, not only high-resolution images are required, but also imaging speed to match mechanical ventilation in real time. An innovative 3D excitation approach is put forth in this chapter to estimate the volume of the lung. And different algorithms are proposed to find the ideal reconstructed image in the process of reconstructing 3D images using only one layer of electrodes. The single layer electrode imaging approach allows for shorter 3D imaging times, which will help to enable real-time lung monitoring. The analysis of the results focuses on the image quality and the accuracy of the predicted tissue conductivity in the reconstructed images. The ideal imaging parameters like the optimal number of iterations are summarised. Real-time 2D and 3D imaging capabilities are made possible by these innovative features, which are crucial for the application of EIT in medical imaging.

3.2 Method

3.2.1 3D lung model

In order to connect simulation with clinical applications, experimental models are essential in EIT. Realistic human lung and chest shapes are very complex to be represented using simple geometric models. A highly advanced type of medical imaging is CT technology, which creates high-resolution tomographic

images. To create the most accurate model of the true thoracic and lung contours, CT images are utilised for lung contour extraction. As a result, realistic modelling makes the subsequent study become more reliable, not only reducing errors but also increasing the perceived worth of visuals.

Frist, the lung images of CT are binarized to enhance important contour details and make the boundary more visible. Then, two sets of images are created by processing the thorax and lung contours individually. Threshold segmentation is carried out in Minics by choosing values that have the least potential impact on the lung region. The lung contours and thorax contours are output for fusion along with the lung and thorax shapes. A 3D model is created in Mimics using the 2D contour slice cloud with the proper interpolation, and a point cloud file is generated [91]. After that, the 3D model is imported into Solidworks to be smoothed [92]. The finished lung and thorax 3D models are independently imported into COMSOL Multiphysics as the last stage, as demonstrated in Figure 3-1. A 3D chest model with the lungs inside is shown in Figure 3-2.

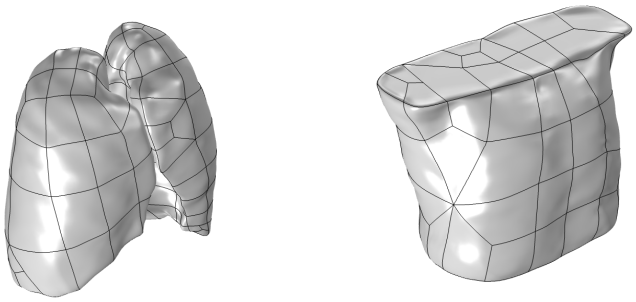

Figure 3-1: Lung (left) and thorax (right) model in 3D.

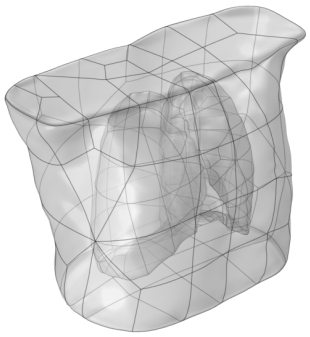

Figure 3-2: 3D model in COMSOL Multiphysics.

Electrodes around the chest, lungs, and thorax are part of the models needed for the studies. Electrical characteristics are just one example of the physical differences between various materials. Similarly, the electrical impedance of various tissues [75] will display different characteristics in the human body. The EIT may identify slight variations in impedance, as mentioned in chapter 2. To ensure a close approximation to reality, each component of the model should be set the right material. Since there is homogeneity in the impedance of the lung or intra-thoracic tissue, it is assumed that the impedance of the chest and lungs is distributed uniformly. The lung has a conductivity of 0.480 S/m, compared to 0.120 S/m for the remainder of the chest [93].

The electrodes are a crucial part of the model in addition to the thorax and lungs. Technology for portable and wearable devices has grown in popularity over the past few years. They are developing more quickly as a result of a lot of study being done in this field. In contrast to the two- and three-layer electrodes typically used in most research, a one-layer electrode measurement was implemented to speed up imaging process of EIT. The majority of tests used the adjacent excitation approach, in which the excitation current was injected into adjacent electrodes [94], as illustrated in the Figure 3-3. 16 electrodes were distributed evenly across the chest cavity.

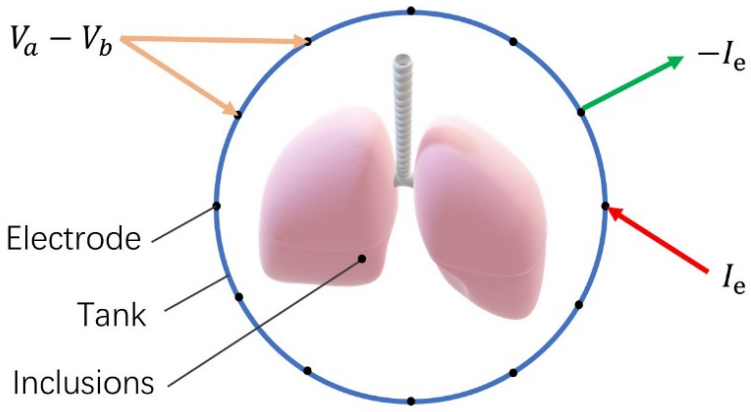

Figure 3-3: Adjacent excitation mode.

3.2.2 Sensitivity matrix

The forward question's aim is to analyze the electric field's potential distribution, which can be depicted by a sensitivity map. Since the sensitivity map will be used to reconstruct the image, the quality of the map will have an impact on the outcome. The electric intensity components in each direction are multiplied and added independently to create the sensitivity map. A sensitivity map can be computed based on the sensitivity map theorem of Geselowitz and Lehr [95].

$$\boldsymbol{J}_{ij} = -\left(\int \frac{\nabla \boldsymbol{\varphi}_i}{\boldsymbol{I}_i} \cdot \frac{\nabla \boldsymbol{\varphi}_j}{\boldsymbol{I}_j} d_x d_y + \int \frac{\nabla \boldsymbol{\varphi}_i}{\boldsymbol{I}_i} \cdot \frac{\nabla \boldsymbol{\varphi}_j}{\boldsymbol{I}_j} d_x d_z + \int \frac{\nabla \boldsymbol{\varphi}_i}{\boldsymbol{I}_i} \cdot \frac{\nabla \boldsymbol{\varphi}_j}{\boldsymbol{I}_j} d_z d_y\right) \quad (3.1)$$

where $\boldsymbol{J}_{ij}$ stands for the sensitivity matrix from j^{th} electrode to i^{th} electrode. $\boldsymbol{\varphi}_i$ and $\boldsymbol{\varphi}_j$ describes the potential distribution when the injection current are $\boldsymbol{I}_i$ and $\boldsymbol{I}_j$ respectively. x, y and z respectively represent the direction in the 3D coordinate system.

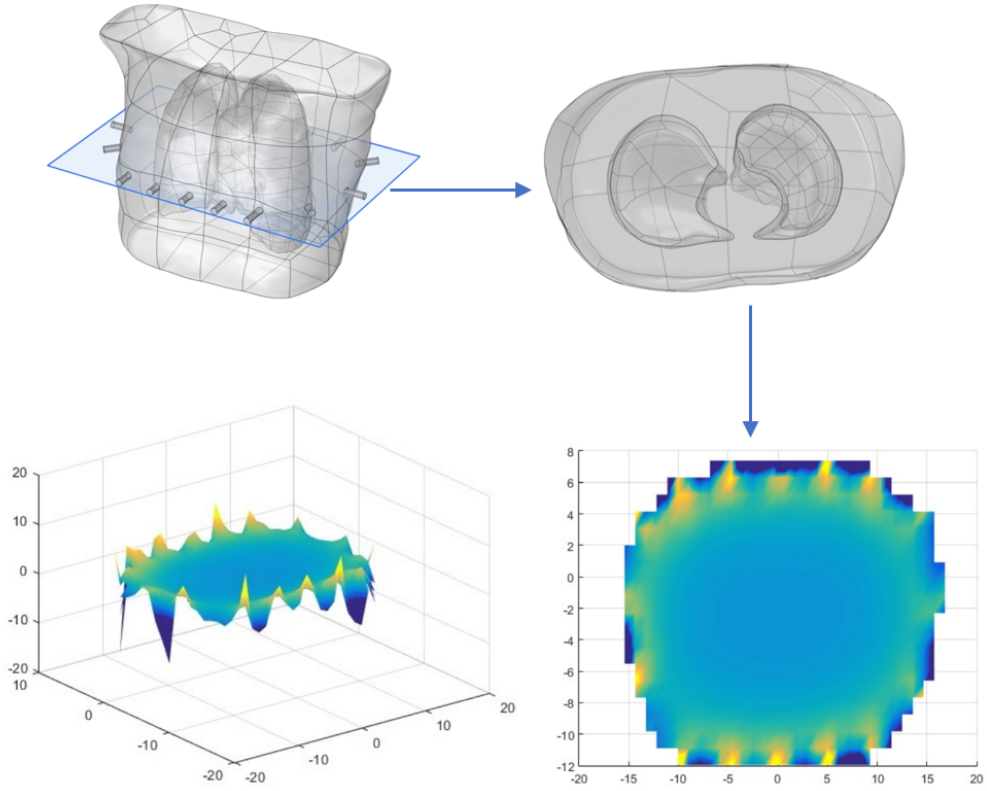

Figure 3-4: Sensitivity map.

3.2.3 Reconstruction algorithm

A sensitivity matrix and voltages across two adjacent electrodes, both measured and reference voltages, are necessary for the image reconstruction. The difference between the measured voltage and the reference voltage is applied to accomplish imaging. Dynamic imaging has been used in this research because it is impossible to acquire information about the null field in an actual experiment without lungs. Therefore, the voltage of the end-expiratory condition is the reference voltage. Additionally, the excitation current used was ± 0.01 A, a safe current amplitude with no side effects on people.

LBP and Tikhonov are two representative non-iterative algorithms [96]. The Tikhonov regularization algorithm [97] is the most often used method for image reconstruction in EIT. Its major goal is to ensure that both residuals and penalty functions are minimised. The solution to the linear inverse problem is given by Equation 3.2, where is the norm of the conductivity distribution controlled, and the stronger noise components are minimized [98].

$$\Delta\hat{\boldsymbol{\sigma}} = (\boldsymbol{J}^T\boldsymbol{J} + \lambda\boldsymbol{I})^{-1}\boldsymbol{J}^T\Delta\boldsymbol{V} \tag{3.2}$$

where $\boldsymbol{J}$ is the sensitivity matrix, and I stands for the identity matrix, which has the same dimension with $\boldsymbol{J}^T\boldsymbol{J}$.

The conjugate gradient (CG) algorithm [99] is one of the effective methods for solving non-linear optimisation problems. The benefits of conjugate gradient algorithm include quick convergence and a comparatively low level of complexity. Each search direction of the CG algorithm is conjugate. The most crucial component in the CG algorithm is changing the direction of iterations [100] in accordance with the conjugate relationship. It is necessary for the matrix of the problem to be symmetric and square. Since the sensitivity matrix $\boldsymbol{J}$ of the EIT inverse problem is neither symmetric nor square, Equation 3.3 [101] cannot be solved directly using standard CG algorithm.

$$\Delta\boldsymbol{\sigma} = -\bar{\boldsymbol{J}}^{-1} \cdot \boldsymbol{e} \tag{3.3}$$

where $\Delta\boldsymbol{\sigma}$ is the vector of relative conductivity change, $\bar{\boldsymbol{J}}^{-1}$ donates the elements of the normalized sensitivity matrix, and e stands for the vector of relative boundary change.

The minimization function, as shown in Equation 3.4, can be used to construct the minimization function presented in Equation 3.5 [101].

$$f(\Delta\boldsymbol{\sigma}) = \frac{1}{2}\|\bar{\boldsymbol{J}} \cdot \Delta\boldsymbol{\sigma} + \boldsymbol{e}\|^2 \tag{3.4}$$

$$\nabla f = r_0 = \bar{\boldsymbol{J}}^T \cdot (\bar{\boldsymbol{J}} \cdot \Delta\boldsymbol{\sigma} + \boldsymbol{e}) \tag{3.5}$$

The CG method may be applied to the transformed Equation 3.5 without forming $\bar{\boldsymbol{J}}^T\bar{\boldsymbol{J}}$ explicitly [101].

The results of two classics algorithms are presented in the Figure 3-5. Figure (a) shows the algorithm via LBP, while Figure (b) shows the Tikhonov algorithm. Both algorithms are non-iterative algorithms. It is clear that the Tikhonov algorithm gives better results than LBP, after all, LBP is not even able to image. Tikhonov works better, but it is difficult to distinguish that there are two lungs, left and right, much less to identify the shape and boundaries of the lungs. This may be because the distance between the two lungs is relatively small, making imaging more difficult. However, both algorithms are poor performance compared to the CG algorithm, due to the model is too complex. It is worth noting that the results in Figure 3-5 shows the image reconstruction in an ideal environment without any added noise. Once noise is added, the results definitely become worse.

The CG algorithm is much slower than LBP and Tikhonov in imaging because the results require several iterations to be derived. However, during assisted mechanical ventilation, the lungs did not change as fast. The conductivity of the lung in the end-inspiratory and end-expiratory states is 0.060 S/m and 0.120 S/m respectively. The amount of change is only 0.06 S/m during one respiratory cycle, which normally is 4 to 5 s. Therefore, a certain imaging speed can be traded off for a higher accuracy of image quality to facilitate a more

accurate estimation of volume change during breath. The CG algorithm overcomes the disadvantage of slow convergence by using first-order derivative information, which not only requires small storage capacity, and high stability. Therefore, in the subsequent chapters, CG imaging methods to optimise the reconstruction results will be presented, compared and discussed.

(a) LBP (b) Tikhonov

Figure 3-5: Different algorithms for reconstruction.

Table 3-1: Computation time for different algorithms.

Algorithm	LBP	Tikhonov	CG
Computation time (s)	0.027	0.045	0.088

3.2.4 Evaluation of image reconstruction performances

Correlation Coefficients (CC), Structural Similarity Index (SSIM) and Imaging Relative Errors (RE) between the real image and the reconstructed image were calculated in order to quantitatively analyse the EIT performance of various modalities and reconstruction algorithms [14, 17, 102, 103].

Correlation coefficient demonstrates the similarity between the true conductivity distribution and the reconstructed image, which is calculated with the following equation:

$$CC = \frac{\sum_{k=1}^{n}\left(\Delta\hat{\boldsymbol{\sigma}}_k - \Delta\bar{\hat{\boldsymbol{\sigma}}}\right)\left(\Delta\boldsymbol{\sigma}_k - \Delta\bar{\boldsymbol{\sigma}}\right)}{\sqrt{\sum_{k=1}^{n}\left(\Delta\hat{\boldsymbol{\sigma}}_k - \Delta\bar{\hat{\boldsymbol{\sigma}}}\right)^2 \sum_{k=1}^{n}\left(\Delta\boldsymbol{\sigma}_k - \Delta\bar{\boldsymbol{\sigma}}\right)^2}} \tag{3.6}$$

where $\Delta\hat{\boldsymbol{\sigma}}_k$ and $\Delta\boldsymbol{\sigma}_k$ represent the reconstructed variation and true conductivity variation at k^{th} pixel, in the meanwhile, $\Delta\bar{\hat{\boldsymbol{\sigma}}}$ and $\Delta\bar{\boldsymbol{\sigma}}$ donate the mean values of $\Delta\hat{\boldsymbol{\sigma}}$ and $\Delta\boldsymbol{\sigma}$, separately. A significantly larger CC indicates that the reconstructed image's shape is more identical to the original images.

Structural Similarity Index demonstrates the applicability as a general image similarity index [104]. Hore constructed a straightforward mathematical relationship for various image, such as additive Gaussian white noise [105]. SSIM is a number between 0 and 1, where a larger number indicates a smaller difference and better image quality between the output image and original image.

$$SSIM = \frac{(2\boldsymbol{\mu}_m\boldsymbol{\mu}_n + c_1)(2\boldsymbol{\sigma}_{mn} + c_2)}{(\boldsymbol{\mu}_m^2 + \boldsymbol{\mu}_n^2 + c_1)(\boldsymbol{\sigma}_m^2 + \boldsymbol{\sigma}_n^2 + c_2)} \tag{3.7}$$

where $\boldsymbol{\mu}_m$ and $\boldsymbol{\mu}_n$ stand for the mean of conductivity of reconstructed and true value, respectively. In addition, $\boldsymbol{\sigma}_m$ and $\boldsymbol{\sigma}_n$ represent the standard deviation of reconstructed results and true value. $\boldsymbol{\sigma}_{mn}$ is the covariance, and c_1, c_2 are constants.

The conductivity between the real object and the reconstructed image at each pixel is described by the image relative error. The tissue sample should have the smallest RE feasible to reflect the actual state of tissue. When RE is high, the gap between the model and the reconstructed image is generally high. RE is described by the following equation:

$$RE = \frac{\left\|\sum_l^n(\boldsymbol{\sigma}_l - \boldsymbol{\sigma}_l')\right\|_2}{\left\|\sum_l^n \boldsymbol{\sigma}_l'\right\|} \tag{3.8}$$

where $\boldsymbol{\sigma}_l$ and $\boldsymbol{\sigma}_l'$ are the calculated conductivity and the true value of conductivity in the l^{th} pixel within the valid field respectively.

3.3 Results

As mentioned in the Chapter 1 the goal of this study is to achieve multiple layers image reconstructions through excitation and measurement of a single layer electrodes. It is important to figure out the optimal parameters of the image reconstruction algorithm, but also to evaluate the distance range from the center layers. The z coordinate of the middle layer is -15 cm, which is the excitation and measurement layer, demonstrated in Figure 3-6(left). The positions of ±0.5 cm, ±1 cm, ±2 cm and ±4 cm from the central layer (Figure 3-6 right) were taken as the imaging targets, respectively. The coordinates of z other than the center layer are -19cm, -17 cm, -16 cm, -15.5 cm, -14.5 cm, -14 cm, -13 cm and -11 cm, respectively.

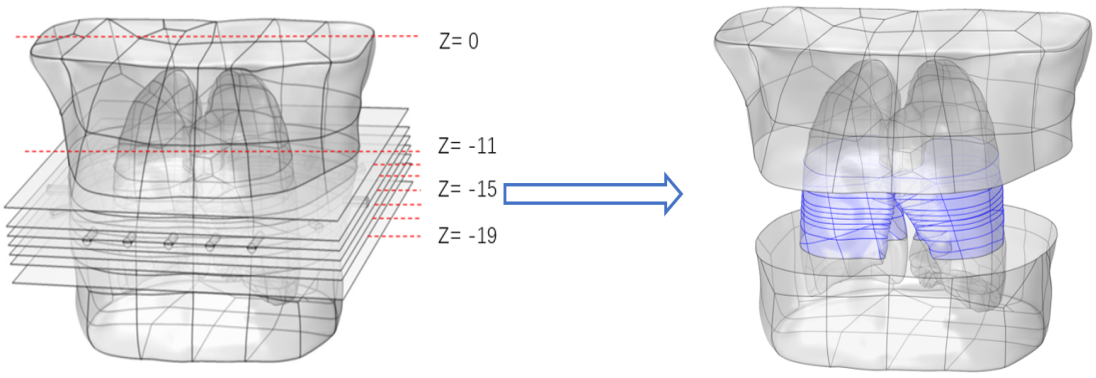

Figure 3-6: Slices of lung model.

Therefore, the final image reconstruction results are shown in Figure 3-7. The cross-section of each layer has characteristics that only belong to itself, and it is too one-sided to use 2D images to characterise information about a 3D organ. This is because the shape of the cross-section of the lung varies slightly from section to section, which also reflects the necessity of 3D imaging.

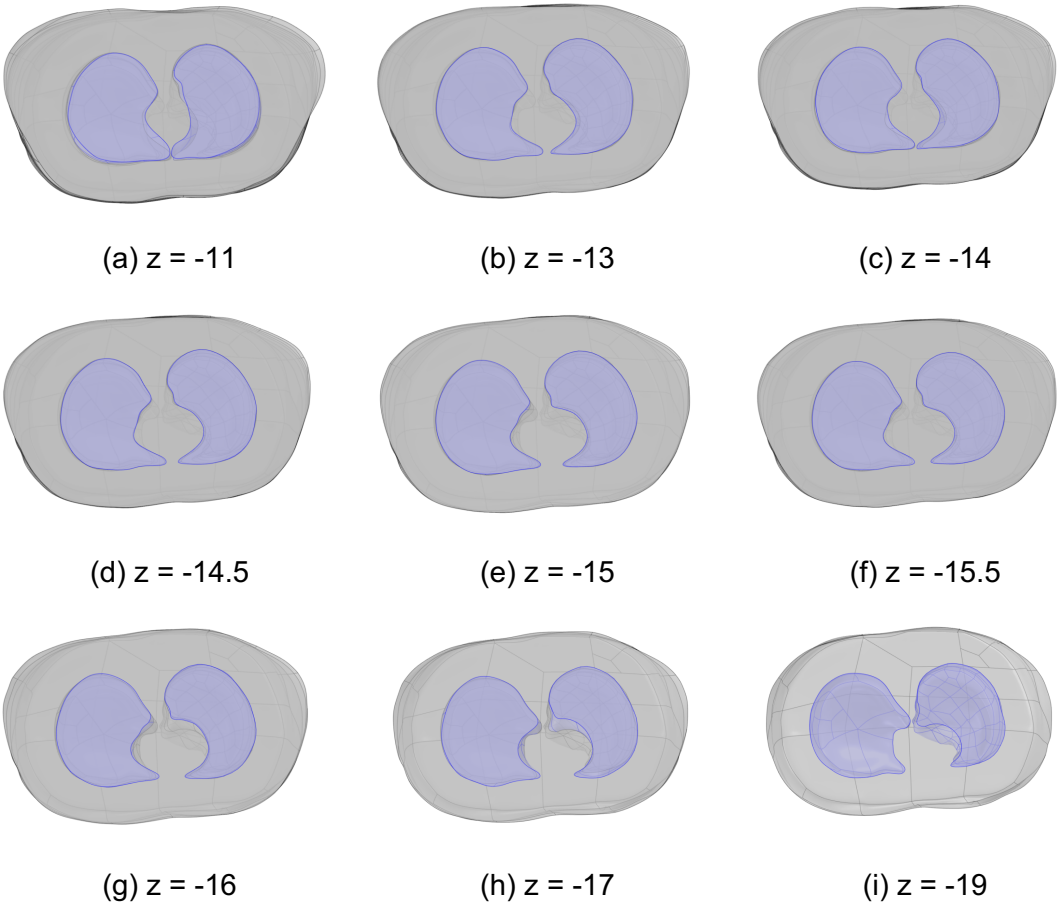

(a) z = -11 (b) z = -13 (c) z = -14

(d) z = -14.5 (e) z = -15 (f) z = -15.5

(g) z = -16 (h) z = -17 (i) z = -19

Figure 3-7: Layer slices of lung model from height -11 cm to -19 cm.

3.3.1 Sensitivity map for lung reconstruction

Sensitivity maps can give the fundamental information in the field of interest. When current is injected through the electrodes, changes in impedance at the field's edge are more clearly visible, and the quality of the reconstructed image that near to margins is higher. The lung and its contour, which is fairly symmetrically distributed near the electrodes rather than in the centre, are the interest of region focused on in this study.

Figure 3-8 to 3-10 display the combined sensitivity maps from the slice layers with a height of -11 cm to the slice layer with a height of -19 cm in 3D and 2D, according to the same lung model. Nevertheless, the extreme points are located at the edge of sensitive maps, as shown in the figures, because the

sensitivity map is heterogeneous, which has an impact on the imaging effect. In order to achieve a more uniform distribution of the sensitive field, the pixels at the edge of the electrodes are removed, as shown in Figure 3-11, which enhances the robustness of the imaging and is less susceptible to interference by noise.

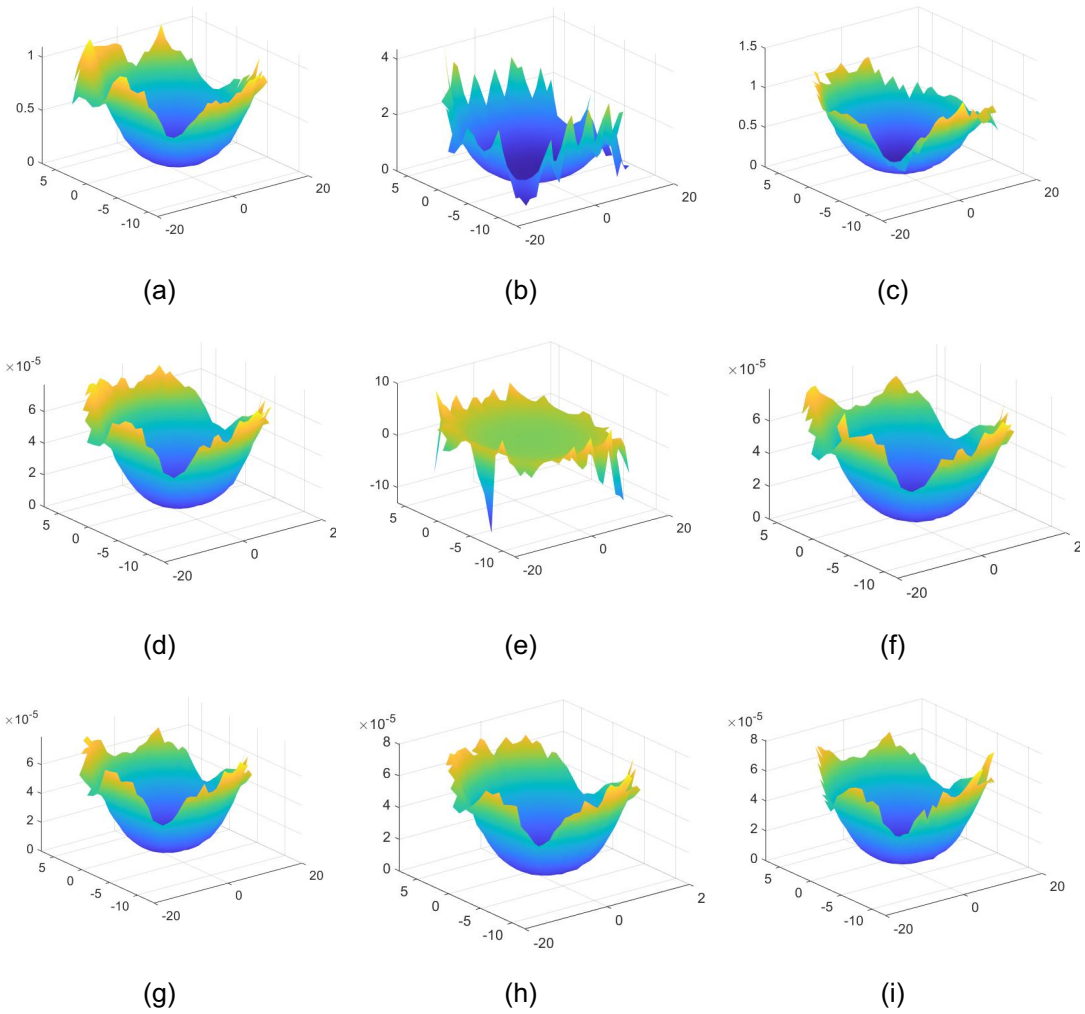

Figure 3-8: 3D combined sensitivity map of slices from height -11 cm to -19 cm according to the same lung model (from a to i).

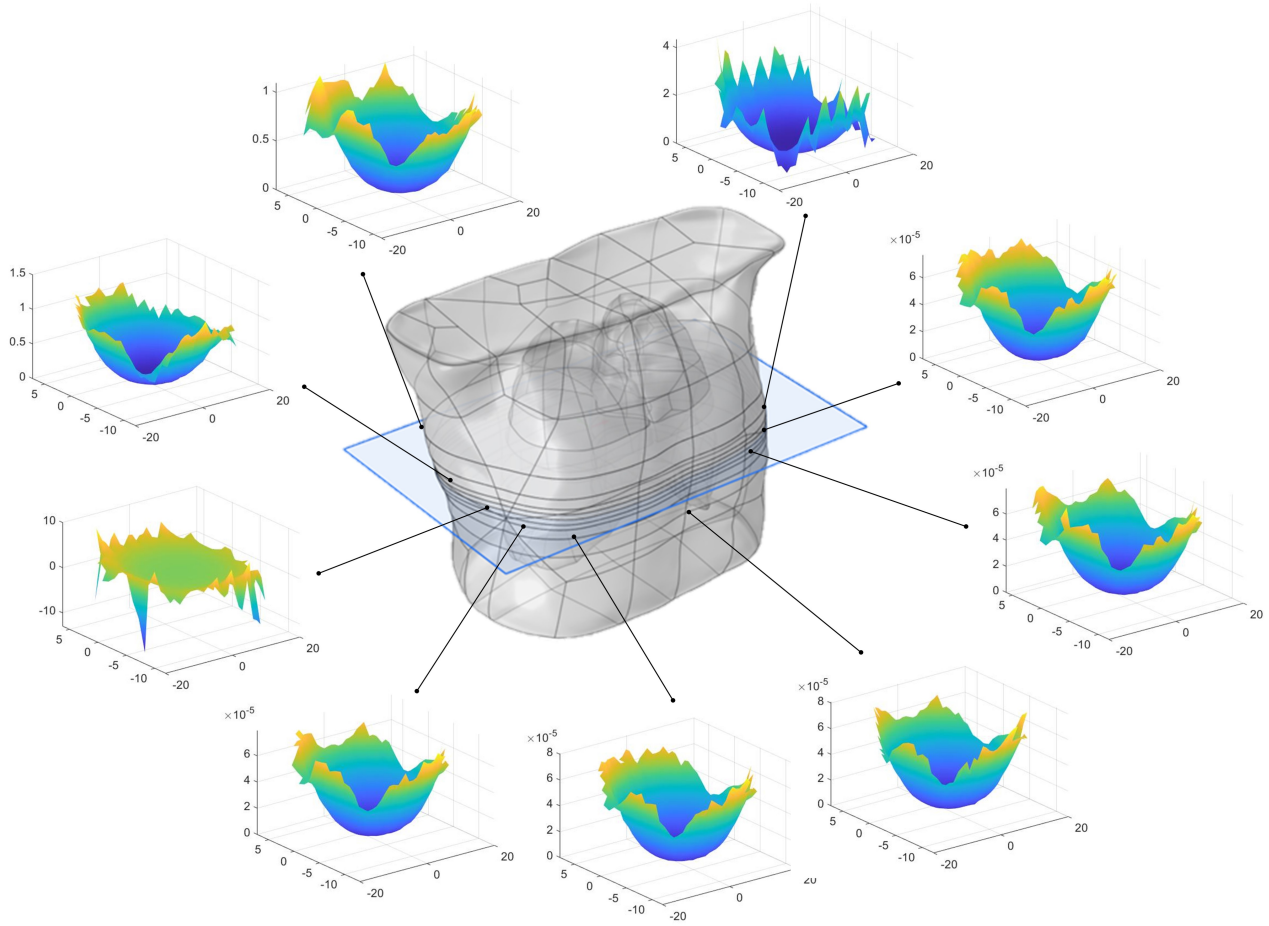

Figure 3-9: Combined sensitivity map with 3D lung model.

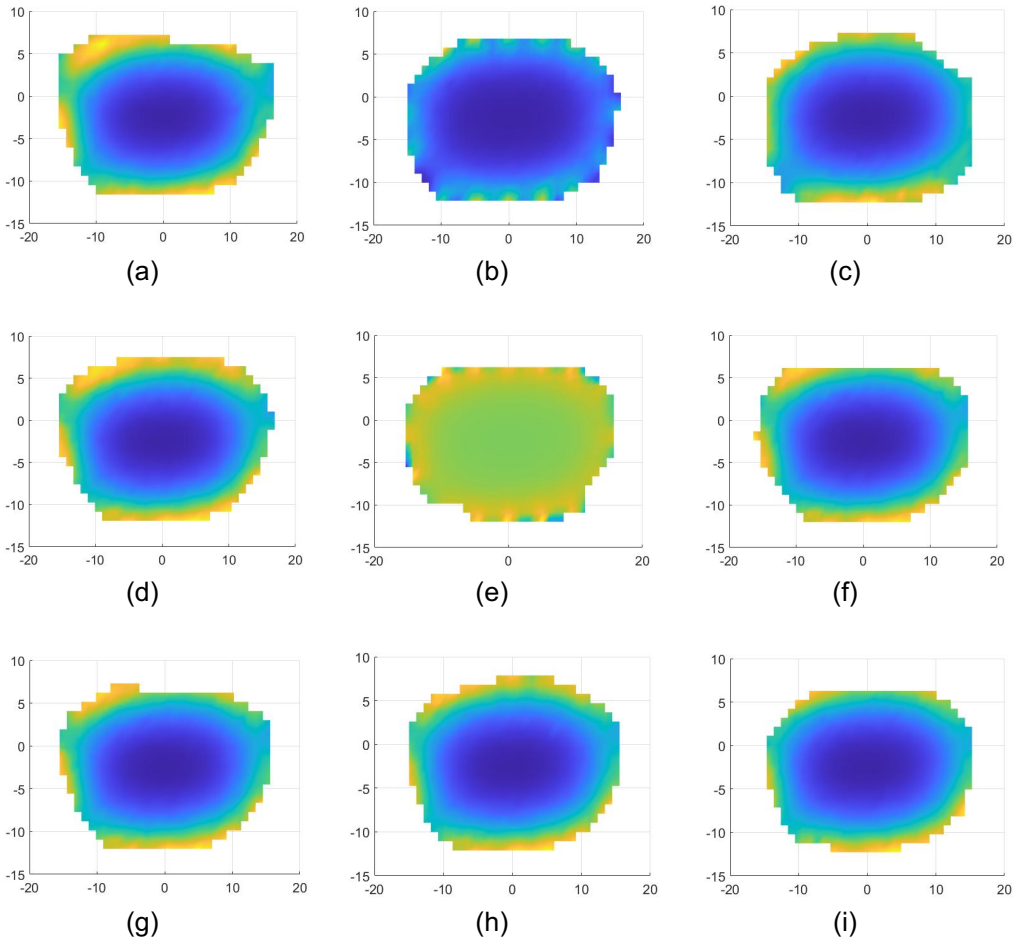

Figure 3-10: 2D combined sensitivity map of slices from height -11 cm to -19 cm according to the same lung model (from a to i).

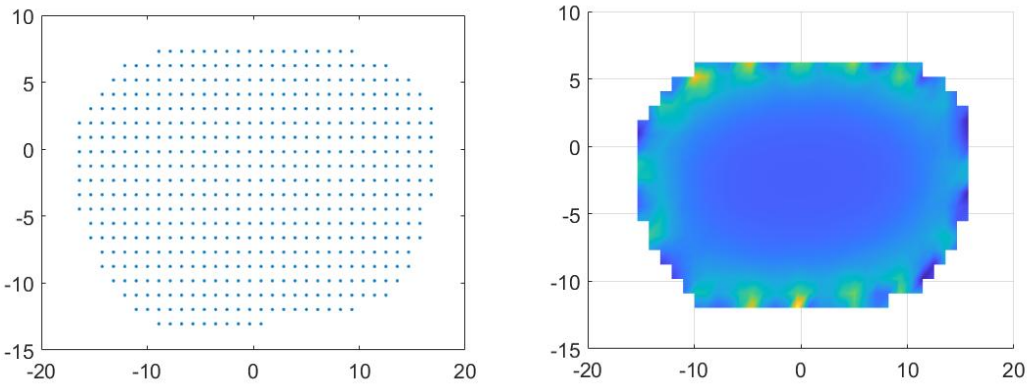

Figure 3-11: Refined sensitivity map of center layer (top view).

3.3.2 Reconstructed images

An important parameter in the CG algorithm is the number of iterations. Depending on the number of iterations, the reconstructed image results change, as shown in Figure 3-12. Figure 3-12 to 3-16 show the results from the multiple imaging layers with different numbers of iterations (from a plane of height -11 cm to -15 cm). Clearly, the optimal number of iterations in the imaging process varies for layers of different heights.

Too many iterations may not be necessarily ideal, as the improvement in image quality is not significant and may even degrade the image quality, as shown in Figure 3-14 (N = 90) and 3-16 (N = 120). For example, in Figure 3-16, only a few scattered dots are visible, and the shape of the lung cannot be reconstructed when N equals to 120. In addition, it will slow down the imaging speed.

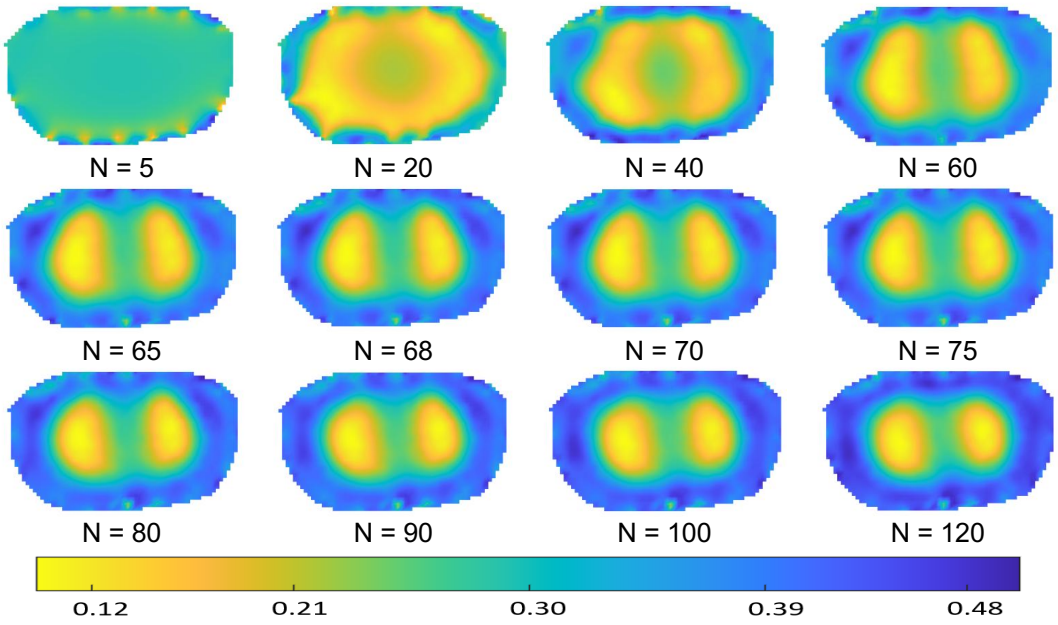

Figure 3-12: Reconstruction images with different iteration at layer -15 cm.

Similarly, too few iterations can cause poor imaging quality too, as illustrated in Figure 3-12 (N = 20), 3-13 (N = 20), and 3-15 (N = 5). For instance, when N is 5, no reconstructed image of any object is visible in the Figure 3-12. It is therefore important to choose a reasonable number of iterations in order to find the best possible results to reconstruct EIT lung images. The optimal number

of iterations will be chosen based on the results of the evaluation parameters, which will be described in detail later in the Section 3.5.

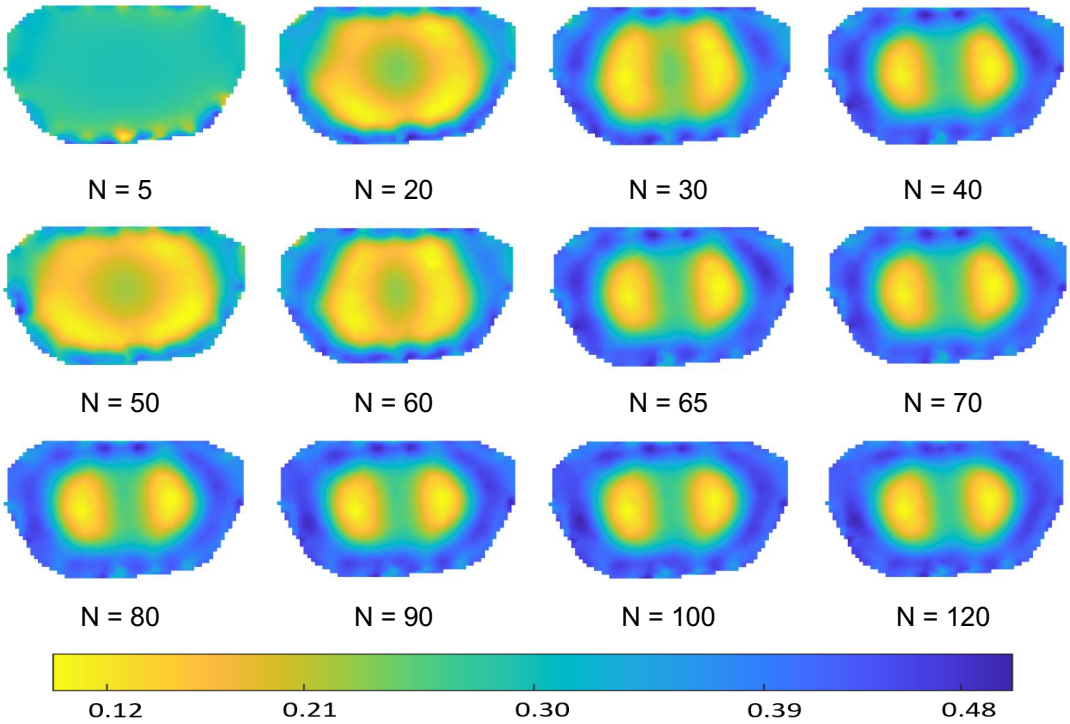

Figure 3-13: Reconstruction images with different iteration at layer -14.5 cm.

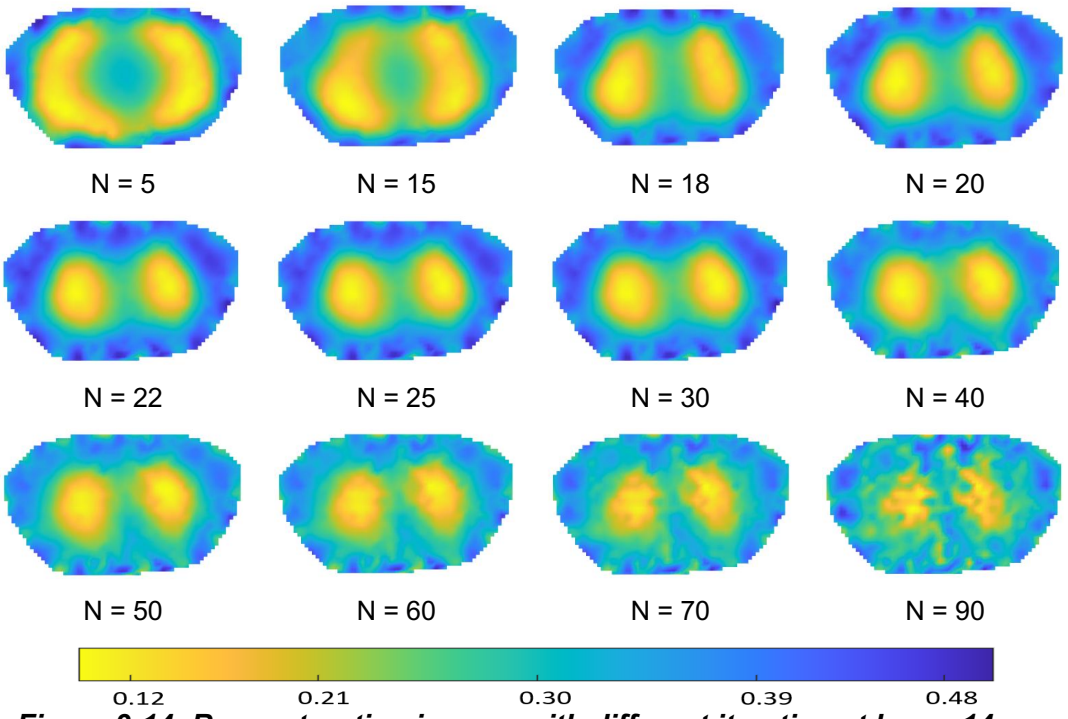

Figure 3-14: Reconstruction images with different iteration at layer -14 cm.

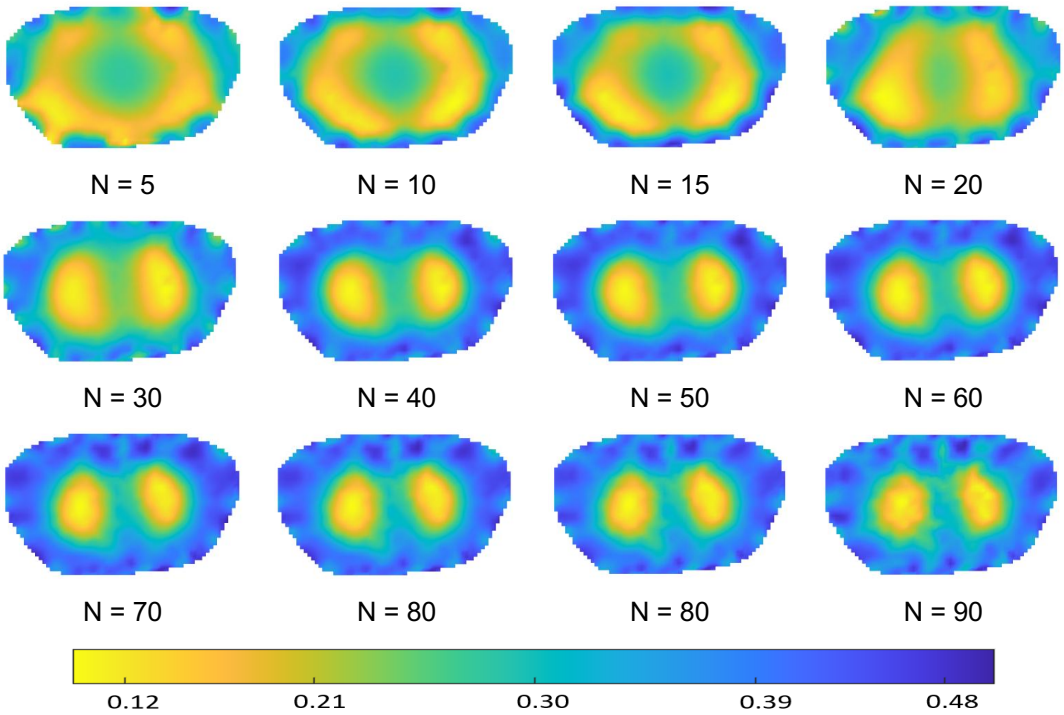

Figure 3-15: Reconstruction images with different iteration at layer -13 cm.

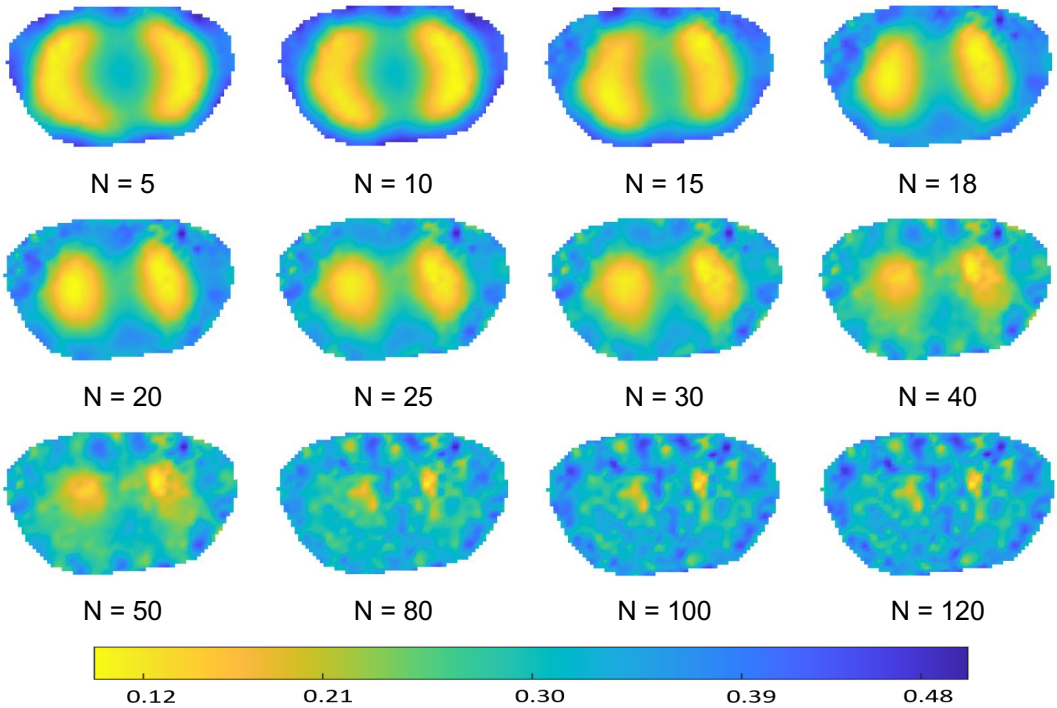

Figure 3-16: Reconstruction images with different iteration at layer -11 cm.

An optimal set of imaging results is shown in Figure 3-17. Usually, the further away from the central layer, the smaller the optimal number of iterations for that layer. Usually, the further away from the central layer, the smaller the optimal number of iterations. The results are obviously able to distinguish

between the left and right lungs, although the contours and shapes of the lungs still deviate from the real model. The solution for this problem will be discussed in following chapters.

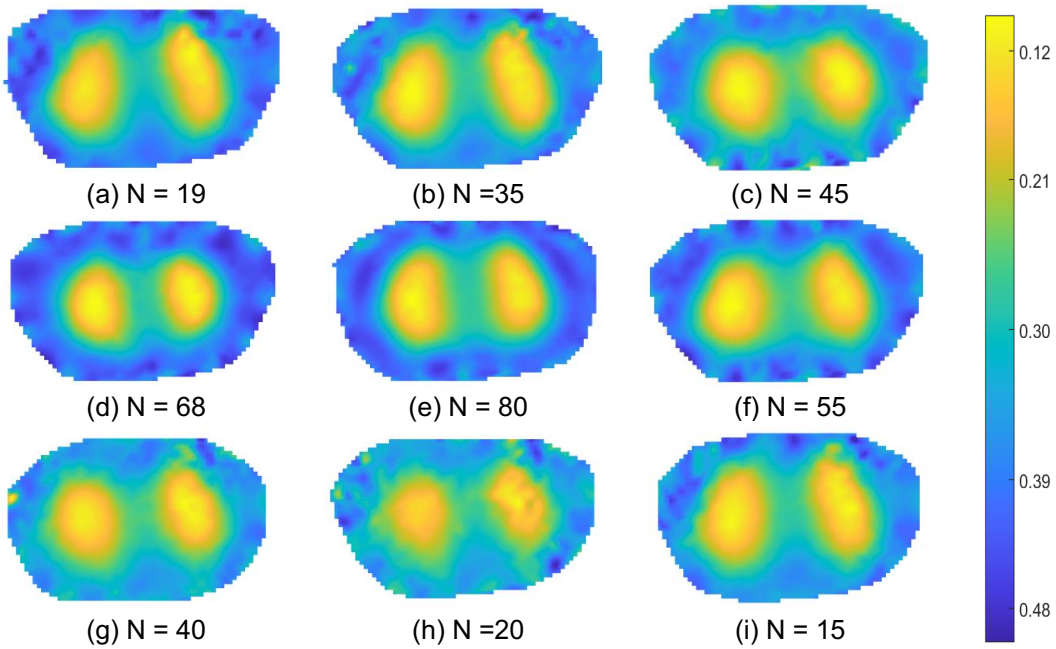

Figure 3-17: Reconstructed images for 9 slices with the optimal number of iterations.

3.3.3 Noise to the signal

Inevitably, measurement data will contain random and systemic noise. In this section, signal to noise ratios (SNR) between 15 dB and 50 dB are applied to test the robustness of image reconstruction algorithm against noise and analyse the impact of noise on the reconstructed image. The results are shown in Figure 3-18.

Overall, the image quality gets better as the SNR increases. The results in the figures are an illustration because noise is added randomly. It can be observed that the contours and position of the lung become progressively clearer when SNR is greater than 30 dB. Additionally, the reconstruction results away from the center layer are noticeably worse than that close to the middle layer. For example, in a layer with a height of -11 cm, it is difficult to reconstruct the lung image when the SNR is 15 dB. However, at a layer with a height of -14.5 cm, the general shape of the lungs can be clearly observed.

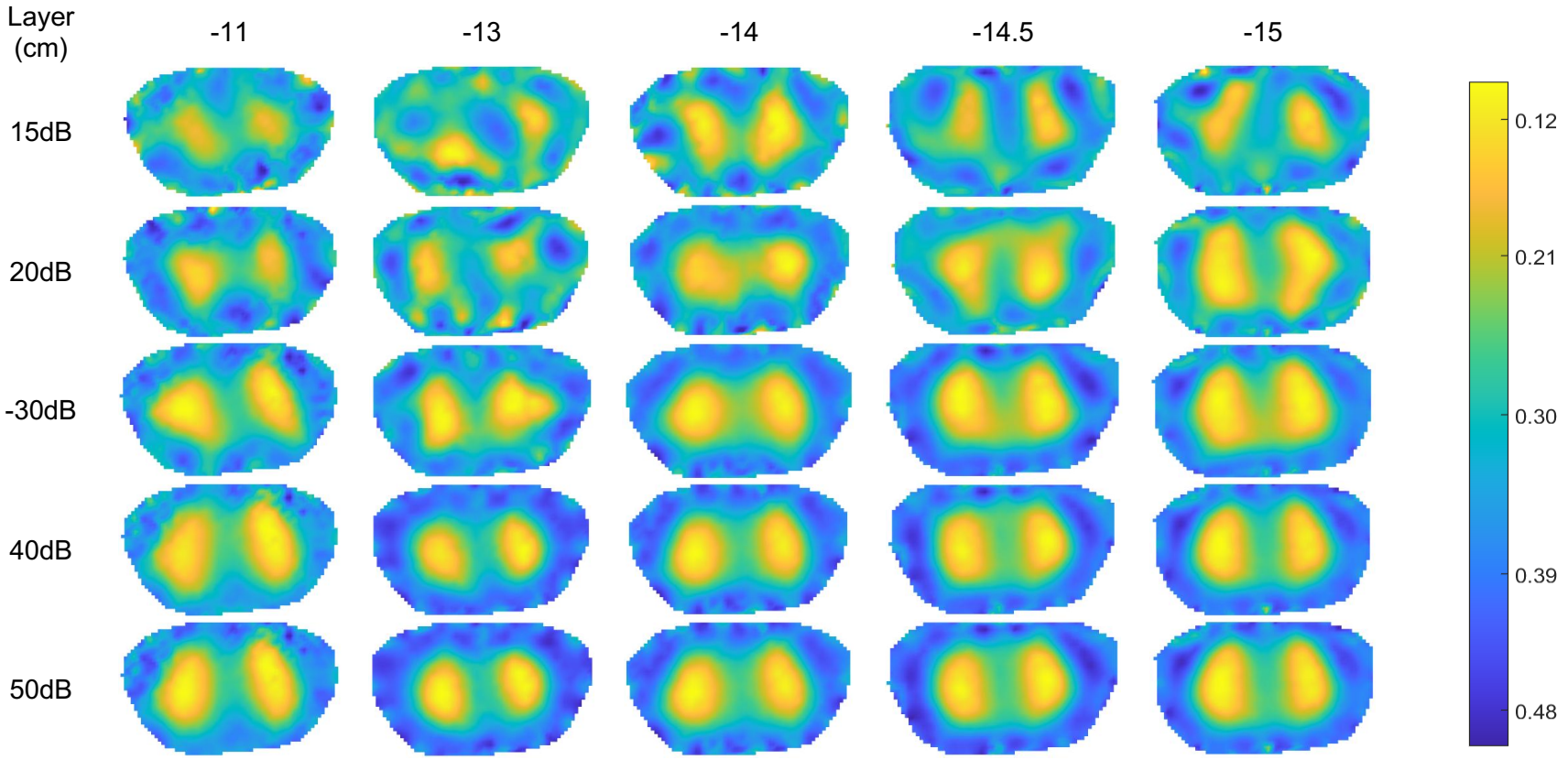

Figure 3-18: The results of different SNR added to different layers.

3.3.4 Evaluation of image reconstruction performances

Many reconstructed images, including those with different layers, different numbers of iterations and different SNR, have been discussed in the previous subsections. The findings of a quantitative analysis are then presented, as illustrated in Figure 3-19 to 3-23. It is obvious that the centre layer produces the finest performance.

With the exception of Figure 3-19, the general trends for CC and SSIM are remarkably similar in that they rise with the number of iterations and eventually converge to a plateau. The fact that this layer is the farthest from the central layer makes Figure 3-19 particularly interesting. According to the results, planes remote from the centre layer are prone to poor imaging, but that a pretty solid result can still be maintained by modifying the number of iterations. Therefore, it is important to find a way to determine the optimal number of iterations.

According to the CC and SSIM, the considerably larger values (near to 1) of them are associated with superior imaging results and can be used to determine the ideal number of iterations. In contrast, a significantly larger RE indicates a poorer imaging quality.

The appropriate number of iterations is typically not too high or too small, but generally in the range of 20 to 80 iterations, according on the results of all the evaluated parameters. Based on the curves in Figure 3-19 to Figure 3-23, it is clear that the optimum number of iterations is not a particular value, but a general range. In Figure 3-19, for example, RE, SSIM and CC are all acceptable values in the curve when the number of iterations is in the interval 18 to 30. Combining the three evaluation parameters, 20 to 25 is considered to be the optimal interval. Therefore, the smallest number of iterations in the usual interval would be considered the best number of iterations, as there would be a relatively short time cost. Based on extensive experimental evidence, the maximum number of iterations is generally around 80 for the central layer, while the lower the number of iterations for layers further away

from the central layer, even 15 is the best result. The same criterion applies to different patients, with the central layer usually having the highest number of iterations and the layers farther from the centre having relatively few iterations.

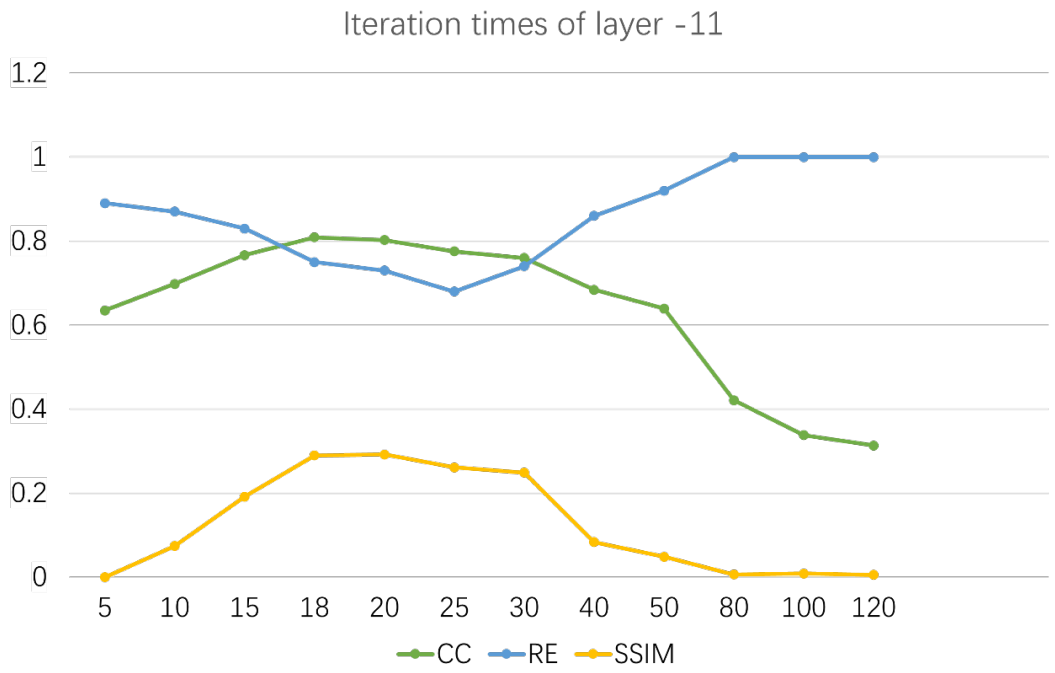

Figure 3-19: Evaluation of the impact of different iteration at the same layer (layer -11 cm).

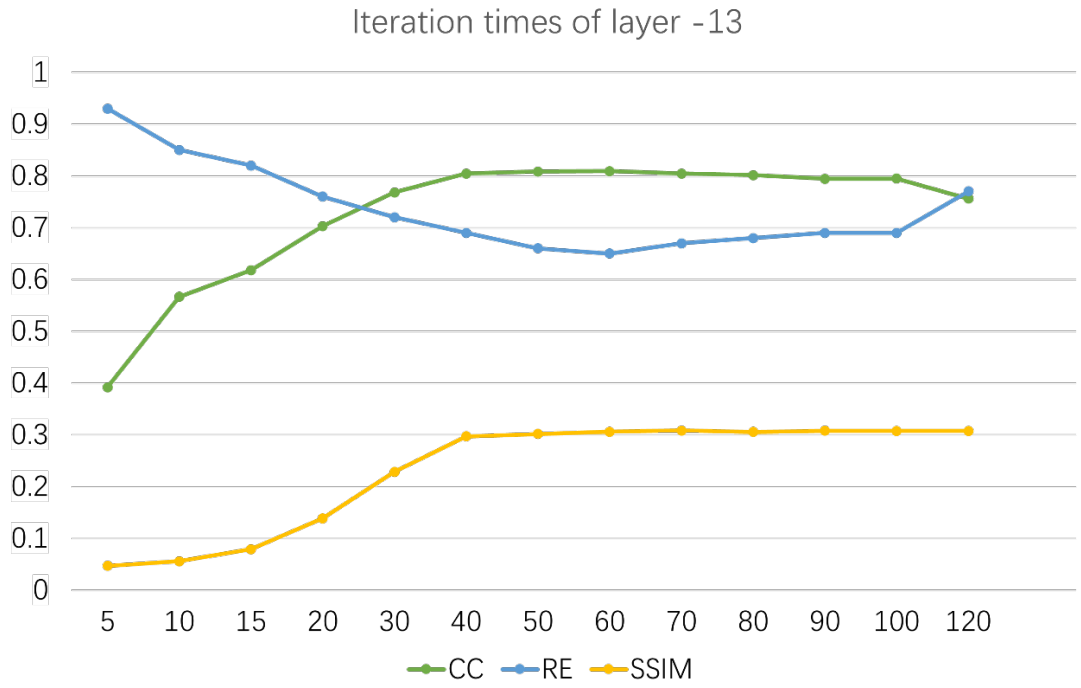

Figure 3-20: Evaluation of the impact of different iteration at the same layer (layer -13 cm).

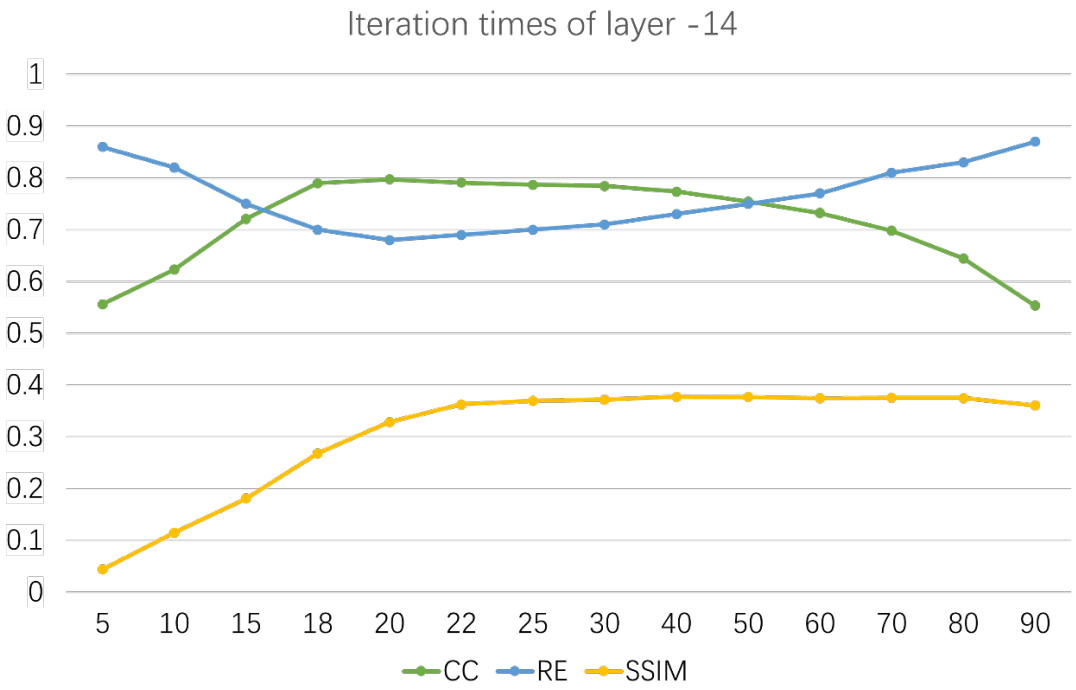

Figure 3-21: Evaluation of the impact of different iteration at the same layer (layer -14 cm).

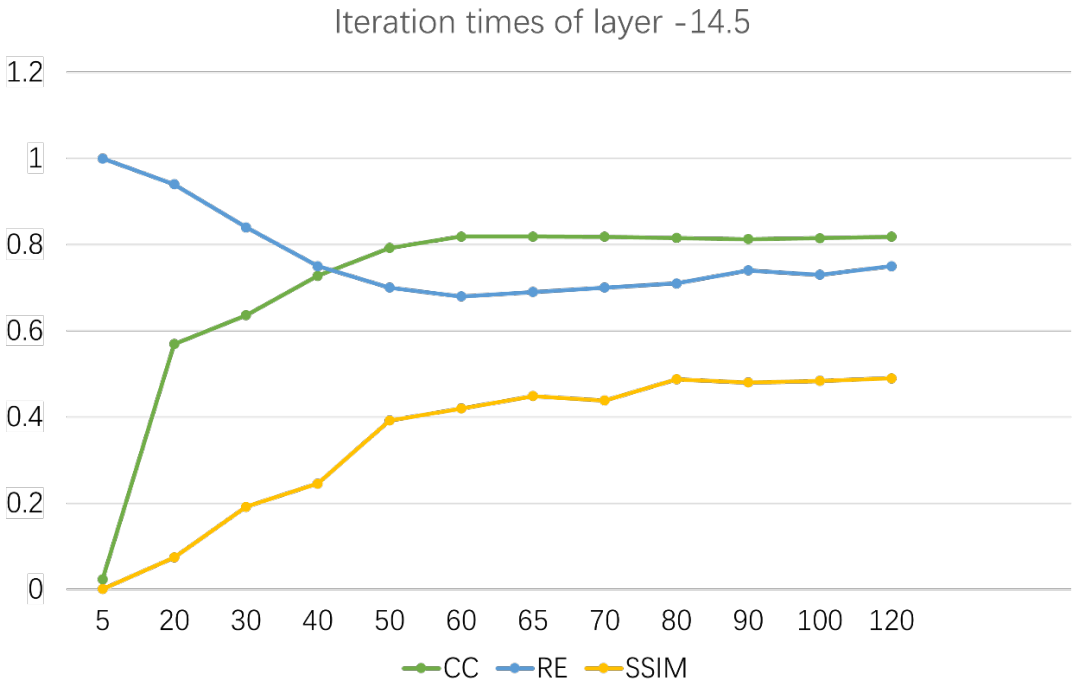

Figure 3-22: Evaluation of the impact of different iteration at the same layer (layer -14.5 cm).

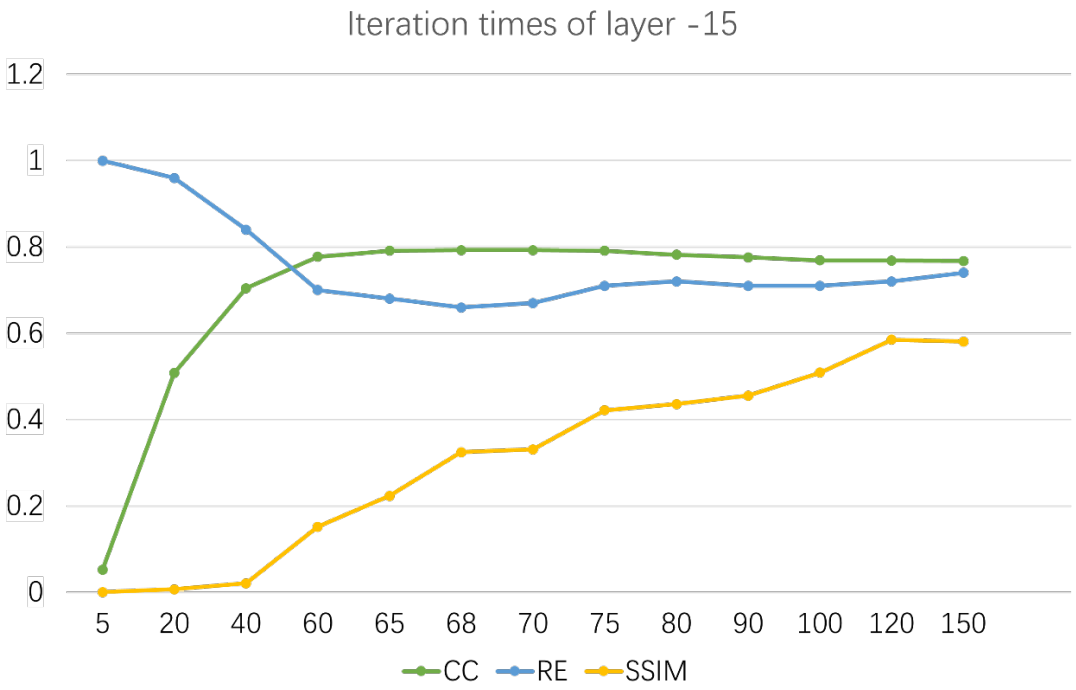

Figure 3-23: Evaluation of the impact of different iteration at the same layer (layer -15 cm).

As demonstrated in Figure 3-24, noise has a significant impact on image reconstruction. The CC gradually improves as the SNR increases. Additionally, it reaffirms the study of the prior section for various imaging heights, according to which the imaging results are improved that the closer the imaging layer is to the central layer.

In spite of this, the CC finally stabilises at a value of about 0.8 and is difficult to enhance further, either by increasing the SNR or reducing the imaging distance. Additionally, the CC fluctuates significantly at layers away from the central layer when the SNR is low, whereas the value of the CC is relatively stable when the noise is low, indicating that it is not sufficiently robust away from the central layer, which may be due to the limitations of algorithm.

According to the discussion in the previous subsection, reconstructing all the slices would be sufficient to obtain a 3D reconstructed image, as shown in Figure 3-25. In the figure, (a) is the model to be reconstructed, (b) is the reconstructed image in the ideal case without noise, and (c) is the

reconstructed image with 30 dB of SNR Although there are still limitations in this study, it is still possible to identify the location and general shape of the lung.

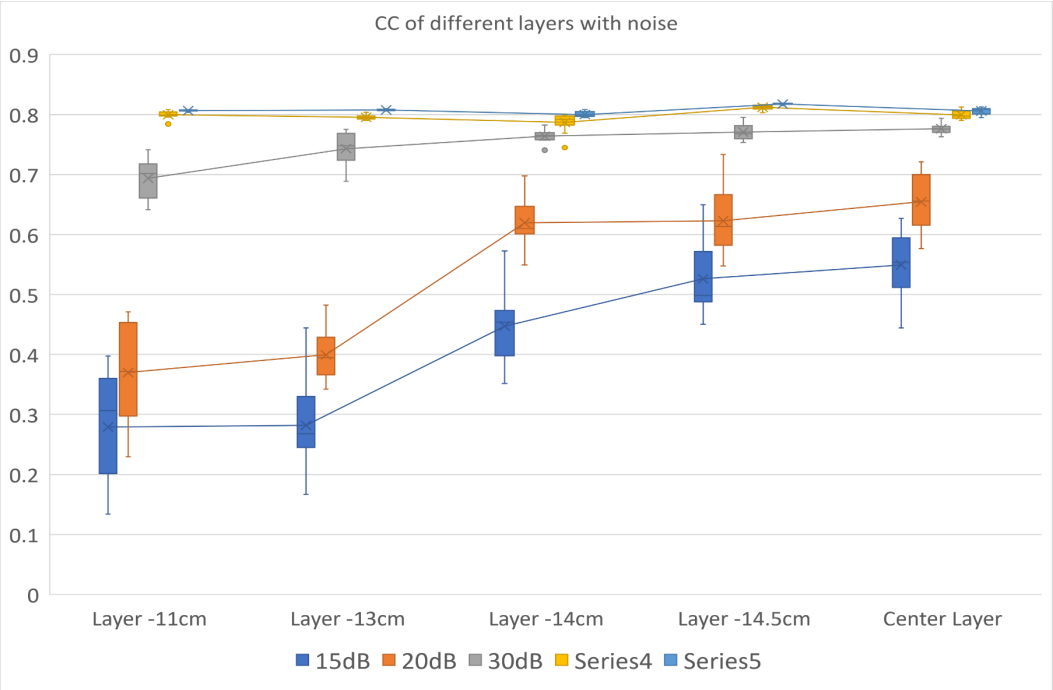

Figure 3-24: CC corresponding to noise.

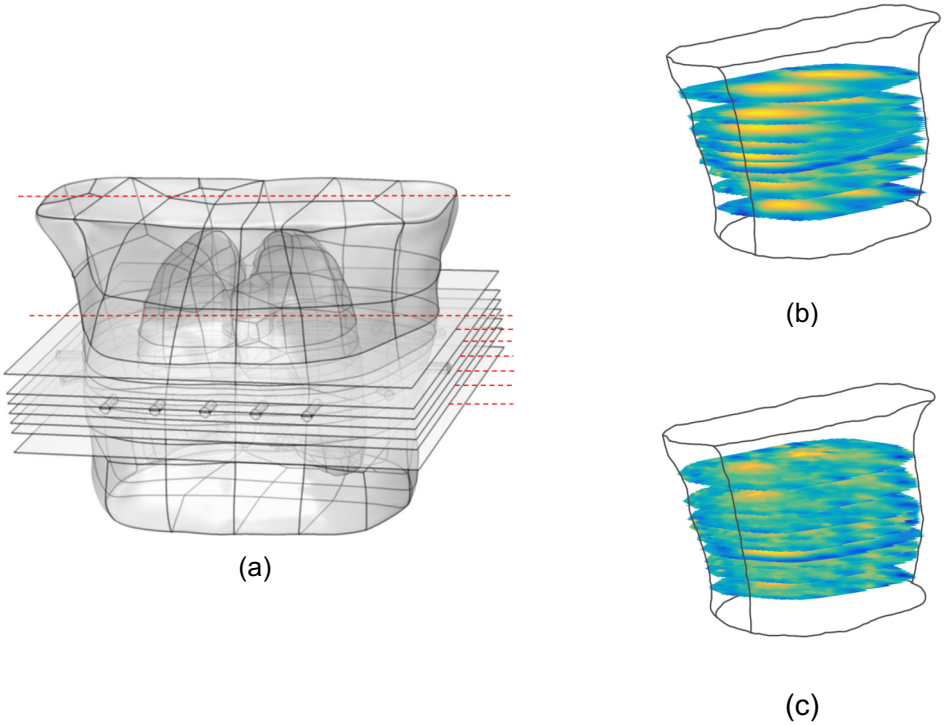

Figure 3-25: 3D reconstruction images.

3.4 Discussion

Depending on performance, the conductivity of various organ and tissues varies and shifts throughout time. As an illustration, the conductivity of the lungs varies from that of the chest cavity. During breathing, the conductivity of the lung changes through changes in the tidal volume within the lung. The more air there is, the lower the conductivity. Impedance measurements can therefore be used to analyse additional information like the function of lung and are ideally suited for application in image reconstruction. Therefore, during prolonged monitoring, the state of the object being reconstructed can be analysed based on changes in conductivity.

The modified sensitive field can be exploited more effectively for reconstructing images. The image quality can be improved by reducing noise and artefacts in the image by eliminating all of the outermost influential points. Good performance can be achieved even in challenging circumstances with low SNR. Despite inadequate imaging of the layers that away from center layer, the approximate location of the lung can still be recognized. The CC of the image could generally be kept around 80%, which is a result that demonstrates the ability of modality to increase imaging speed without sacrificing resolution. More importantly, finding the ideal number of iterations for each layer is essential, as utilizing too many iterations will increase the imaging time. A general rule is that the optimum number of iterations is around 80 for the central layer and gradually decreases for the parts away from the central layer.

3.5 Summary

In this chapter, an improved approach to 3D imaging is presented and the feasibility of a one-layer electrode EIT device for 3D lung imaging is demonstrated. Also, the performance is evaluated under different imaging designs. Dynamic imaging with three reconstruction algorithms is compared in the imaging of the lung. The evaluation showed that CG can provide more information when working at the right number of iterations. Even with a low

SNR, the algorithm can be used to monitor the electrical conductivity of lungs over time. This will help to monitor the working state of lungs.

The findings in this chapter confirm that EIT can be used to monitor changes in the lung, setting the stage for the subsequent chapters, which will be compared with other imaging algorithms in Chapter 4 to further address the issue of unclear imaging boundaries. In Chapter 6, the algorithm proposed in this chapter will be applied to monitor the tidal volume of the lungs and enable control of the ventilator.

Chapter 4 The reliable deep learning scheme for lung reconstruction based on electrical impedance tomography

4.1 Introduction

Due to its high sensitivity to changes in body impedance, EIT is used to visualise living tissue in the body for biomedical imaging applications, as a non-invasive technology [106-109]. As mentioned in Chapter 3, since the conductivity of lung tissue is significantly lower than that of other soft tissues in the chest cavity, EIT is used clinically for chest imaging to monitor lung function and it has been demonstrated to be effective in acquiring pathological information [108, 110, 111]. The main computation goal of EIT is the reconstruction of conductivity distributions based on differential voltage measurements, by resolving the inverse problem [102]. However, the spatial resolution of the EIT is only around 10% of the sensor diameter, which results in poor image quality and prevents its further application in this area [112]. Therefore, it is critical to advance image reconstruction technology which is one of the key goals of both the Chapter 3 and Chapter 4. Due to its non-linearity and ill-posed problem, robust and high-resolution conductivity reconstruction remains difficult despite the fact that numerous solutions have been studied and published over the past few decades [113, 114], especially for accurate reconstruction of the chest region for clinical applications [115]. This chapter discusses innovative deep learning-based image reconstruction techniques to enhance image resolution, decrease artefacts, and optimize image quality.

Recently, with improvements in deep learning theory and hardware computing capacity, an increasing number of academics have looked for novel ways to

use deep learning algorithms to solve nonlinear pathological inverse issues [116]. Seo [117] developed a novel deep learning-based approach for resolving pathological nonlinear inverse issues. For evaluating lung function in 60 patients, Zhu's study developed empty convolution combined with the full convolutional neural network optimization algorithm (ECFCNN) [118]. A lung segmentation approach that is automatic, robust, and rapidly accessible has been developed by Ko, which can be utilised to identify the proper regions of interest (ROIs) in EIT images [119]. To determine the thickness of abdomen subcutaneous fat, Lee stated a deep learning algorithm based on EIT [120]. For pathological image processing tasks including tumour location identification, tumour microenvironment characterisation, and metastasis detection, deep learning has also demonstrated considerable potential. An overview of existing and future advantages of AI approaches in pathological image processing is covered in this topic [121], with an emphasis on lung cancer. Several typical deep reinforcement learning models that can be applied to the detection of lung cancer are demonstrated by Liu [122]. On the basis of lung CT images, two CNN-based models for deep learning were presented [123]. The suggested method of Wu, especially in the presence of measurement noise and interference, achieved excellent resolution and trustworthy shape reconstruction for EIT lung imaging [84].

UNet is one of the most important segmentation frameworks for CNN, which is a technique mainly used for medical image segmentation tasks in the CT, MRI, and X-ray fields [124]. For kernel segmentation, the RIC-UNet (residual-inception-channel attention-UNet) neural network was proposed by Zeng et. al. in 2019 [125]. In order to remove artefacts from 2D PAT images that were reconstructed from sparse data, Guan proposed an improved CNN architecture called fully dense UNet (FD-UNet) and compared the proposed CNN with the standard UNet in terms of the quality of the reconstructed images [126]. In 2020, Huang illustrated a novel UNet 3+ that exploited supervision

and full hopping connection [127]. Swin-UNet, a pure UNet-like transformer for medical image segmentation, was proposed by Cao [128].

Many deep learning algorithms have been proposed for solving the inverse problem of EIT and for improving resolution and robustness. However, existing models, some of which cause artefacts, blur the boundaries. Therefore, further improvements are still needed in terms of reconstructing clear lung contours and in reconstructing image accuracy. The technique presented in this section is the first to be utilised with EIT and lung images, and it concentrates on image reconstruction using fused UNet networks. Although the spatial resolution of CT and MRI is very high, CT is radioactive and cannot monitor detected object in real time. In addition, MRI, although free of radiation, is expensive and cannot be applied to specific patients with magnetic metal or pacemakers in their bodies. Therefore, the fused UNet strategy in conjunction with EIT images for medical imaging can perfectly avoid the drawbacks of CT and MRI, while improving the image quality of EIT and enhancing the usability of EIT devices. The principles of the hybrid UNet network are introduced in detail. Moreover, to confirm the calibre of the images and the accuracy of the outcomes, simulations of ordinary lung and aliquot slices are performed.

4.2 Method

This chapter focuses on a UNet-like architecture that was presented at the MICCAI conference in 2015 [129] as a classical network practical technique for biomedical image segmentation. The core concept behind UNet is to initially map an image to a vector before reconstructing it back into an image. The fundamental concepts of UNet are extended across to the network architecture that is developed in this chapter, which also includes additional modules and design ideas. More thorough description of the two enhanced versions is discussed below.

4.2.1 DSA-UNet

As shown in the Figure 4-1, there is a 3×3 convolution layer and a 3×3 Depthwise Separable Convolution (DSC) block on the left hand of the UNet, which is applied for contraction, with a 2×2 max pooling in each step. Moreover, the 2×2 upsample layer has been used at the bottom layer after convolutions. In the expansion process on the right, the relevant feature maps from the contraction part are employed again to lessen image distortion. They are combined directly after the layer of upsampling. The self-attention block has been applied to capture key information. After the final 3×3 Depthwise Separable Convolution block operation, a 1×1 convolution block with a sigmoid is combined for classification.

This novelty network has three important components in addition to the UNet, namely the depthwise separable convolution, self-attention and the initialized full connection. The input size and output size for each layer have been demonstrated in Table 4-1.

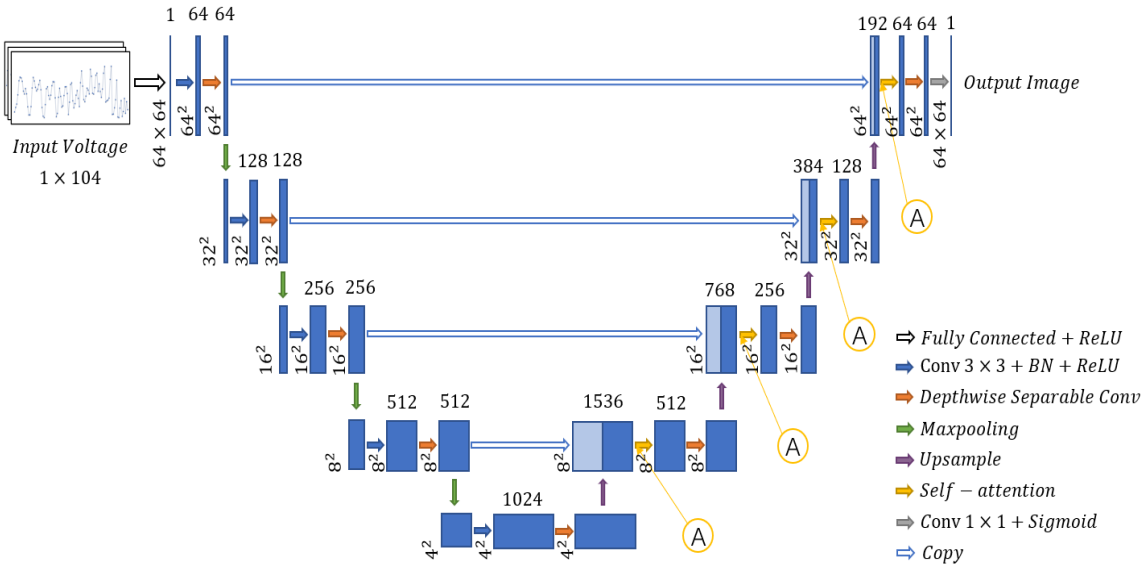

Figure 4-1: The architecture of the DSA-UNet reconstruction algorithm.

Table 4-1: The size of the compoment for each layer.

Block	Input size	Layer	Output size
Input-1	1*1*104	Fully connected + ReLU	1*1*3228
Input-2	1*1*3228	Reshape	64*64*1
1-1-1	64*64*1	Conv 3*3 + BN +ReLU	64*64*64
1-1-2	64*64*64	DSA conv 3*3 + BN + ReLU + Max pool	32*32*64
1-2-1	64*64*192	Self-attention + Conv 3*3 + BN + ReLU	64*64*64
1-2-2	64*64*64	DSA conv 3*3 + BN + ReLU	64*64*64
1-2-3	64*64*64	Conv 1*1 + Sigmoid	64*64*1
1-2-4	64*64*1	Reshape	1*1*3228
2-1-1	32*32*64	Conv 3*3 + BN +ReLU	32*32*128
2-1-2	32*32*128	DSA conv 3*3 + BN + ReLU + Max pool	16*16*128
2-2-1	32*32*384	Self-attention + Conv 3*3 + BN + ReLU	32*32*128
2-2-2	32*32*128	DSA conv 3*3 + BN + ReLU + Upsample + copy	64*64*192
3-1-1	16*16*128	Conv 3*3 + BN +ReLU	16*16*256
3-1-2	16*16*256	DSA conv 3*3 + BN + ReLU + Max pool	8*8*256
3-2-1	16*16*768	Self-attention + Conv 3*3 + BN + ReLU	16*16*256
3-2-2	6*16*256	DSA conv 3*3 + BN + ReLU + Upsample + copy	32*32*384
4-1-1	8*8*256	Conv 3*3 + BN +ReLU	8*8*512
4-1-2	8*8*512	DSA conv 3*3 + BN + ReLU + Max pool	4*4*512
4-2-1	8*8*1536	Self-attention + Conv 3*3 + BN + ReLU	8*8*512
4-2-2	8*8*512	DSA conv 3*3 + BN + ReLU + Upsample + copy	16*16*768
5-1-1	4*4*512	Conv 3*3 + BN +ReLU	4*4*1024
5-1-2	4*4*1024	DSA conv 3*3 + BN + ReLU + Upsample + copy	8*8*1536

a) Depthwise Separable Convolution

In order to extract feature maps, a convolution operation known as Depthwise Separable Convolution (DSC) is performed in two steps: Depthwise Convolution and Pointwise Convolution. Compared with a normal CNN, DSC method can reduce the number of parameters and the cost of operation. In other words, DSC can do deeper convolution with the same number of parameters. The normal convolution block and DSC block have shown in the Figure 4-2.

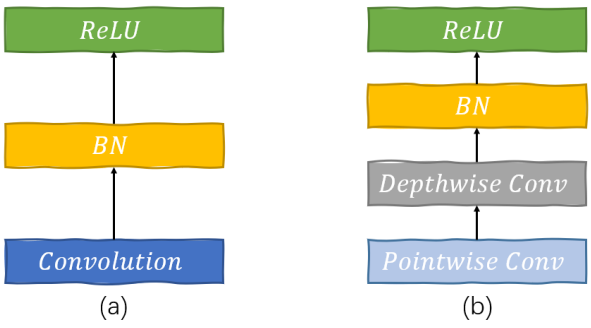

Figure 4-2: Two different convolution block in the DSA-UNet. (a) Normal convolution block. (b) Depthwise separable convolution block.

In traditional convolution, each convolution kernel operates on each channel of the input image simultaneously. However, in depthwise convolution, each convolution kernel is responsible for one channel, and each channel is convolved by only one convolution kernel, as shown in Figure 4-3. Therefore, in depthwise convolution, the number of convolution kernels is the same as the number of channels in the previous layer, resulting in a corresponding number of feature maps [130].

The number of convolution kernels for depthwise convolution can be calculated by the Equation 4.1.

$$N_{DSC} = k^2 \cdot c_{in} \cdot h \cdot w + c_{in} \cdot c_{out} \cdot h \cdot w \tag{4.1}$$

where $c_{in} \cdot h \cdot w$ is an input feature map, and k^2 stands for the kernel size. The spatial dimension of the kernel is k. In addition, $c_{out} \cdot h \cdot w$ represents the output feature map with height h and width w.

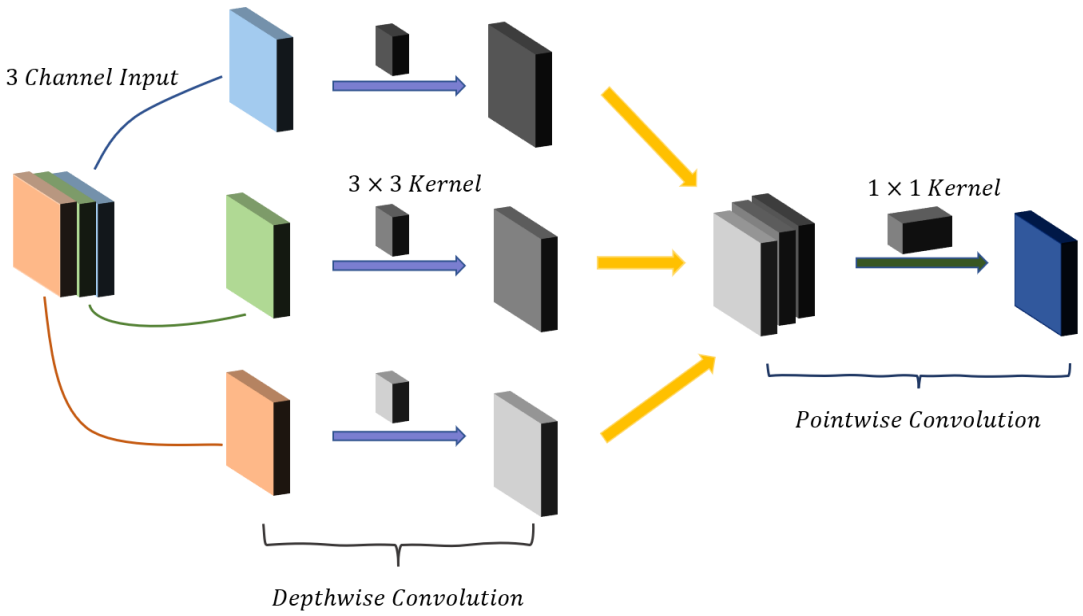

Figure 4-3: Depthwise Separable Convolution. Image and kernel are broken into three different channels for example and convolved separately.

Following the depthwise convolution, a pointwise convolution is used as a weighted combination of the feature map in the depth direction to generate a new feature map and fuse the feature map from depthwise convolution. In

addition, pointwise convolution has the ability to change the number of output channels, with the 1*1 kernel size. Therefore, the number of the feature map is same to the number of kernels.

b) Self-Attention

Attention is a kind of Transformer. It can filter out a small amount of essential information from innumerable information, and ignore the mostly unimportant information. Therefore, the complexity of the model which is limited by computational power would be avoided. The value of the weight represents the importance of the information [131]. In addition, the self-attention reduces the reliance on external information and is good at capturing the relevance within the data and features. The structure of self-attention is shown in Figure 4-4.

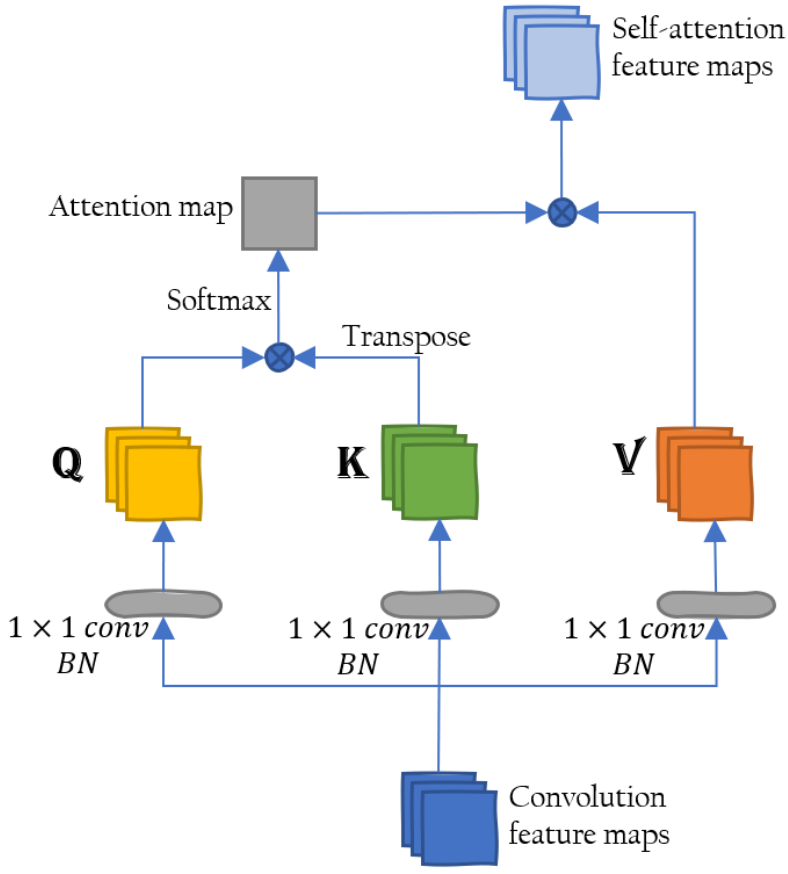

Figure 4-4: The self-attention mechanism in DSA-Unet.

The weight distribution of value can be determines by the degree of similarity between query and key in the self-attention, according to the Equation 4.2 and Equation 4.3.

$$Attention(\boldsymbol{Q}, \boldsymbol{K}, \boldsymbol{V}) = softmax\left(\frac{\boldsymbol{Q}\boldsymbol{K}^T}{\sqrt{d_{\boldsymbol{k}}}}\right)\boldsymbol{V} \tag{4.2}$$

$$Softmax(z_i) = \frac{e^{z_i}}{\sum_{c=1}^{C} e^{z_c}} \tag{4.3}$$

where z_i is the output value of i^{th} node, and C is the number of the output node.

c) Full Connection Block

In order to relate the model to its actual physical meaning, this section propose to initialize the weights of the fully connected layer with the least squares solution (LS) of the linear function, using training data rather than random weights.

$$\Delta \boldsymbol{V} = \boldsymbol{J}\Delta\boldsymbol{\sigma} \tag{4.4}$$

Since matrix multiplication is always achieved by introducing a fully connected layer in principle, the fully connected layer would be followed by a ReLU layer.

4.2.2 RP-UNet

Rep-PSA-UNet (RP-UNet) is a completely new design, in addition, it is the first time this network has been proposed and applied to the field of image segmentation for medical imaging. This unique network structure is completely different from the DSA-UNet described above, which improves computational power by changing the convolution method, thus reducing the number of parameters in the network. In contrast, the structure of RepVGG in RP-UNet is implemented by the structural re-parameterization technique. In RP-UNet, two parts of the innovation are incorporated. The original 3×3 convolution module in UNet has been replaced in entirety with the RepVGG module.

Moreover, parallel polar self-attention is incorporated to solve the pixel-level regression task, as shown in Figure 4-5, and the two innovative parts are described in detail below.

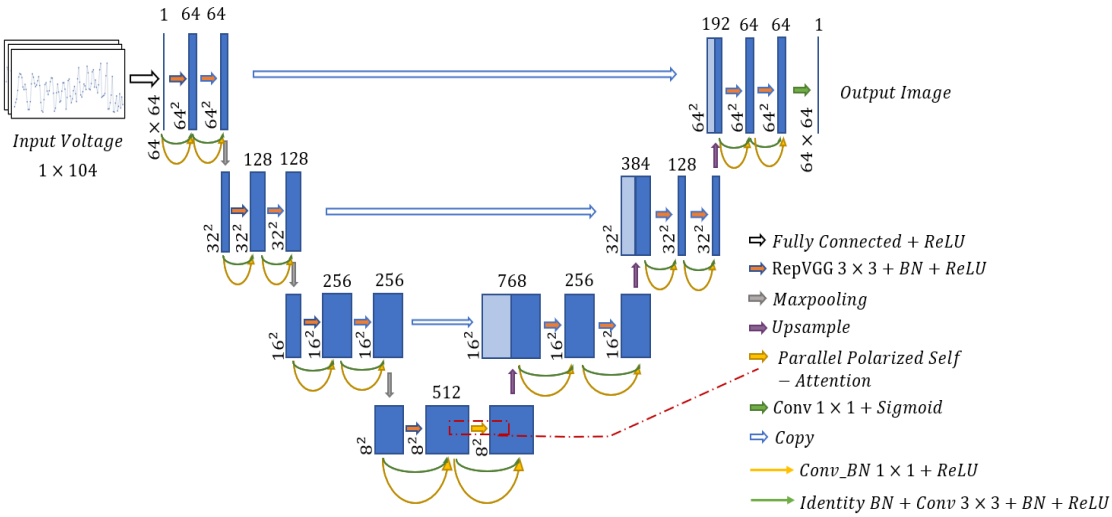

Figure 4-5: The network structure of RP-UNet.

a) RepVGG Block

According to the work of Ding, the structured re-parameterization technique had been mentioned as using a ResNet-like multi-branch model during training, yet transformed into a single-way VGG model during inference [132]. As shown in the Figure 4-6, (a) is the structure of ResNet, (b) is the structure of the training model of RepVGG, and (c) is the inference model, respectively. Inspired by the ResNet, the structural of (b) changes the addition branch. The original addition branch is added to the main body between every two or three layers, while adding branches exist between each layer in the new structure. By combining a parallel 1×1 convolution and a constant mapping branch to the 3×3 convolutional layer, which forms one of the main parts of this structure, the RepVGG block. It can be seen that the (c) in Figure 4-6, as the validation network, equates the original multi-branch model to a single-way model, not only taking advantage of the high performance obtained from the

multi-branch training process, but also increasing the speed in the process of inference about the single-branch model.

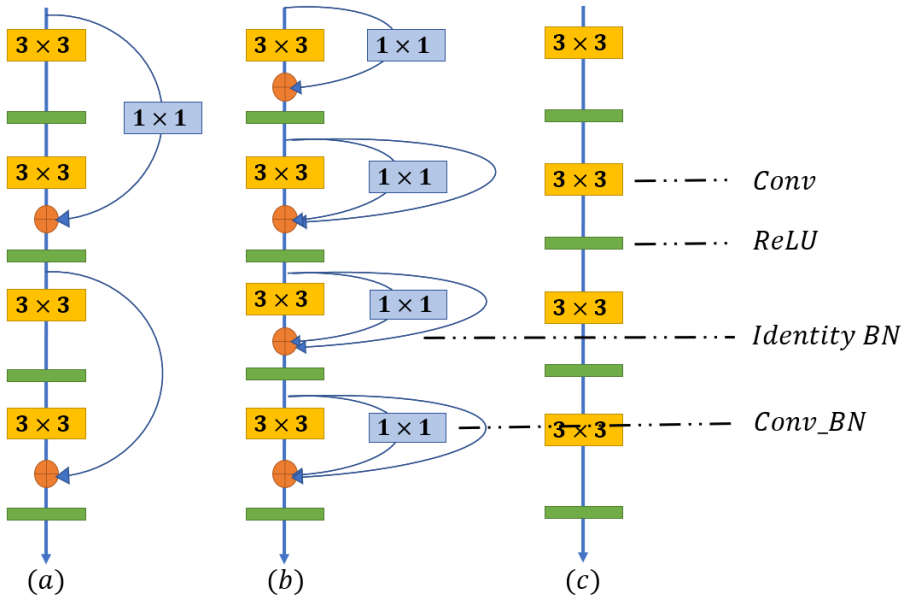

Figure 4-6: The structure of RegVGG. (a) ResNet. (b) Training model of RepVGG. (c) RepVGG inference.

Not only that, but after the conversion of the multi-branch to a single-branch model, Conv2d and BN are fused, which makes the computation smaller. The existing hardware conditions are generally heavily optimised for 3×3 convolution operations, so as can be seen in Figure 4-6 (c), the conversion to a single-branch model uses 3×3 convolution, which can further speed up inference.

The structural re-parameterization technique describes precisely the transformation of the trained RepVGG block into an inference model. There are two steps, as shown in Figure 4-7. First of all, fuse cond2d with bn and transform the separate bn layers into conv2d. The 3×3 convolution layers of each branch are then fused into one convolution layer, as convolution has cumulative properties.

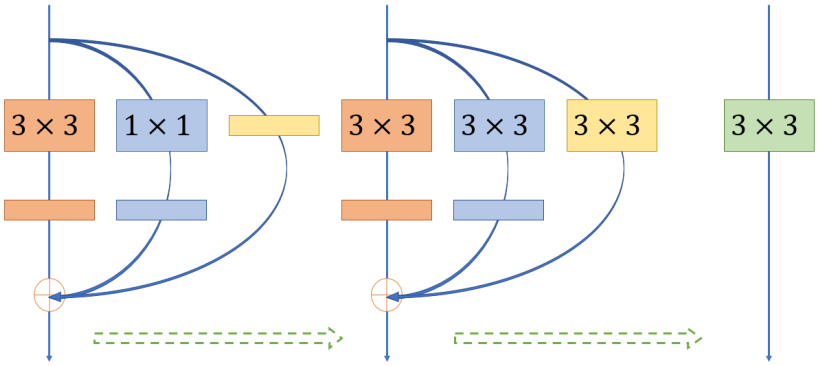

Figure 4-7: The process of converting multi-path training model to single-path test model.

In this conversion process, the essence of structural re-parameterisation can be explained. The structure for training corresponds to a set of parameters, and the structure for inference corresponds to another set of parameters. The structure of the former can be equivalently converted to the latter as long as the parameters of the former can be equivalently converted to the latter, according to the equations shown below. The equation for computing the convolution is,

$$Conv(\boldsymbol{x}) = W(\boldsymbol{x}) + b \tag{4.5}$$

and the equation for BN layer is,

$$BN(\boldsymbol{x}) = \gamma * \frac{(\boldsymbol{x} - mean)}{\sqrt{var}} + \beta \tag{4.6}$$

Bringing the results of the convolution into Equation 4.6, the fused BN can be obtained.

$$BN\big(Conv(\boldsymbol{x})\big) = \frac{\gamma * W(\boldsymbol{x})}{\sqrt{var}} + \left(\frac{\gamma * (b - mean)}{\sqrt{var}} + \beta\right) \tag{4.7}$$

$$BN\big(Conv(\boldsymbol{x})\big) = W_{fused}(\boldsymbol{x}) + B_{fused} \tag{4.8}$$

where γ and β can be obtained from training.

b) Parallel Polarized Self-Attention

The tensor connecting the encoder and decoder in the UNet is usually small in spatial dimension, which can cause some impairment of performance. Therefore, the polarized self-attentive (PSA) module is added to the network to handle the pixel-level regression task. Compared to other attention mechanisms, the PSA has two main design highlights as followed.

Polarized filtering: maintaining a relatively high resolution in the channel and spatial dimensions (C/2 dimensionality in the channel and [H, W] dimensionality in the space), that reduces the loss of information due to dimensionality reduction.

Enhancement: a non-linear function of the output distribution using fine-grained regression.

The structure of the PSA is shown in Figure 4-8.

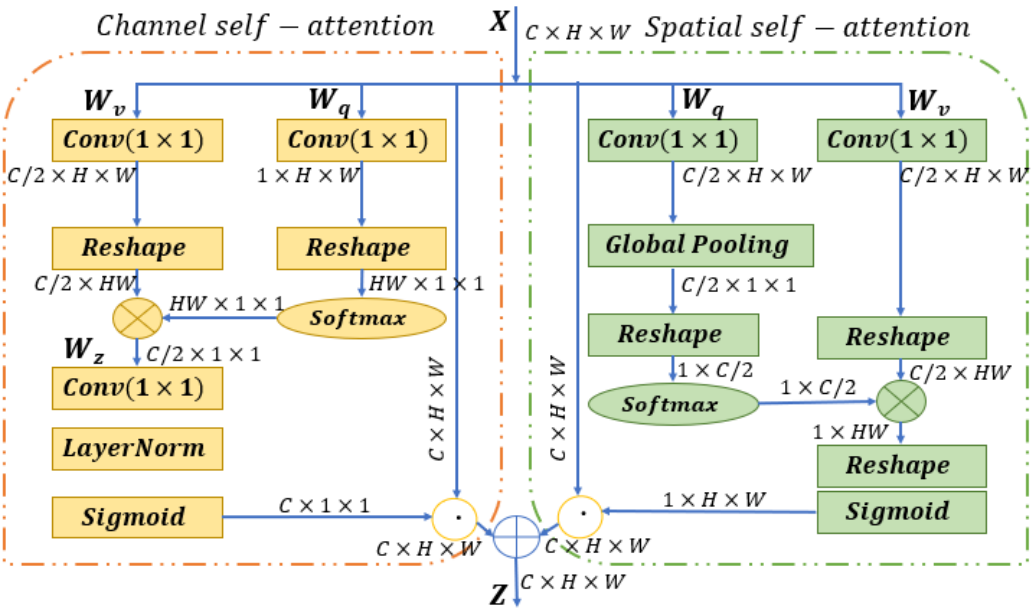

Figure 4-8: The structure of Parallel Polarized Self-Attention block.

4.2.3 Loss function

In this section, the mean square error (MSE) and L1 is adopted as the loss function, which is mathematically defined as the Equation 4.9 and Equation 4.10.

$$L_{MSE} = \frac{1}{2}\sum_{K=1}^{K}\left\|\Delta\boldsymbol{\sigma}_{real} - \Delta\boldsymbol{\sigma}_{pred}\right\|^2 \tag{4.9}$$

where L_{MSE} is the loss function of the DSA-UNet, K stands for the number of real conductivities, which is 3228. In addition, $\boldsymbol{\sigma}_{pred}$ is the estimated value under the DSA-UNet.

$$L_1 = \sum_{i=1}^{N}|\boldsymbol{Y}_i - f(\boldsymbol{x}_i)| \tag{4.10}$$

where $\boldsymbol{Y}_i$ is the i^{th} target value and $f(\boldsymbol{x}_i)$ means the i^{th} estimated value, which is applied for RP-UNet.

4.3 Experimental setup

4.3.1 Dataset

The measured voltages of the dataset were generated from the CT images of 19 patients, as shown in Figure 4-9. Firstly, 19 CT images were acquired and then the contours of the lungs were obtained based on a global threshold image segmentation algorithm. Based on the acquired lung contour information, different lung models were built, including simulated normal lungs and lungs with disease. For different lung diseases, such as pneumothorax, pulmonary oedema and pleural effusion, there are different lung cut methods and different conductivity.

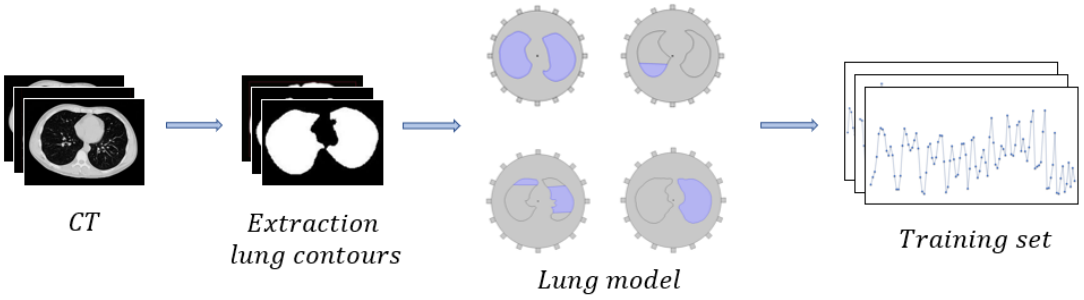

Figure 4-9: The progress of generating the lung EIT dataset.

The forward and inverse finite element meshes used in the joint COMSOL and MATLAB simulation are shown in Figure 4-10 and consist of 3312 regions and 335 boundary elements, and 3228 elements, respectively. Then the measurement voltage can be obtained as input of the net. Increasing the dataset by changing the conductivity of the lungs. In addition, the Gaussian White Noise had been added into dataset with 50 dB and 40 dB. Finally, the size of the dataset is 72585, which is divided by the ratio of 6: 2: 2, as shown in the Table 4-2.

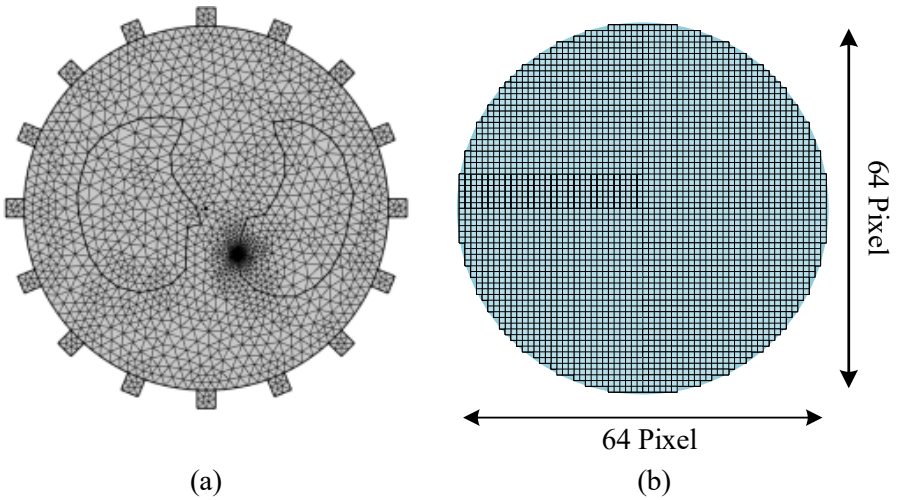

Figure 4-10: Forword and inverse finite element meshes (FEM). (a) Forward mesh made up of 3312 domain elements and 335 boundary elements. (b) Inverse grid consisting of 3228 elements.

Table 4-2: The size of dataset for training, validation and test.

	Training data	Validation data	Test data
size	43551	14517	14517

To improve the accuracy of the model, the measured voltage and conductivity will be normalised.

$$\Delta V = \frac{V_{mear} - V_{ref}}{V_{ref}} \tag{4.10}$$

$$\Delta \boldsymbol{\sigma} = \frac{\boldsymbol{\sigma}_{reco} - \boldsymbol{\sigma}_{ref}}{\boldsymbol{\sigma}_{ref}} \tag{4.11}$$

4.3.2 Optimizer

Adam has been used for optimization. In addition, the initial learning rate is 0.0001, which decays with a factor of 0.1. The model is trained with a back size of 64. All the experiments are implemented based on NVIDIA RTX A5000, Intel(R) Xeon(R) W-2265 CPU (3.50 GHz) and 128 GB RAM.

4.4 Results

4.4.1 Learning curves

The learning curves of two different UNet-like model, DSA-UNet and RP-UNet, have been demonstrated in the Figure 4-11 and Figure 4-12, respectively.

The blue line is the loss during training and the orange line is the loss during validation, both of them are dropping rapidly at first and then levelling off, with some fluctuations. As can be seen from Figure 4-11, in the first epoch, the value of loss was the largest in both training and validation, even exceeding 20. As the model continues to learn and update its parameters, it falls below 0.3 in the eleventh epoch and eventually is stabilised at around 0.1.

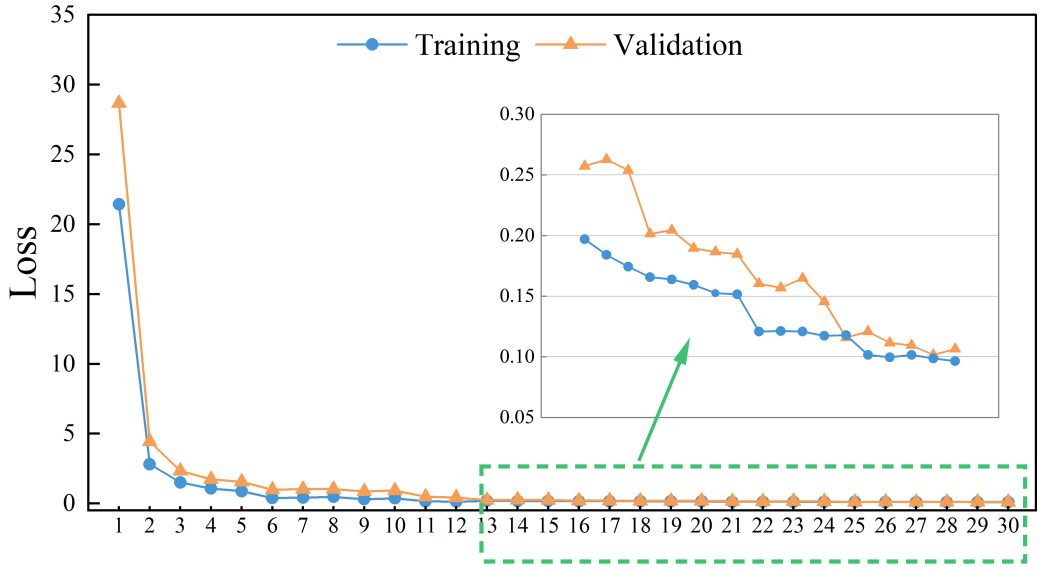

Figure 4-11: The learning curves of the training data and validation data based on DSA-UNet.

In Figure 4-12, the training and validation loses are the solid blue line and the solid orange line, respectively. Finally, these two curves are stabilised below 0.005, even though the validation results are a little worse than the training results. Compared to the results of loss results of DSA-UNet, the starting point of the loss RP-UNet is relatively much lower, while the asymptotic line at the end point corresponds to a very low loss. This proves that a better starting point for training is provided by RP-UNet, especially RepVGG, which helps to learn the model faster and also improves the performance of the model.

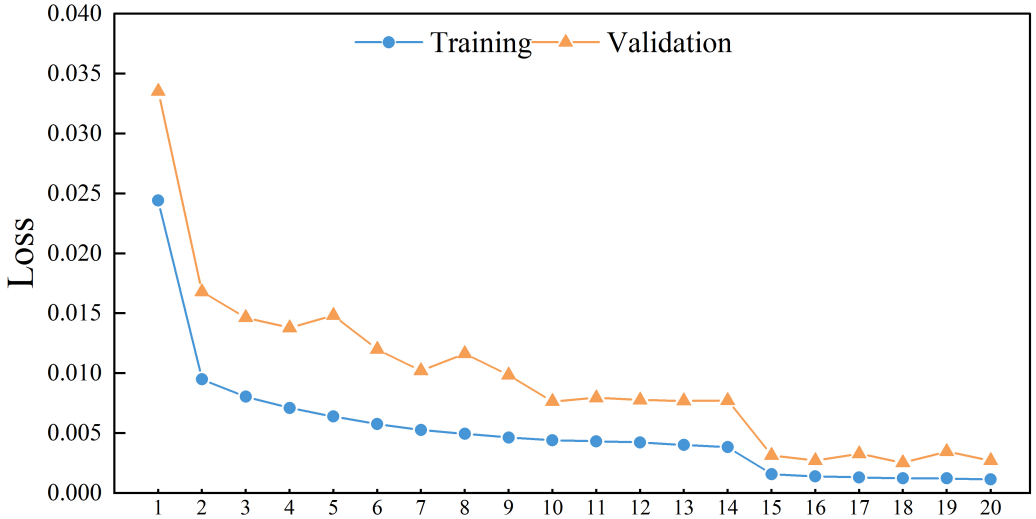

Figure 4-12: The learning curves of the training data and validation data based on RP-UNet.

4.4.2 Image reconstruction with simulation data

In this section, different models were compared and quantitatively analysed, including FC-UNet, LeNet, MLCNN, Deeplabv3-FC, Swin-UNet, CG, and the network models designed in this chapter, RP-UNet and DSA-UNet, as demonstrated in the Table 4-3.

Table 4-3: Evaluation for different reconstruction algorithms.

Algorithm	SSIM	RE	CC
RP-UNet	0.9699	0.1800	0.9727
DSA-UNet	0.9416	0.2378	0.9592
FC-UNet	0.9117	0.3041	0.9216
LeNet	0.9103	0.3252	0.9020
MLCNN	0.8934	0.3628	0.9007
Deeplabv3_FC	0.9149	0.3037	0.9332
Swin-UNet	0.9221	0.2967	0.9365
CG	0.5918	0.7618	0.8088

Based on the table, it can be observed that both models proposed in this chapter, whether SSIM, RE or CC, perform much better than the other models, especially the CG of the traditional algorithm. Therefore, these two models have a better performance on medical image segmentation. Moreover, it also confirms that the Section 4.2 is correct in the understanding of the models. Furthermore, although the other deep learning algorithms do not perform as well as those two proposed, they still outperform CG, particularly SSIM and RE. Therefore, deep learning and data driven are the future trend to increase the performance of medical image segmentation and construction, in particular for needs with complex structures and high resolution.

The image reconstruction results for the different algorithms are shown in Figure 4-13, which illustrates the lung reconstruction results for the six reconstruction algorithms for four different lung injuries, including normal lungs.

In the first column, which is the ground truth of the images, it can be seen that, as presented in the database, the different pathologies are simulated by segmenting the lung and assigning different conductivities to different regions, including normal lung case, Pleural, Pulmonary, as well as Pneumothorax. According to the conventional algorithm CG, the location of the lung is evident in all the reconstruction images, but it is difficult to distinguish the type of disease from the small conductivity changes. Not only is it difficult to distinguish between different regions within the lung, but it is also difficult to obtain an accurate lung shape. As a result, the results of conventional methods are more suited to qualitative rather than quantitative analysis. The remaining models with deep learning can demonstrate the general contour of the lung, but the boundaries are blurred in DeepLabV3-FC and the resolution is low. Artefacts are present in the reconstructed images of UNet and LeNet, but different regions within the lung can be distinguished. In conclusion, the best imaging results were obtained with DSA-UNet, with significantly sharper boundaries and resolution than the other models. The results of Swin-Unet are also good, but still slightly inferior compared to DSA-UNet, because of the inhomogeneity.

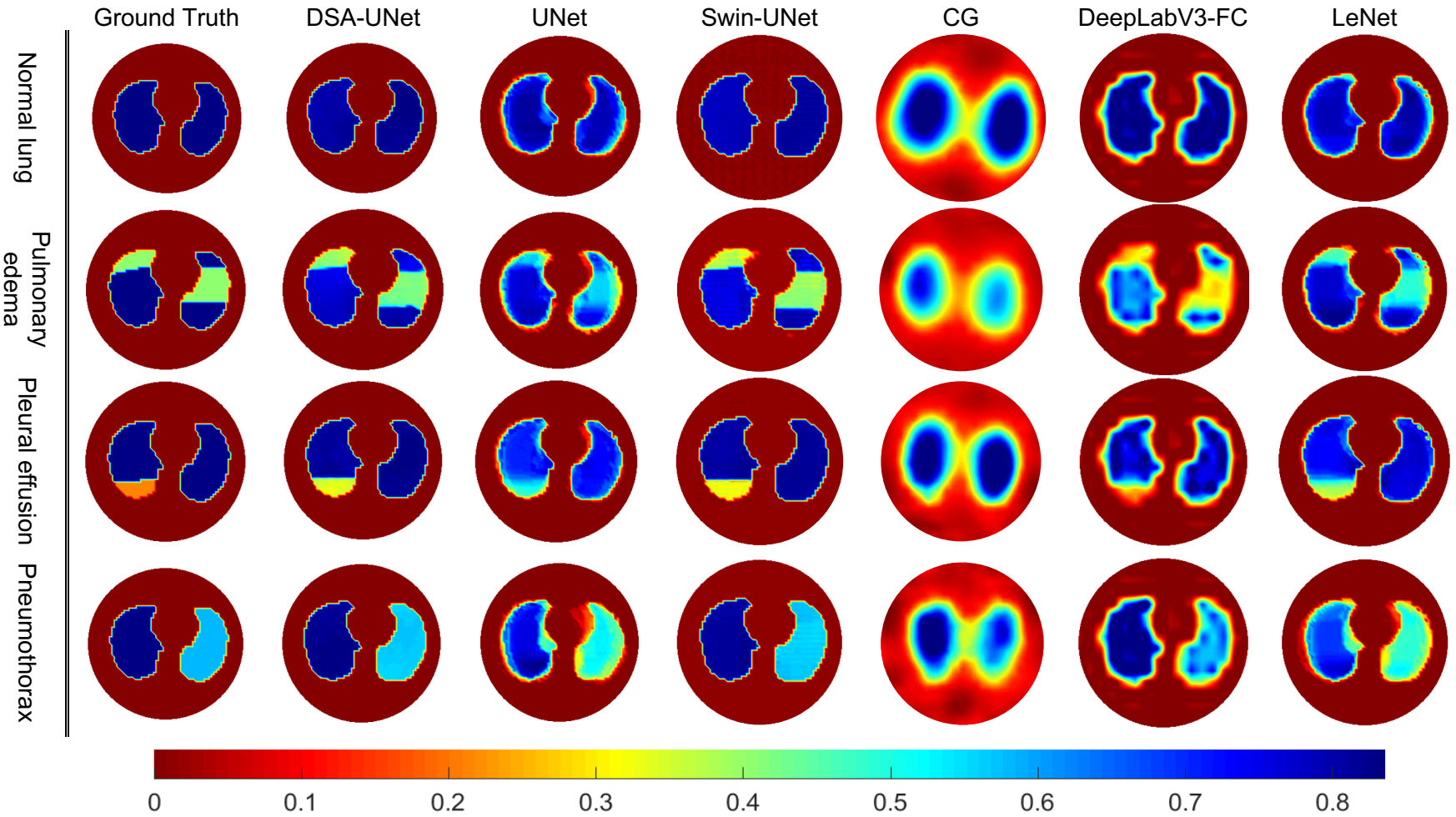

Figure 4-13: Image reconstruction results of the lung with different algorithm methods.

Table 4-4: The results of CC, RE and SSIM of the Figure 6-13 for different lung diseases.

	Ground Truth	Evaluation	DSA-UNet	UNet	Swin-UNet	CG	DeepLabV3-FC	LeNet
Normal lung	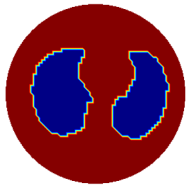	CC	0.9562	0.9252	0.9419	0.7301	0.9399	0.9136
		RE	0.2500	0.2950	0.2324	0.7865	0.2928	0.2704
		SSIM	0.9556	0.9180	0.9422	0.4979	0.9368	0.9236
Pulmonary edema	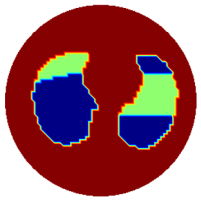	CC	0.9549	0.9170	0.9284	0.6805	0.9353	0.9052
		RE	0.2566	0.3359	0.2748	0.8233	0.3048	0.3136
		SSIM	0.9542	0.9096	0.9281	0.4236	0.9326	0.9023
Pleural effusion	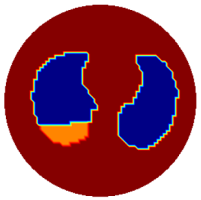	CC	0.9538	0.9278	0.9360	0.7168	0.9244	0.9142
		RE	0.2514	0.3299	0.2638	0.8147	0.3298	0.2878
		SSIM	0.9567	0.9163	0.9356	0.4395	0.9217	0.9121
Pneumothorax	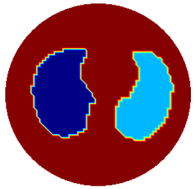	CC	0.9550	0.9228	0.9446	0.7141	0.9368	0.9172
		RE	0.2542	0.3002	0.2625	0.8196	0.2980	0.2935
		SSIM	0.9545	0.9072	0.9438	0.4791	0.9338	0.9035

Different lung diseases are designed with different levels of complexity in this section, and it is evident that pulmonary is the most complex type of segmentation in this chapter, as both left and right lungs are segmented into different regions, making imaging more difficult to reconstruct. However, according to the data in Table 4-5, it can be seen that the experimental results do not degrade performance due to the increased imaging difficulty, as the DSA-UNet model is proven to be more robust and can consistently output valuable reconstructed images.

Table 4-5: The comparison between different lung diseases based on DSA-UNet.

	Normal lung	Pulmonary	Pleural	Pneumothorax
CC	0.9562	0.9549	0.9538	0.9550
RE	0.2500	0.2566	0.2514	0.2542
SSIM	0.9556	0.9542	0.9567	0.9545

Figure 4-14 illustrates the performance of the RP-UNet for the lungs in different situations. Six different shapes of lungs are included in the figure as well as different segmented regions. The results show that the RP-UNet results do not differ much from the ground truth and have reproduced the true conductivity distribution as much as possible. Therefore, RP-UNet is considered to be useful for complex medical image segmentation, not only in terms of short inference times, but also to substantially improve the imaging results. Although some details are not yet fully restored, it is still the best choice among all models.

.

Ground truth	RP-UNet	Ground truth	RP-UNet	Ground truth	RP-UNet
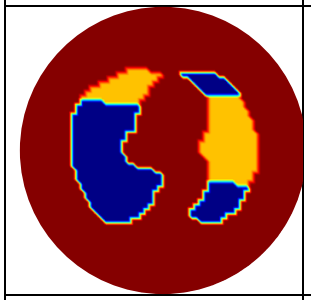	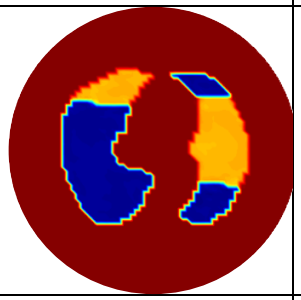	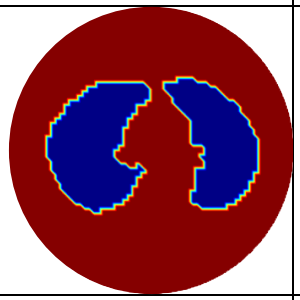	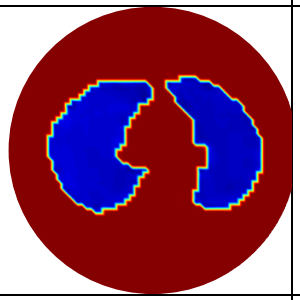	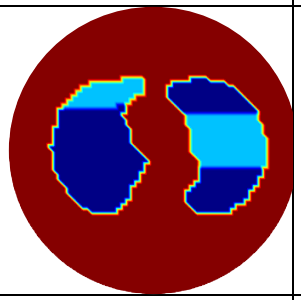	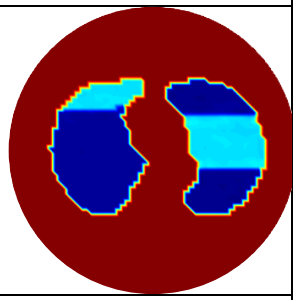
CC	0.9687	*CC*	0.9688	*CC*	0.9740
RE	0.1754	*RE*	0.2046	*RE*	0.2024
SSIM	0.9686	*SSIM*	0.9691	*SSIM*	0.9806
Ground truth	**RP-UNet**	**Ground truth**	**RP-UNet**	**Ground truth**	**RP-UNet**
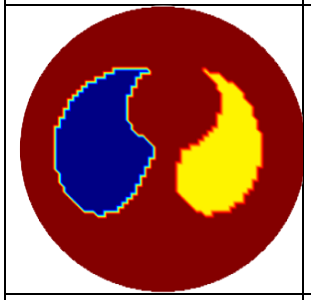	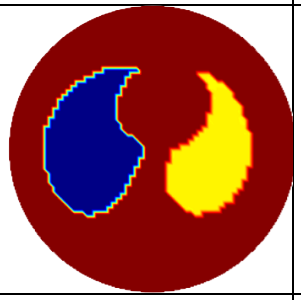	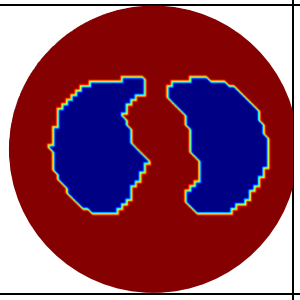	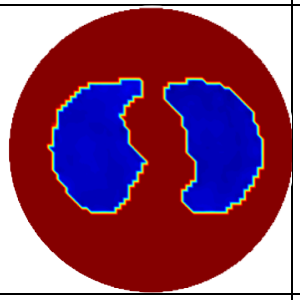	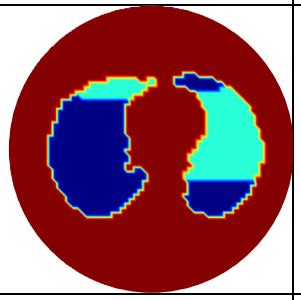	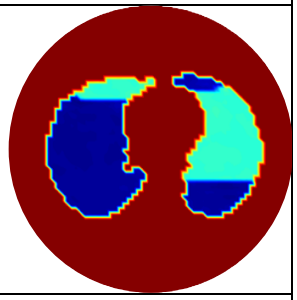
CC	0.9698	*CC*	0.9752	*CC*	0.9694
RE	0.1872	*RE*	0.1698	*RE*	0.2329
SSIM	0.9667	*SSIM*	0.9894	*SSIM*	0.9698
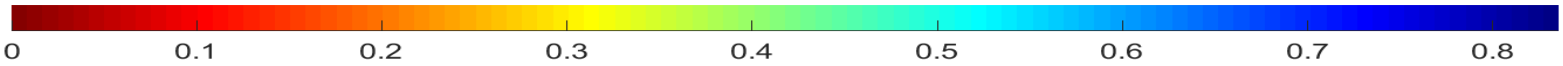					

Figure 4-14: The reconstructed imaging for RP-UNet with different lungs.

4.5 Ablation experiment

An ablation experiment is an experiment in which variables are controlled. When multiple modules or parameters are changed, the effect on the experimental results is verified by controlling the presence or absence of a single variable separately.

4.5.1 DSA-UNet

There are three added sections in the DSA-UNet model. Removing any one of them and testing the remaining part will show the effect of the removal term on the overall model, which is shown in Table 4-6.

When the DSC part is removed, the overall performance drops but the RE drops more. This proves that the DSC component is helpful in improving the performance of the model. However, without the SA or FC components, the performance of the model is much worse than when all of them are added. Thus, both the SA and FC components have a greater impact on the performance of DSA-UNet than DSC. It shows that all three can play their respective roles, but DSA is relatively weaker.

Table 4-6: The results of the ablation experiment based on DSA-UNet.

Network	CC	RE	SSIM
DSA-UNet	0.9592	0.2378	0.9416
w/o DSC	0.9527	0.2475	0.9379
w/o SA	0.9486	0.2614	0.9338
w/o FC	0.9487	0.2636	0.9309
Baseline	0.9216	0.3041	0.9117

4.5.2 RP-UNet

In the RP-UNet, there are only two new sections, but one additional assessment indicator, as shown in Table 4-7. As described in Section 4.2.2,

the main function of RepVGG is to speed up the inference time and to improve the performance of the structure as much as possible while ensuring that the inference time is not degraded. The table, therefore, includes an additional evaluation of the inference time.

Based on information in Table 4-7, it can be found that RepVGG has a significant impact on the inference time of the model, improving it by 0.0246 over the inference time of baseline. It sacrifices some inference time for greater accuracy and better performance compared to the full RP-UNet. When there is no RepVGG, the performance of the model drops even more, compared to no PSA. But in any case, both are beneficial to the performance improvement of the model, only RepVGG is more important.

Table 4-7: The results of the ablation experiment based on RP-UNet.

Network	CC	RE	SSIM	Time(s)
RP-UNet	0.9727	0.1800	0.9699	0.0201
w/o PSA	0.9684	0.1959	0.9650	0.0169
w/o RepVGG	0.9468	0.1761	0.9572	0.0224
Baseline	0.9216	0.3041	0.9117	0.1945

A visual demonstration of the performance of DSA-UNet, RP-UNet and baseline is shown in Figure 4-15. Based on the three evaluations, SSIM, CC and RE, RP-UNet as a whole performs the best, with optimal values for all indicators. Baseline, on the other hand, has the worst performance. Therefore, both innovative models are successful, and both can be useful for performance improvement.

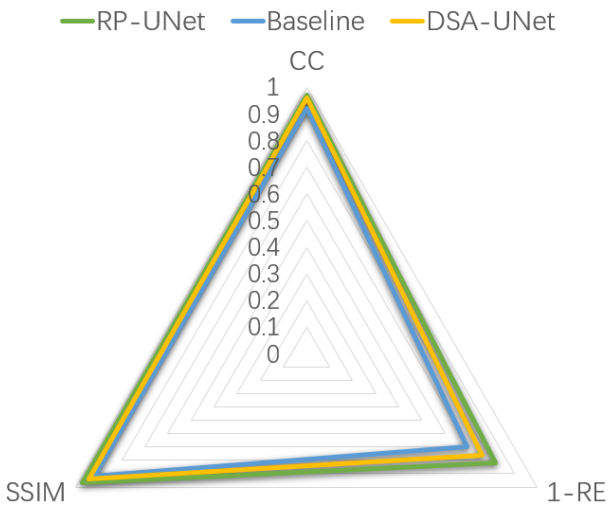

Figure 4-15: The performance of novel models and baseline.

4.6 Discussion

In this study, the focus is on two deep learning models. A comparison of eight image reconstruction algorithms and a qualitative and quantitative analysis shows that the new proposed models result in well-defined lung boundaries and a homogeneous internal conductivity distribution. The judgement of different types of lung disease can still be made in the presence of accompanying 40 dB noise, along with a high accuracy rate. While the performance analysis of the experimental results is important, ablation experiments are also essential. In the ablation experiments, each module is independently examined for its contribution to the performance of the network, and the blocks that have the greatest impact on the performance of the model are found. If some blocks are acting as side effects and affecting the performance of the model, then they can be replaced with more appropriate blocks in time.

UNet is a widely used model for medical imaging, and the parts added are well suited to the highly precision and complex medical image segmentation task, so that the innovative model exhibits high performance. However, it is worth noting that there are still many shortcomings. There is a certain scarcity of data

in this experiment, which was only obtained from 19 patient CT images through various deformations. Therefore, more CT images should be supplemented in subsequent experiments, as well as more segmentation of different lung regions. The improved database will allow for a more accurate analysis of the model's performance.

4.7 Summary

In this chapter, two different models are developed to improve the performance of UNet. Both novel models can handle complex image segmentation and reconstruction with high imaging quality. DSA-UNet is designed to improve inference speed by streamlining the parameters in the structure. Whereas RP-UNet aims to obtain more valid information by using a large number of parameters in the training process and to reduce inference time by simplifying the inference process. However, both models incorporate different attention, which makes the model more focused on useful information and improves the performance of the model. Based on the results shown, not only can we find a clear outline of the lungs, but we can also partition them precisely. Thus, we can calculate tidal volume changes from accurate EIT images. In addition, the reduction in inference time further facilitates the implementation of EIT-based control of the ventilator. Although not yet tested on human bodies, this chapter shows as many simulation results as possible. Only very simple phantom experiments have been verified, but there is too limited data to show them.

This chapter not only compares the results of deep learning and conventional algorithms discussed in Chapter 3, but also provides a deep foundation for Chapter 6. More importantly, the proposed model can perform perfectly in the field of lung imaging, as well as other medical imaging applications.

Chapter 5 Automatically adjusted ventilation control system based on ultrasound

5.1 Introduction

Mechanical ventilators have existed since at least the 14th century, however, it has been utilised widely in clinics until the late 19th century. Nowadays, mechanical ventilation is a core component of all hospitals, particularly the ICU. Ventilators were developed to monitor flow and pressure variables, and integrated these parameters to control ventilation patterns, with the development of electronic devices such as sensors [133]. In order to maintain proper gas exchange, ventilators exploit the pressure gradient between the atmosphere and the lungs [134]. By adjusting significant factors including tidal volume and respiratory rate, the mechanical ventilation focused on maintaining the optimal alveolar pressure range. A fixed tidal volume and a stable breathing rate are provided by the traditional mechanical ventilator. The lack of ability to monitor and record ventilation variables was a limitation of this version.

The negative consequences of ventilators were not recognized until the 1970s. Despite having the potential to save lives, misappropriation can result in consequences such VILI, which is reviewed in Chapter 2 [135]. Driving the pressure by controlling the tidal volume is a typical method. Lung injury can be resulted from the pressure caused by mechanical ventilation [42]. ARDS can be occurred by VILI, which would progress to multi-organ failure. Unacceptably high mortality rates are associated with ARDS [8]. Therefore, developing a precision ventilation strategy that protects the lungs is crucial. Due to its extremely high spatial resolution, CT has been crucial in monitoring the region of ventilation in earlier studies [65]. As a result, CT can detect localised pressures and alveolar hyperdistension that lead to VILI. Despite its benefits, CT still has significant limitations. Critically ill patients run a significant danger from radiation exposure and transportation to the CT room [136].

Contemporary ventilators are based on classical control theory, which can provide air flow to patient and obtain the feedback from monitor [42]. The experiments carried out for this research adopted a volume control strategy to develop an output-following system. As discussed in Chapter 3, reconstructed images of the EIT can be applied to determine the volume of lung. The output information of EIT is therefore anticipated to be involved in the closed loop to control variations of tidal volume, which is the focus of this thesis. In order to test the viability of the multi-sensor control strategy, this chapter will replace the EIT with an ultrasound sensor fused to the control system. The ultrasonic sensor will generate a feedback signal by detecting the change of liquid level caused by the increasing or decreasing of the volume in the lung. This is also to pave the way for the fusion of EIT with mechanical ventilation in Chapter 6, based on the control of tidal volume. Due to the non-linearity and unpredictability characteristics of the respiratory systems [134], intelligent control theories have also been applied to the system, such as dual-loop PID. The main objective of this chapter is to design and implement an appropriate control system for a laboratory ventilator model and to investigate the feasibility of a closed-loop system with volume feedback. As a result, the first fully closed-loop EIT-guided mechanical ventilation system can be introduced in the following chapter by integrating a dynamic EIT system with the volume control system.

5.2 Method

To simulate the ventilator control system, a simplified lung ventilator model was designed for the research.

According to Figure 5-1, the model is primarily made up of three parts: the hardware control component (an FPGA controller), the execution part (a

stepper motor and a syringe), and the feedback signal detection section (an ultrasound sensor).

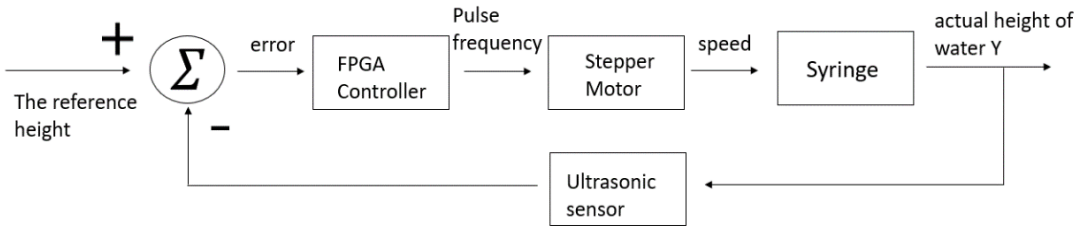

Figure 5-1: Block diagram of the control system.

5.2.1 Design a model for the control system with ultrasound

The object under control in this experiment is a balloon. The balloon inside the container is completely submerged in the water with an initial volume of 500 mL. The volume of the balloon can be adjusted by controlling the movement of the syringe, which in turn alters water height in the tank. On the FPGA board, the targeted reference water height is configured. The control signal is adjusted by the feedback signal from the ultrasound sensor. In essence, the reference signal and feedback signal are compared to generate an error signal, which is then used as an input signal of the controller. The signal produced by the controller, which is affected by the feedback of the sensor, is used to control the actuator, stepper motor. The final stage alters the height of the water in the tank by converting the volume of the syringe into the volume of the balloon in the water. The change of water height is detected by ultrasound, which serves as negative feedback, as well as the height of the water level is visible on the seven-segment display on the FPGA board.

The purpose of the control system is to ensure that the overall volume range of the balloon is not affected in any way, for example, if the patient breathes suddenly. It implies that the volume of the lungs remains within a constant range, approximating the ideal scenario for a patient's breathing. In the event of the routine breathing of patient is disturbed, the control system needs to

respond to the disturbance immediately and bring it back to a steady state as soon as possible.

The output of the ultrasound sensor initially reads 79 mm on the seven-segment display. The initial and final measurements of half cycle can be applied to calculate the peak-to-peak values of the curve. It is presumable that the typical respiratory curve based on tidal volume resembles a sinusoidal curve. The period of the aforementioned sinusoidal curve is 4 seconds while the typical respiratory cycle and rhythm of the human body are taken into account. Because the experiment uses the volume change of the balloon to approximate the volume change of the lung, the syringe's movement must follow a sinusoidal curve to guarantee that the balloon's volume change also follows sinusoidally when there is no disturbance to the system. However, in the event of a disturbance in the system, the syringe should automatically adjust its trajectory to ensure that the overall tidal volume is changing with a strictly sinusoidal wave. The system is disturbed if the other syringe triggers a change, in which case the control system must guarantee that the syringe's movement rapidly returns to an established sinusoidal curve. The spontaneous breathing of patients such as a sharp deep inspiration or a shift in spontaneous breathing intensity, may be the source of this disturb.

The FPGA board was set up via Verilog to carry out the aforementioned methodology, and the system was constructed using a laboratory model Basys 3 Artix-7 from Xilinx. The fundamental configuration of a simplified mechanical ventilator is illustrated in Figure 5-2. The ventilator is simulated using a stringer driven by a stepper motor fixed to the rails. The lung is simulated using a balloon submerged in water. The air that is delivered to the lung to facilitate breathing is the air in the syringe. The working process is shown below.

- When the system is reset, the starting point is on the right side of the syringe, meaning that the balloon's volume is at its minimum level.

- The motor driver, which is connected directly to the FPGA board, delivers a signal to the stepper motor to turn it on, squeeze the syringe and enlarge

the balloon.

- The change in water level is recognized by the ultrasound sensor. The stepper motor rotates in reverse once the FPGA board receives a signal from the ultrasound sensor whenever the maximum water level has been achieved. To reduce the volume of the balloon, the plunger is withdrawn from the syringe.

- The ultrasound sensor alerts the FPGA board once that the level of water reaches the minimum. The stepper motor rotates once again in the opposite direction and reciprocal action.

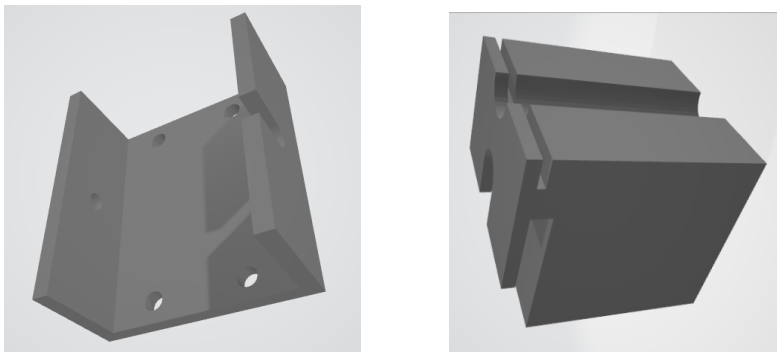

(a).

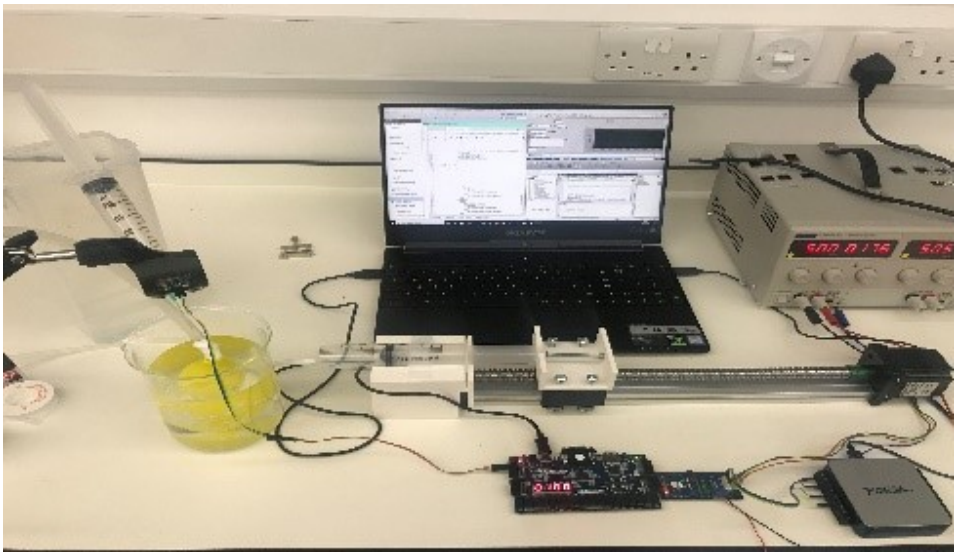

(b)

Figure 5-2: Experiment setup of the control system (a). Link parts between rail and syringe, which is also designed for holding the syringe. (b). The whole control system.

5.2.2 System design and implementation

The specific design details are presented in this section.

a) Execution system

Stepper motor and rail

A stepper motor is a brushless DC motor that converts electrical pulses into angular displacements. The rotor rotates by a fixed angle, known as the pitch angle, once a voltage pulse is supplied. The quantity of input pulses can be used to control the angular displacements and the position of the syringe.

This experiment uses a Nema 23 stepper motor with a maximum current of 3 A and a nominal voltage of 24 V. The rotor shaft is joined to a 300 mm guide rail, and each complete rotation cycle keeps moving on the rail by 5 mm. One complete cycle demands 200 pulses at a pitch angle of 1.8 degrees. Figure 5-3 shows the mechanical structure of the stepper motor with a linear guide rail.

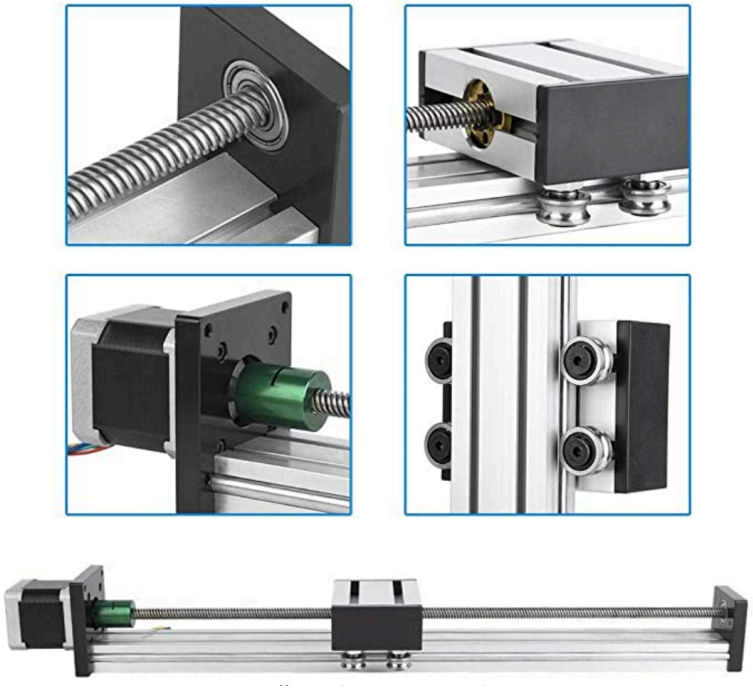

Figure 5-3: Stepper motor with linear guide rail.

Stepper motor driver

The Pmod stepper motor driver as shown in Figure 5-4 (a) is a default driver for the FPGA board. It can be directly linked to the Pmod port on FPGA board. However, it turns out that the driver can only supply up to 600 mA to the motor, which is a far less than 3 A. As a result, the speed of the stepper motor is consequently quite low and cannot meet the specifications. Therefore, in order to amplify the current and generate the pulse signal for the stepper motor, a new stepper motor driver is essential.

The high supply voltage of the Geckodrive G201X stepper motor driver as shown in Figure 5-4(b) ranges from 18V to 80V. The maximum phase current is 7 A. The maximum input stepping frequency is 300 kHz. In contrast to the Pmod driver, it is competent to drive high-power motors consistently.

(a) Pmod stepper motor driver

(b) Geckodrive G201X stepper motor driver

Figure 5-4: Stepper motor driver.

b) Feedback signal detection system based on ultrasound sensor

Ultrasound waves are processed by ultrasonic sensors to measure distance. The sensor sends out ultrasound waves and then calculates how long it will take for the waves to return from the target. The following formula can be applied to obtain the distance between the sensor and the target once the time has been determined.

$$D = \frac{v * t}{2} \tag{5.1}$$

where D stands for distance, v is the speed of ultrasonic waves at room temperature, and t means the time difference between emission and reception.

The Parallax PING ultrasonic sensor is demonstrated in Figure 5-5. It offers precise, non-contact measurements ranging from 2 cm to 3 m. The detailed signal transmission strategy will be discussed in the next Subsection 5.2.2.

Figure 5-5: Ultrasound sensor (Parallax PING).

c) Hardware control system on FPGA board

An FPGA is an integrated circuit that can be reconfigured by the user using a hardware description language, such as Verilog. It can be thought of as a control unit with hardware acceleration for different applications, etc. The primary benefits of using FPGAs in studies are their parallel execution and rapid processing speed.

For this project, a FPGA board called the Basys 3 was adopted. It includes three Pmod ports for input and output connections, along with a 100 MHz clock. In addition, it contains a 4-bit seven segment display, 5 push buttons, and 16 slide switches. The simplified ventilator control system can be implemented with these components.

Speed control and direction control

Careful control of the motion speed and direction for the stepper motors is essential during operation in this work. State machines are a valuable tool for Verilog to implement the process of control, as illustrated in Figure 5-6.

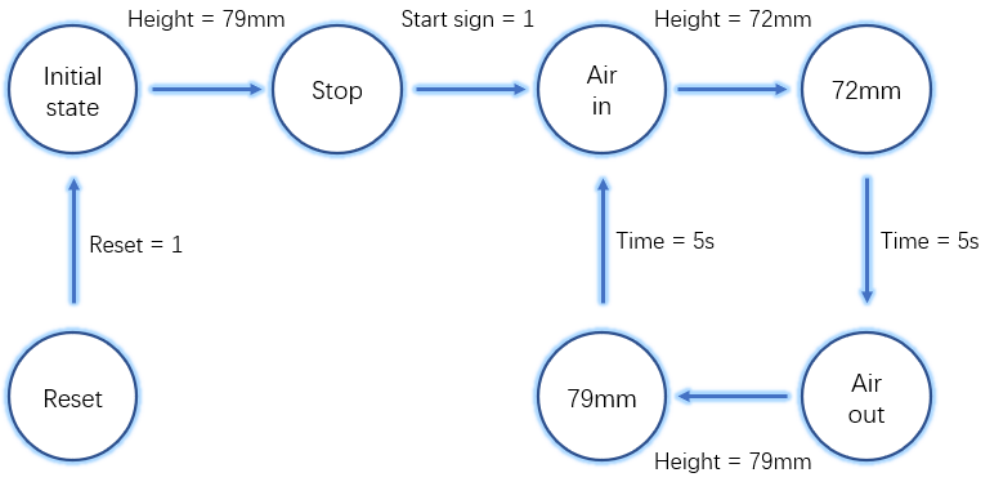

Figure 5-6: State machine diagram.

Any state will recover to the initialised state when the reset button has been pressed. The end of exhalation and the end of inhalation are added as two pauses to the threshold in order to more accurately replicate human breathing. The positive pressure at the end of inspiration is indicated by the pause at 72 mm. The pause at 79 mm state reflects the break in respiratory cycles. In typical human breathing, the pauses between respiratory cycles are so short that they only last for around 0.5 s at the end of the breath. Additionally, the conversion of discrete curves into continuous curves is easily achieved by such a breathing curve.

PID controller module

There are four primary factors to take into account when determining the task of the controller: stability, steady-state performance, transient responsiveness, and disturbance rejection [137]. Based on these criteria, an effective controller should be robust to any potential inputs or disturbances and enable the entire control system to reach the steady state with less overshoot and small steady-

state error. The robustness of the control system is particularly crucial because it is common for systems to be influenced by unanticipated events.

Due to its remarkable performance, PID controllers are frequently employed in the design and implementation of the control systems. PID controllers can control a variety of systems under different situations and are easy to develop. P, PI, PD, and PID controllers are the four main categories of controllers. The specification and control system contribute significantly to the controller selection. Alternatively, all of these can be implemented, and the corresponding responses compared to select the best response.

$$Time\ domain: u(t) = K_p e(t) + K_i \int_0^t e(t)\,dt + K_d \frac{de(t)}{dt} \tag{5.2}$$

$$Frequency\ domain: U(s) = \left(K_p + \frac{K_i}{s} + K_d s\right) E(s) \tag{5.3}$$

The performance of PID controller is not always sufficient. The value of K_p, K_i and K_d still need to be tuned and adjusted, because each value affects the output response differently.

The FPGA can only generate a discrete-time PID controller because it is a digital system. Here, a discrete controller should be developed by converting the continuous PID controller. This can be discretized and use the approach of summing for integration. Equation 5.4 can be approximated to Equation 5.5, where T_0 is the sampling interval and t is equal to kT_0. With respect to the derivative term, it is replaced by backward differencing. Equation 5.7 can be applied to approximate Equation 5.6.

$$K_i \int_0^t e(t)\,dt \tag{5.4}$$

$$K_i T_0 \sum_{i=1}^{k} e(i) \tag{5.5}$$

$$K_d \frac{de(t)}{dt} \tag{5.6}$$

$$K_d \frac{e(k) - e(k-1)}{T_0} \tag{5.7}$$

Then Equation 5.8 can be obtained, which is an absolute PID algorithm. The absolute value of the control signal will be the output of the algorithm. The incremental PID algorithm is a different discrete PID algorithm. The incremental value can be defined as Δu [13].

$$u(k) = K_p e(k) + K_i T_0 \sum_{i=1}^{k} e(i) + K_d \frac{e(k) - e(k-1)}{T_0} \tag{5.8}$$

$$\Delta u = u(k) - u(k-1) \tag{5.9}$$

$$\Delta u = K_p\big(e(k) - e(k-1)\big) + K_i T_0 e(k) + K_d \frac{e(k) - 2e(k-1) + e(k-2)}{T_0} \tag{5.10}$$

$$\Delta u = delay_0 * e(k) + delay_1 * e(k-1) + delay_2 * e(k-2) \tag{5.11}$$

where

$$delay_0 = K_p + K_i + K_d \tag{5.12}$$

$$delay_1 = -\big(K_p + 2K_d\big) \tag{5.13}$$

$$delay_2 = K_d \tag{5.14}$$

The incremental PID controller has a smaller register than the absolute PID algorithm since its output is just connected to the three previous states. The incremental algorithm is appropriate for controlling the stepper motor since stepper motor is controlled by an incremental signal.

According to the study above, there is a time-based relationship between $e(k), e(k-1)$ and $e(k-2)$, which are sampled at adjacent time. As a result, it can be implemented as follows in Verilog,

$$e(k-1) <= e(k);$$

$$e(k-2) <= e(k-1);$$

The Ziegler-Nichols method is a popular method of tuning a PID controller, which is apply to this control system. It very similar to trial and error method where K_I and K_D are set to zero, in the meanwhile, increase K_P until the loop has stable and consistent oscillation. Then according to control table of Ziegler-Nichols, K_P, K_I and K_D can be adjusted. After several experiments and adjustments, the most suitable set of PID parameters was obtained for $K_P = 0.125$, $K_I = 0.001$ and $K_D = 0.062$.

Stepper motor

The connection between the stepper motor driver and the FPGA board is illustrated in Figure 5-7. Based on internal instructions, the FPGA board would produce a step signal at the specified frequency. At the same time, the direction of rotation is controlled. The driver module, which is directly connected to the stepper motor, receives the step signal and direction signal. To generate signals for each port of the stepper motor, the stepper signals will be converted. Since this module is driven by a single coil, just one coil is active during each clock cycle. Figure 5-7 displays the waveform for a single coil.

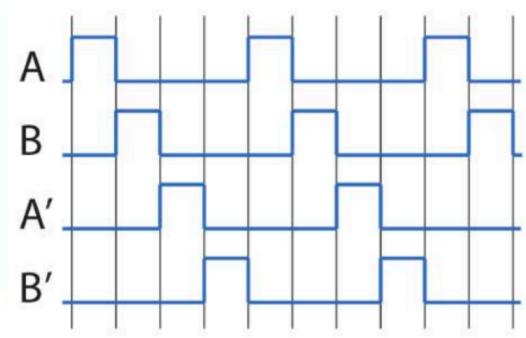

Figure 5-7: Single-coil excitation.

To evaluate the speed of the stepper motor and identify the relationship between the input command and step signal frequency, a separate module

has been designed, which is called *Test_Speed module* in the Figure 5-8 and Figure 5-9.

Syringe plunger movement length is 109 millimetres. The internal speed of FPGA board has a direct relationship with the speed of the stepper motor. The stepper motor will begin to move after a certain threshold has been obtained. Either the push-in or pull-out processes should be carried out to measure how long it takes the syringe plunger to travel that distance. The speed can then be determined by dividing the distance by the average travel time.

Theoretical speed can be obtained according to the equations below,

$$Theoretical\ speed = N * \frac{1}{200} * 5 \tag{5.15}$$

where N is the number of flips per second.

$$N = \frac{10^8}{n_c} * \frac{1}{10} * \frac{1}{2} \tag{5.16}$$

Where n_c stands for the number counted by counter.

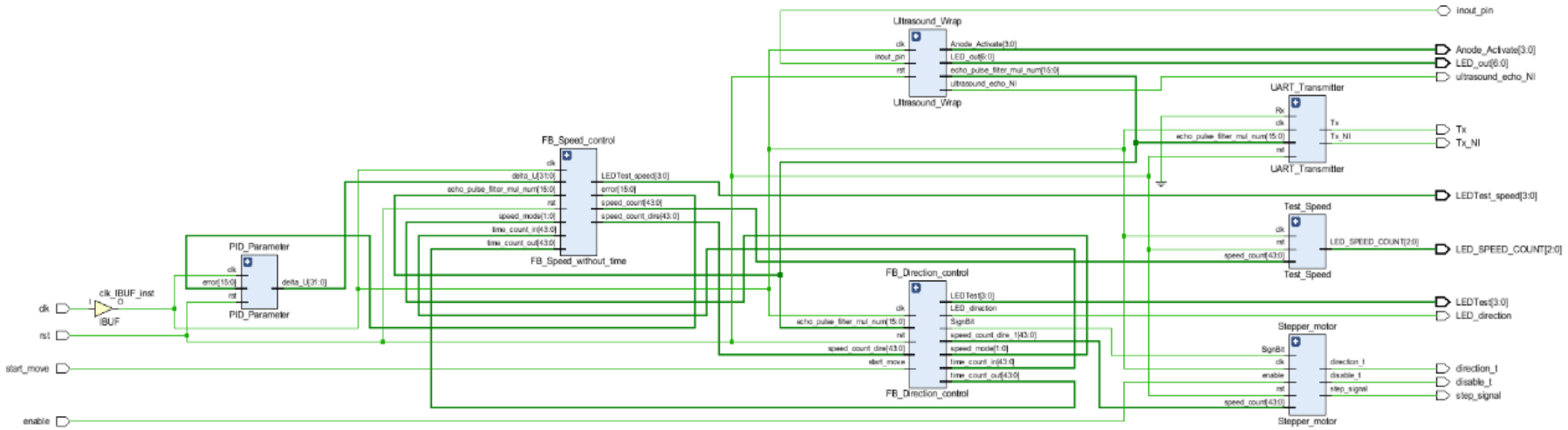

Figure 5-8: Structure of modules based on FPGA in Verilog (The detail in the blue block will be shown in Figure 5-9.).

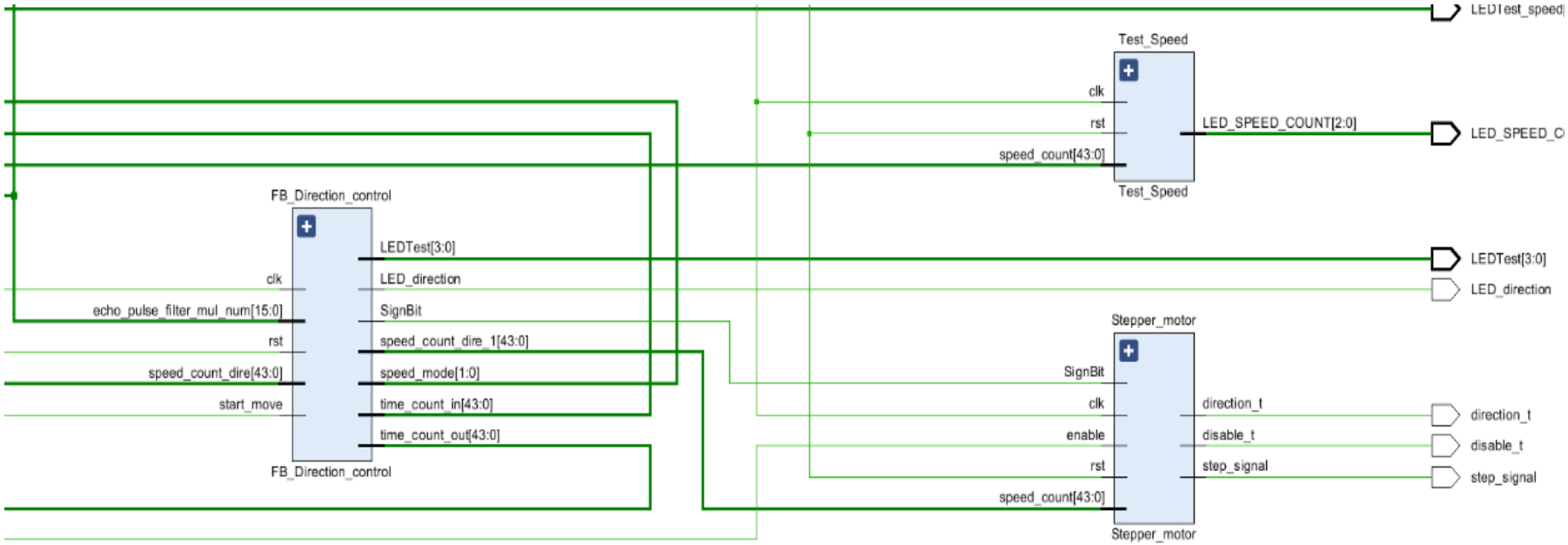

Figure 5-9: The structure of the stepper motor driver.

Ultrasound sensor module

The ultrasound sensor module has three pins [14]: GND, Vcc, and SIG, as shown in Figure 5-5. In addition, both input and output are implemented via the SIG pin, as shown in Figure 5-10. The basic operating principle of the ultrasound sensor is described in Section 2.2.2.

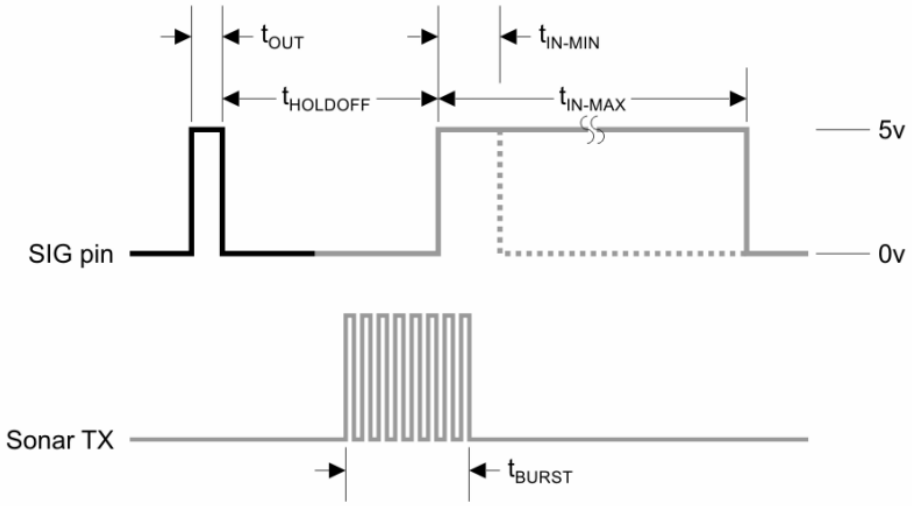

Figure 5-10: Working principle of ultrasound sensor [14].

The duration of the input trigger pulse (t_{out}) is 10 μm. The signal at the SIG pin is then inspected after that. The counter begins counting as soon as a rising edge is detected and ends when a falling edge is observed. The count is proportional to the time (t_{in}) utilised to compute the distance. To reduce the inaccuracy, which is calculated as the average of eight measurements, an averaging filter is used. The eight results are stored in eight registers and combined together in this block. Finally, the summation register is shifted three places to the right, which means divided by 8. The distance calculation is based on Equation 5.1. Verilog lacks direct multiplication and division, unlike software programming languages like C, C++, or Python. The Verilog IP core can be utilised for multiplication and register shifts can represent division by powers of two.

From the documentation,

$$C_{Air} = 331.5 + (0.6 * T_c) \tag{5.17}$$

where C_{Air} is speed of ultrasonic and T_c is room temperature in Celsius degree (by default, 25 Celsius degree). Hence,

$$C_{Air} = 346.5 \left(unit: \frac{m}{s}\right) \tag{5.18}$$

The unit of time is 10 ns. Assuming the counter number is t, then

$$D = \frac{10^{-8} * t * 346.5}{2} (unit: m) \tag{5.19}$$

where D represents distance between water surface to the ultrasound sensor. If unit of D is millimetre, and

$$D = \frac{0.0017325 * 2^{19} * t}{2^{19}} = \frac{908 * t}{2^{19}} \tag{5.20}$$

The division of 2^{19} is equal to right shift the distance register 19 bits in the digital system design.

Finally, the distance will be displayed in the seven-segment display. It can provide a visual indication of how the water level has changed. The whole implementation process of ultrasound sensor in Verilog is illustrated in Figure 5-11.

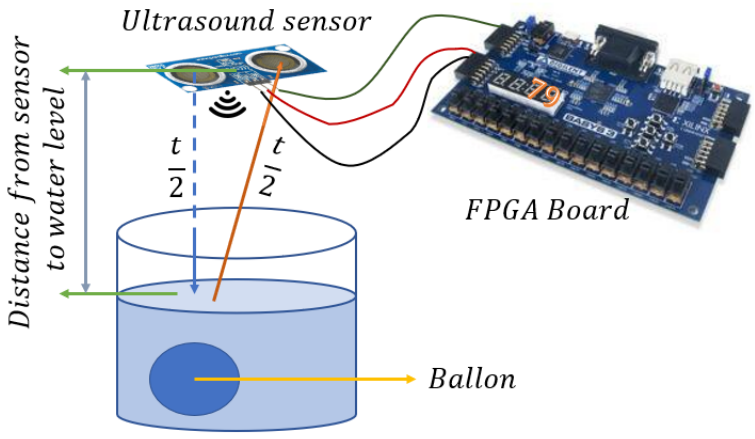

Figure 5-11: Ultrasound sensor implementation process.

d) Evaluation

To quantify the error between the output signal and reference signal, the mean squared error (MSE) and mean absolute error (MAE) can be defined as below,

$$MSE = \frac{1}{n}\sum_{i=1}^{n}(y(i) - x(i))^2 \tag{5.21}$$

$$MAE = \frac{1}{n}\sum_{i=1}^{n}|y(i) - x(i)| \tag{5.22}$$

where n is the sample number, as well as the $y(i)$ and $x(i)$ refer to output signal and input signal, respectively.

5.3 Results

5.3.1 Simulation results

The typical breathing rhythm is thought to be a sine wave curve, which is used in the simulation model. The blue line serves as a reference signal, while the red line represents the output response. This control strategy has a good following effect, as shown in Figure 5-12. The error analysis has been shown in Table 5-1. Furthermore, the output is relatively slow when the system is working without the PID controller, as shown in Figure 5-13, resulting in a delay of 25.22 ms.

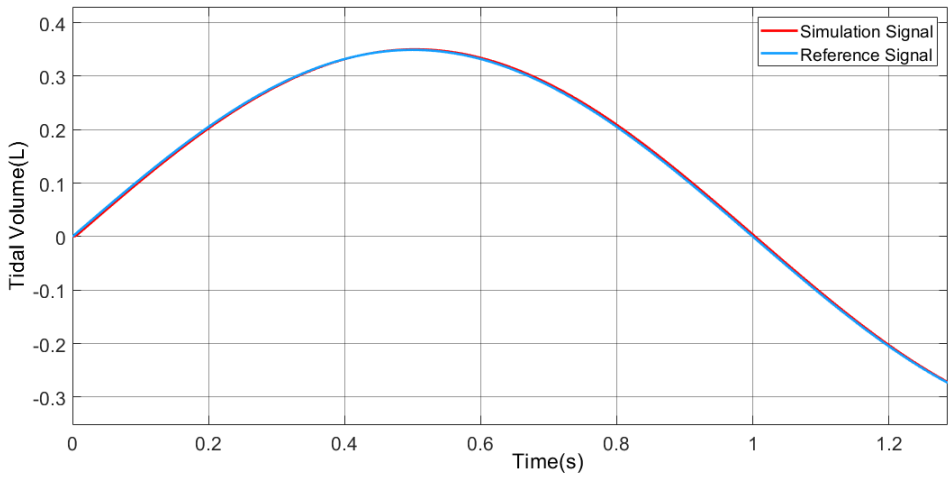

Figure 5-12: The results of the system with PID controller.

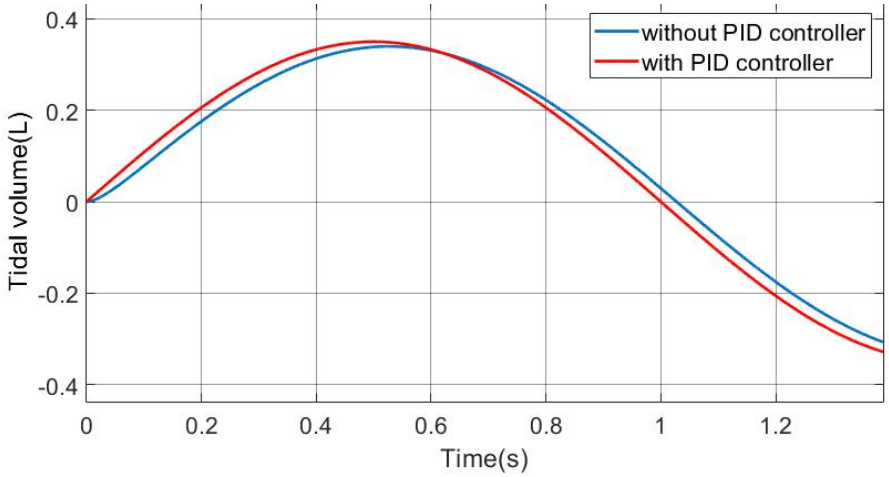

Figure 5-13: Results of the system without PID controller.

In most control systems, disturbance is common. It manifests in a number of reasons, including sensor noise, air friction, and distortion of non-linear components. Disturbing factors will lead to target deviations and distorted output responses. In control systems, disturbance suppression is essential. Adding feedback to the system, which mitigates undesirable impacts on the output response, is an excellent way to accomplish this aim.

The patient's ability to breathe on their own should be taken into consideration while developing a medical ventilator. However, it is unpredictable. It serves as a system disturbance in this work. The aim of the control system is to minimise the mismatch to a target value. A step input signal representing the disturbance is added to the system at a specific time in the simulation. The results of the simulation for different time and type disturbances are shown in the Figure 5-14 and Figure 5-15.

One of the basic requirements of a control system for PID is stability. After a system has been disturbed in equilibrium, within a period of time, the controlled quantity can reach a certain steady state, then it becomes stable state system. This can be confirmed by the fact that demonstrated in Figure 5-14 and 5-15. In addition, the PID system responds quickly to signals and quickly adjusts the system to a stable state. The effects of disturbances are eliminated.

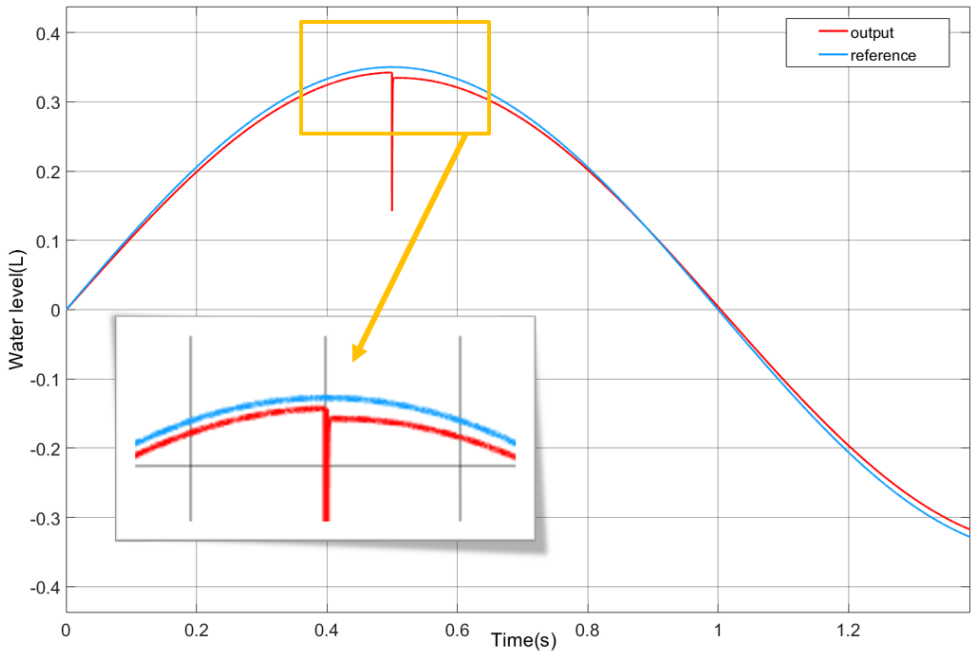

Figure 5-14: Sudden disturbance to the system (air out).

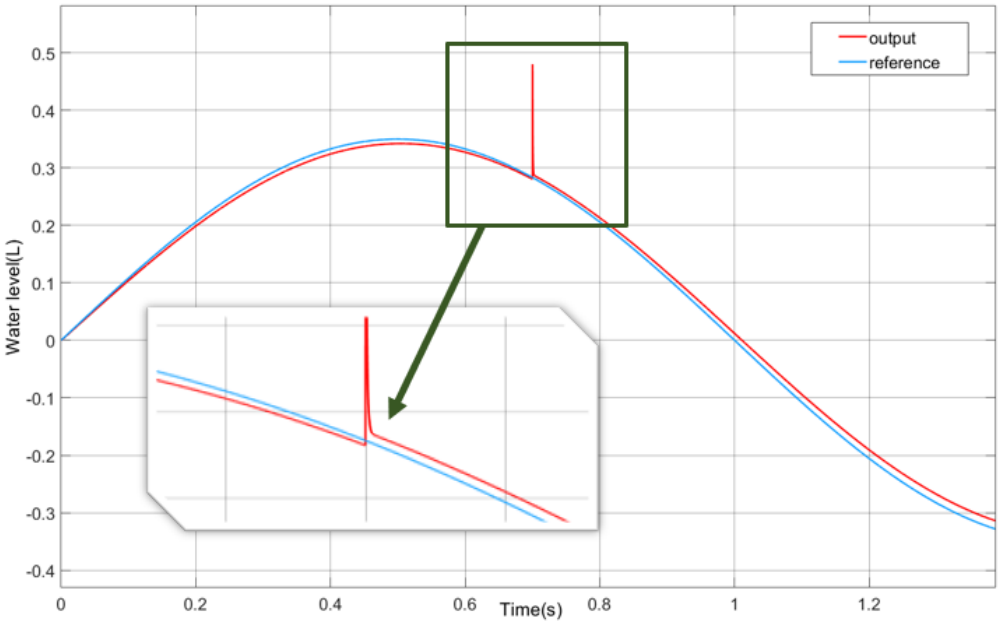

Figure 5-15: Sudden disturbance to the system (air in).

The control of the system with the PID controller is clearly superior to that without the PID controller, as evidenced by the error analysis in Table 5-1. Additionally, it may be considered as that the system is more robust and stable.

The system would react to disturbances relatively rapidly and return to a steady state.

Table 5-1: Evaluation of the errors.

	With PID	Without PID	Disturbance in	Disturbance out
Mean Squared Error (MSE)	0.9911	2.7734	0.9999	1.0104
Mean Absolute Error (MAE)	0.0070	0.0475	0.0091	0.0074

5.3.2 Experimental results

The experimental equipment is connected as shown in Figure 5-16. In the figure, (a) denotes the end of expiratory state, which is also the finished initialization state. (b) stands for the end of inspiratory state. Reciprocating motion can be carried out between expiratory and inspiratory. A comparison of (a) and (b) in Figure 5-16 shows that the balloon was growing bigger in the state of inspiration, resulting in a slight change. Because the tidal volume is small compared to the redundancy, it is difficult to observe. Therefore a more straightforward way has been chosen, which is to measure the height of the water level. The water level increased by 7 cm, from 79 cm to 72 cm, which is a noticeable change for the height of the water surface caused by insignificant change. In the meanwhile, the real time height data from the ultrasound sensor can be transmitted to the computer via Universal Asynchronous Receiver/Transmitter (UART). Once the data collection completes, information will be analysed.

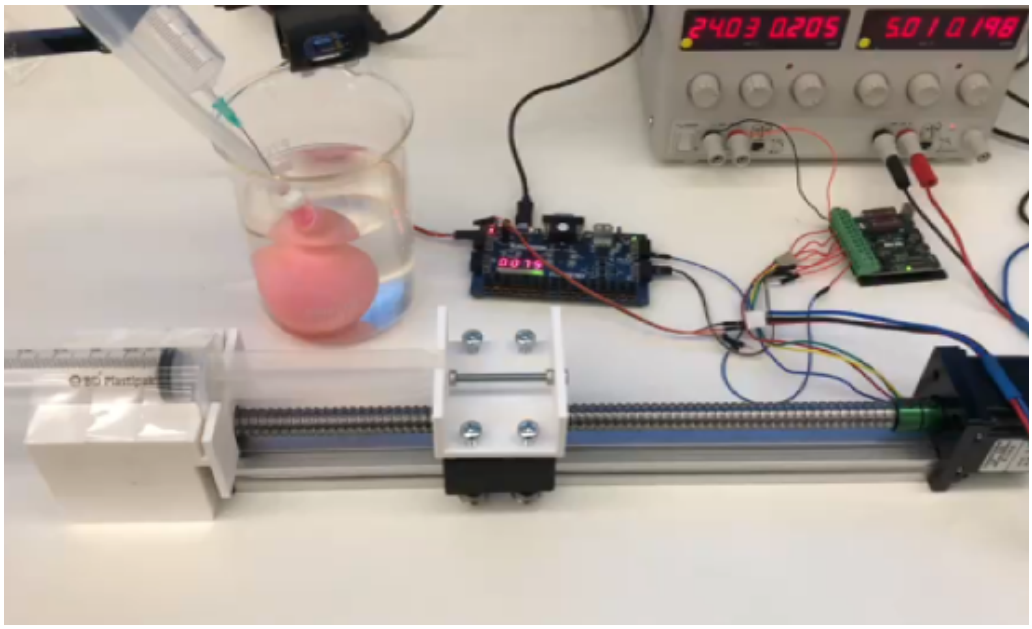

(a) End-expiratory state

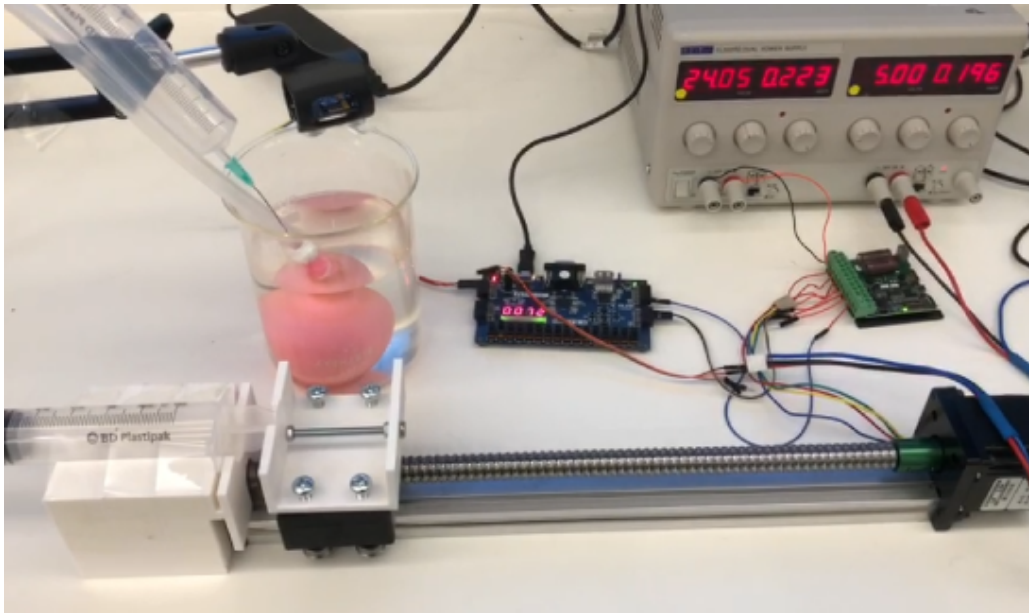

(b) End-inspiratory state

Figure 5-16: Experimental setup and different state of respiration.

The black dashed line in Figure 5-17 symbolizes the output of the seven-segment display, which can only produce a step signal due to the restrictions of the precision. The fitting curve of the output is shown by the solid blue line. It produces a smoother curve and a closer approximation to the breathing curve by fitting the discrete data to a sinusoidal waveform.

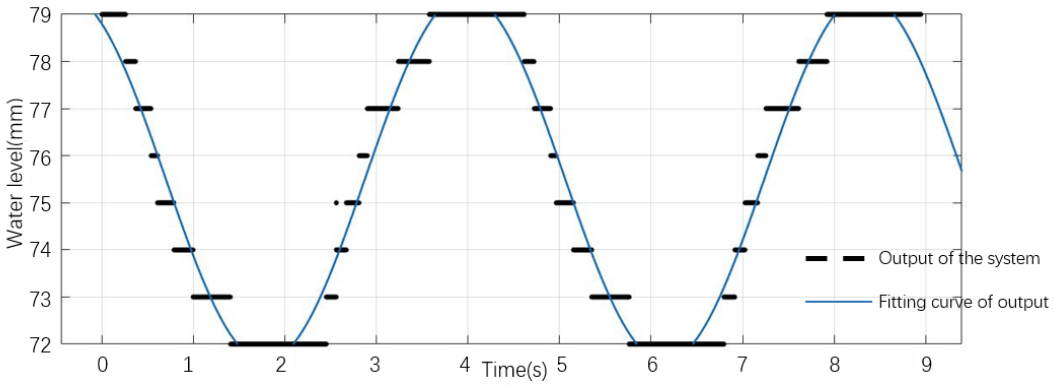

Figure 5-17: Fitted curve of water level.

The hardware control system additionally integrates a PID controller. The performance comparison between a system with and without a PID controller is demonstrated in Figure 5-18. The blue curve indicates a system without a PID controller, whereas the amber curve represents a system with a PID controller. The PID controller responds quickly and achieves steady state in a short period of time. System delay of 0.21 s is the result of the absence of PID, which is much large than that results in simulation.

Lagging occurs because proportional control increases the response speed by means of the gain K_p. Usually there is no hysteresis in proportional control. When derivative control is added, the system can react to the changing trend of the input signal with predictability. An effective early correction signal can therefore be introduced into the system to increase the degree of damping. This also explains why the response of a system without the PID controller lags behind that of one with it. However, the experimental response is much worse than the simulation results, mainly because there are many systematic and random errors in the experiments, which make the signals less accurate. For example, when water level is measured by the ultrasound sensor, water level changes as the volume change of the balloon. Additional water surface random movement is amplified. On the other hand, mechanical systems introduce unavoidable errors during operation due to frictional resistance, for example. Therefore, the response in the experiment is therefore slightly worse.

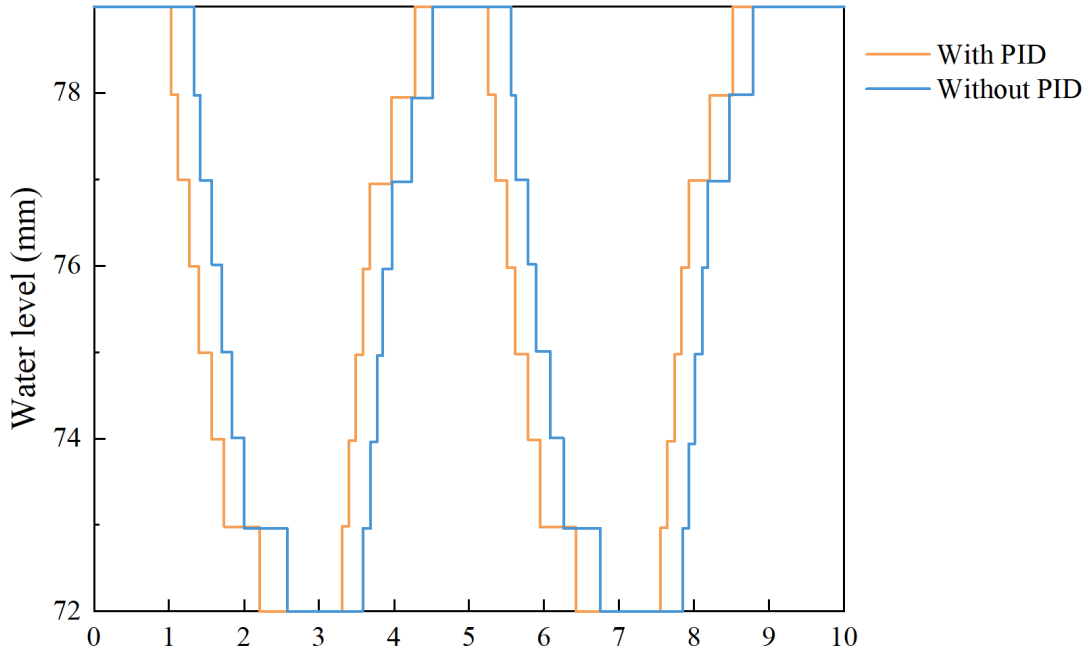

Figure 5-18: Time response of controller with/without PID.

5.4 Discussion

In clinics, ventilators are a crucial component of medical equipment. VILI was first recognised in the 1970s. To lessen the impact of VILI, many pulmonary protection measures were recommended, including the use of CT to analyze images of the lungs. EIT-guided ventilators can work at the bedside for longer periods of time than traditional ventilators, which can detect changes in the lungs in real-time. Additionally, compared to a conventional ventilator, the changes in variables that can be obtained with an EIT-based ventilator. It can offer multiple dimensional information. The enhanced ventilator might lower patient fatalities caused by VILI and even ARDS. Work in this chapter paved a foundation for EIT-guided ventilators, which provides a PID framework for the ventilator control system. Once lung tidal volume is obtained by EIT in real-time, this information will replace water level from the ultrasound sensor. It is expected the whole control system will continue to work with minimal

adjustment. For researchers attempting to comprehend the fundamental operation of a ventilator, work presented in this chapter can be a useful starting point. On the basis of this, more options are presented for upgrading the ventilator further to a smarter model. Few human interactions are required in the future because the ventilator will choose the appropriate tidal volume and breathing rate based on the patient's age, weight, and other factors.

5.5 Summary

In this chapter, the project aims to design and implement a control system for the ventilator that explores the feasibility of a volume control strategy with ultrasound sensor. In specifically, the study of this chapter describes the design and implementation of the model. In addition, the discrepancy between simulation and experiment is compared. Moreover, the error analysis of the control system in the experiment had been carried on. The experimental results demonstrate that the designed system is capable of achieving the goals and requirements. As a result, the integration of EIT with mechanical ventilation will be discussed in the following chapter.

Chapter 6 Ventilator control system guided by electrical impedance tomography

6.1 Introduction

As an important medical device, mechanical ventilation can improve respiratory function and reduce respiratory exertion in patients who are physically unable to breathe [138], such as ARDS [139]. However, conventional ventilators may lead to VILI, as described in Smith's work [140] Local pressure in the lungs may result in uneven gas distribution within the lungs. Therefore, real-time imaging of the lungs to detect inhomogeneous gas distribution is essential.

As a unique imaging modality, EIT can provide both 2D and 3D lung imaging to offer medical information without any side effects to the body. Therefore, using the medical information provided by EIT to guide the mechanical ventilation system can be effective in reducing VILI. A similar concept was proposed by Tregidgo [42]. The work of Tregidgo was designed to demonstrate that EIT and lung function models could be coupled to retrieve variables and assist mechanical ventilation adjustment. However, EIT is primarily used as a monitoring instrument to measure changes in lung volume over time, rather than providing an automated guide to ventilator flow rates. To evaluate the impact of MIE, the viability of employing 3D EIT images to estimate lung volumes before and after MIE was explored [53]. The EIT could detect lung hyperinflation and misaspiration during respiratory support in patients who were under anaesthesia or in the ICU [54]. Therefore, incorporating information from EIT to control mechanical ventilation is necessary to avoid further lung damage. Becher analyzed the influence of an EIT-based protocol on respiratory compliance, oxygenation, and alveolar circulation as well as discover whether it could customise ventilator settings without introducing too much pressure on the lungs [51]. The ability of the EIT

device to measure relative tidal volume and relative stroke volume concurrently, non-invasively, and in real time was conclusively achieved in Jang's work [141].

In the Chapter 5, information conveyed by ultrasound was one-dimensional and could only be used to determine whether the water level was at the reference height and thus infer whether the tidal volume inside the balloon was achieved as expected. EIT can be used to provide image information in 2D and 3D. Thus, it is possible to determine whether the air volume inside the lung is at the expected value, whether there is damage inside the lung, and even the location, size and extent of that damage. Of course, there are many imaging modalities that can also provide image information, but the non-radiation, non-invasive, real-time nature of EIT further extends its advantages. Ordinary EIT imaging suffers from low resolution. However, in Chapters 3 and 4, we have optimised the existing image reconstruction algorithms by means of conventional algorithms and deep learning algorithms, which also contributes significantly to the implementation of this chapter. Therefore, in this chapter, the image reconstruction algorithm of the EIT is no longer the focus, but how to utilise the image information from the EIT is our main concern.

In order to improve the intelligence of the ventilator and to take advantage of the EIT as much as possible, this study designs mechanical ventilation guided by the EIT. A closed-loop ventilator control system is implemented using the reconstructed images of the EIT as feedback loop. In addition, EIT images can provide additional valuable information such as localised lung expansion or atelectasis. Based on the EIT reconstructed the cross-sectional lung images, the tidal volume during respiration is estimated, and a relationship between the conductivity of the lung and the tidal volume is derived. Based on this model, an EIT-based mechanical ventilation system is developed. For the first time, EIT is used as a feedback signal for long-term real-time control of tidal volume changes, combining a joint simulation method with COMSOL, MATLAB and SIMULINK. Experiments are carried out with different lung models and breathing conditions to verify the performance of the control system.

6.2 Method

The structure of the closed-loop control system with a respiratory system designed in this chapter is shown as below in Figure 6-1, which consists of controller, actuator and feedback sensor. However, unlike in Chapter 5, the feedback sensor has been replaced with an EIT system. It was verified that a closed-loop control system via a volume control strategy could be implemented in the last chapter. Therefore, the thoughtful approach of volume control is continued to complete the closed-loop control system with EIT images as feedback in this chapter. The three components are described in detail below.

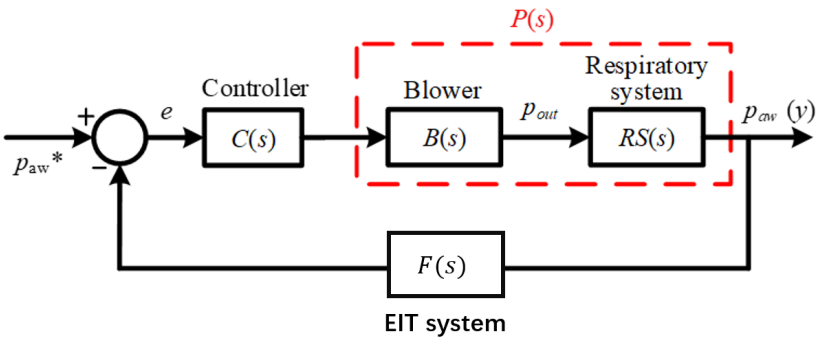

Figure 6-1: Closed-loop control system with a respiratory system.

6.2.1 Estimation of the lung volume

Based on the algorithms for reconstructing images in Chapters 3 and Chapter 4, the images of the lungs can be rendered relatively accurately. Therefore, the volume of the lung will be estimated, based on the results of the reconstructed lung images. Since the reconstructed result is composed of 64×64 pixels, a grid will be drawn over the image, as shown in Figure 6-2. It is worth noting that the meshing for reconstructing the image is also 64×64, while (a) in the figure is only a schematic. The Figure 6-2 (b) is enlarged with the details of Figure 6-2 (a) to make it easier to understand the 1×1 pixel points.

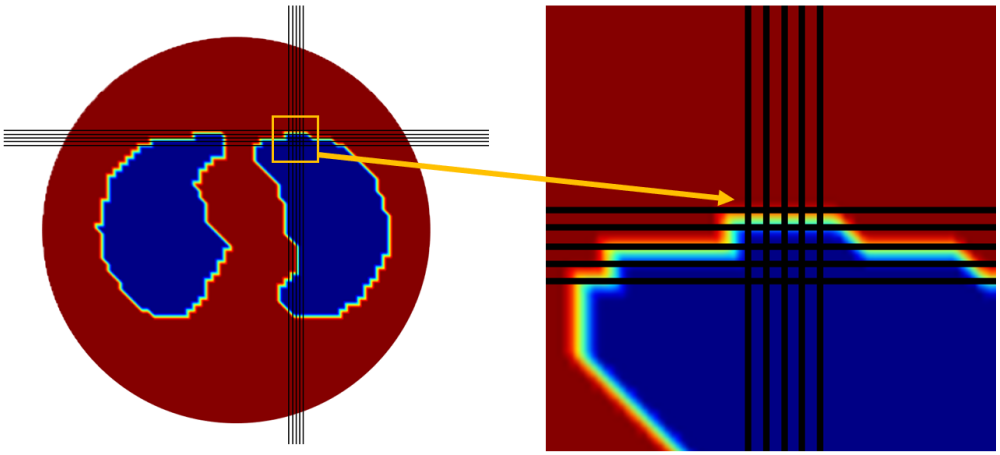

(a) (b)

Figure 6-2: Meshing the reconstruction images for counting the area of valid lung.

After the reconstructed image has been divided into 64×64 pixels, the threshold τ can be decided according to Equation 6.1.

$$\tau = \frac{\sigma_{max} - \sigma_{min}}{2} \tag{6.1}$$

where σ_{max} is the maximum conductivity of the reconstructed image and σ_{min} stands for the minimum conductivity of the result.

Therefore, the valid lung area is all pixels with a value less than the threshold, due to the conductivity of the thorax is greater than the conductivity of the lung. To simplify the lung model, the lung is considered to be an irregular column, so that the volume of the lung is,

$$V_{lung} = A_{lung} \times h_{lung} \tag{6.2}$$

$$= N_{pixel} \times \sigma_{ave} \times h_{lung} \tag{6.3}$$

where V_{lung} is the estimated volume of lung, A_{lung} represents the estimated valid area of the cross-section of the lung. N_{pixel} means the total number of the valid pixel according to the threshold. As for the σ_{ave} is the average conductivity of the valid pixel, and the h_{lung} stands for the height of the lung.

6.2.2 Control system

In this chapter, a linear active disturbance rejection control (LADRC) strategy has been used, which is proposed by Gao [142], to improve the speed and the robust of the system. Therefore, the anti-disturbance ability shows an excellent performance when the respiratory is disturbed. The LADRC contains two important blocks, linear state error feedback control (LSEF) and linear extended state observer (LESO), as shown in the Figure 6-3.

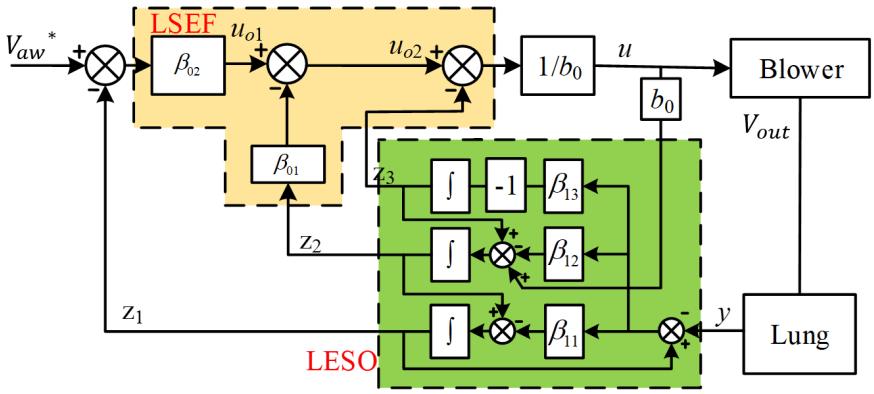

Figure 6-3: Structure diagram of LADRC.

The system can be affected by disturbances occurred by the spontaneous breathing of patient and by air leaks of the system. Therefore, the control strategy can be adjusted by estimating the disturbances in the system in order to ensure that the respiratory function works properly.

The output u of LSEF can be defined as,

$$u_{o2}(t) = u_{o1}(t) - \beta_{01} z_2(t) \tag{6.4}$$

$$u_{o1}(t) = V_{aw}{}^* - \beta_{02} z_1(t) \tag{6.5}$$

$$\beta_{01} = 2\omega_c \tag{6.6}$$

$$\beta_{02} = \omega_c^2 \tag{6.7}$$

where u_{o2} and u_{o1} are the outputs of the LSEF, the output of lung y will product the z_1, z_2 and z_3. ${V_{aw}}^*$ represents the reference signal, which is the desired volume.ω_c is the bandwidth of the controller.

The LESO block is used to estimate the disturbance, which is shown in the below,

$$u(t) = \frac{u_{o2}(t) - z_3(t)}{b_0} \tag{6.8}$$

$$\ddot{y}(t) = f(t) - z_3(t) + u_{o2}(t) \tag{6.9}$$

where b_0 is the control gain of the system, $f(t)$ is the disturbance to the system.

6.2.3 Mathematical model of respiratory system

In this chapter, the respiratory system consists of the blower, the connecting hose and the lung, which is shown in Figure 6-4. The relationship between tidal volume V and the inspiratory flow Q is,

$$Q(t) = \frac{dV(t)}{dt} \tag{6.10}$$

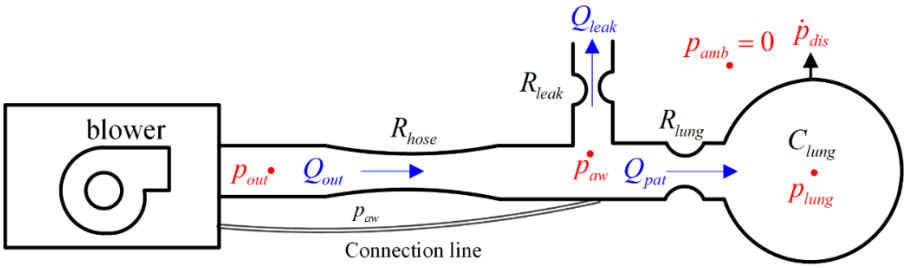

Figure 6-4: Structure of a respiratory system.

The blower compresses the air according to the signal from the front control system, so that at the position of the blower outlet Q_{out}. After Q_{out} passes through the connection line, part of the airflow is leaked, so that the airflow into the lungs is Q_{pat}, as shown in Equation 6.11.

$$Q_{pat} = Q_{out} - Q_{leak} \tag{6.11}$$

where Q_{pat} is the airflow delivered to the lung. Q_{out} represents the airflow out from the blower. As for the Q_{leak} is the part leaked from connection hose.

The relationship between pressure and airflow is,

$$Q_{\text{out}} = \frac{p_{\text{out}} - p_{\text{aw}}}{R_{\text{hose}}} \tag{6.12}$$

where p_{out} is the output pressure of the blower, the p_{aw} is the airway pressure in the hose, and the R_{hose} is the resistance of hose.

$$Q_{\text{leak}} = \frac{p_{\text{aw}}}{R_{\text{leak}}} \tag{6.13}$$

where R_{hose} is the resistance of leaking.

$$Q_{\text{pat}} = \frac{p_{\text{aw}} - p_{\text{lung}}}{R_{\text{lung}}} \tag{6.14}$$

where p_{lung} represents the pressure in the lung, and R_{lung} stands for the resistance before the inspiratory flow get into the lung.

From the above equation it can be derived that,

$$p_{\text{aw}} = \frac{R_{leak} R_{\text{hose}}\, p_{\text{lung}} + R_{\text{lung}}\, R_{leak} p_{\text{out}}}{R_{leak} R_{\text{hose}} + R_{leak} R_{\text{lung}} + R_{\text{hose}}\, R_{\text{lung}}} \tag{6.15}$$

$$\dot{p}_{\text{lung}} = \frac{p_{\text{aw}} - p_{\text{lung}}}{C_{\text{lung}}\, R_{\text{lung}}} + \dot{p}_{\text{dis}} \tag{6.16}$$

Then,

$$\dot{p}_{\text{lung}} = \frac{(Q_{out} - Q_{leak}) R_{\text{lung}}}{C_{\text{lung}}\, R_{\text{lung}}} + \dot{p}_{\text{dis}} \tag{6.17}$$

$$\dot{p}_{\text{lung}} = \frac{-(R_{\text{leak}} + R_{\text{hose}}) p_{\text{lung}} + R_{\text{leak}}\, p_{\text{out}}}{R_{\text{lung}}\, C_{\text{lung}}\, R_{\text{hose}}\, R_{\text{leak}}\, R} + \dot{p}_{\text{dis}} \tag{6.18}$$

where $R = (R_{lung}R_{hose} + R_{lung}R_{leak} + R_{hose}R_{leak})/(R_{lung}R_{leak}R_{hose})$

Depending on the relationship between the obtained pressure and tidal volume, the simulation of the lung can be controlled by adjusting the lung resistance and lung compliance. In addition, the parameters had been set as the Table 6-1.

Table 6-1: Parameters of single lung model.

Parameters	Value	Unit
$\boldsymbol{C_{\text{lung}}}$	20	$mL/mbar$
$\boldsymbol{R_{\text{lung}}}$	5	$mbar/L/s$
$\boldsymbol{R_{\text{hose}}}$	10	$mbar/L/s$
$\boldsymbol{R_{\text{leak}}}$	55	$mbar/L/s$

Expansion of a single lung to multiple lungs are present, according to the work of Henry [42] , it is possible to model multiple lungs as having two lungs on the left and right, and each lung containing two lobes, as shown in Figure 6-5. Thus, the compliance and resistance values of the whole lung are,

$$\boldsymbol{C} = \begin{bmatrix} C_1 & 0 & 0 & 0 \\ 0 & C_2 & 0 & 0 \\ 0 & 0 & C_3 & 0 \\ 0 & 0 & 0 & C_4 \end{bmatrix} \tag{6.19}$$

$$\boldsymbol{R} = \begin{bmatrix} R_0 + R_1 & R_0 & R_0 & R_0 \\ R_0 & R_0 + R_2 & R_0 & R_0 \\ R_0 & R_0 & R_0 + R_3 & R_0 \\ R_0 & R_0 & R_0 & R_0 + R_4 \end{bmatrix} \tag{6.20}$$

where R_0 is the residence of the hose before the airflow get into four lungs.

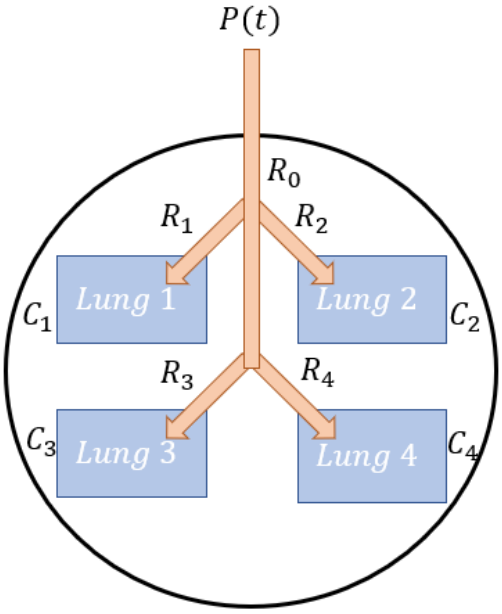

Figure 6-5: Multi-lung model for two lobes each in the left and right lung.

Moreover, the parameters for each lung of the multi-lung model are represented in Table 6-2. In order to simulate the effects of different lungs, different parameters have been set.

Table 6-2: Parameters of multi-lung model.

Compartment	C ($mL/mbar$)	R ($mbar/L/s$)
Lung1	10	*10*
Lung2	10	*20*
Lung3	15	*5*
Lung4	25	*10*

6.2.4 Lung cases

In this section, four different respiratory situations are considered: the adult respiratory state, the disturbed state, the gradual state, and the neonatal respiratory state. The tidal volume is the parameter to be focused on.

a) The adult respiratory state

Case 1 describes a situation when the patient has no spontaneous breathing, where the ventilator needs to output the breathing curve of a normal adult, including intensity and frequency. The simplified breathing curve is a sinusoidal curve based function with a period of 4 s, with an average of 15 breaths per minute. The average tidal volume is 500 mL, which is also the amplitude of the respiratory curve.

b) The disturbed state

Case 2 describes a situation when a sudden change in the breathing process occurs. This disturbance may be influenced by the spontaneous breathing of patient, such as a sudden deep inspiration, or it may be due to the effect of a leak. Therefore, the situation simulated in this section is one in which the patient has part of spontaneous breathing but cannot maintain the vital needs. Then, at some point, there may be a sudden pause in breathing or a deep inhalation that affects the original breathing. Consequently, the cooperative work of a ventilator is required. For example, a deep inhalation results in a sudden increase in lung volume. As a result, the conductivity of the lungs also changes and is fed back through the images of the EIT. At the same time, the ventilator needs to react quickly to this sudden change so that the tidal volume of patient can be quickly recovered to normal values.

c) The gradual state

During general anaesthesia, it is necessary to keep the total respiratory curve of patient in line with that of a normal adult. As the spontaneous breathing of patient gradually decreases until it is fully supported by the ventilator, the ventilator needs to provide a respiratory curve of varying intensity. After ten seconds the respiratory curve reaches a steady state, with the same frequency and amplitude as in case 1. The process of recovery is the opposite of that of general anaesthesia. However, during this process, the sum of the patient's

breathing and the amount provided by the ventilator needs to be maintained to match the ideal adult respiratory curve.

d) The neonatal respiratory state

Neonatal respiratory distress syndrome (NRDS) is a common condition in premature babies. Its symptoms initially present as shortness of breath. In severe cases, the infant may gradually become unable to breathe or even stop breathing for a long period of time. In the early stages of NRDS, the respiratory rate of new-born increases, but the ventilator needs to respond immediately to ensure that normal breathing is maintained. Neonates have a different breathing frequency and intensity to adults, so it is also a reflection of the stability and compatibility of the system if it works for different patients.

6.2.5 Evaluation

In order to assess the error between the output tidal volume and the reference signal, the error calculation formula is defined below.

$$error = \sqrt[2]{\frac{\sum_{i=0}^{n}(y_i - x_i)^2}{n}} \tag{6.21}$$

where y_i is the actual output tidal volume data, x_i is the ideal reference data, and n is the number of total data.

6.3 Results

6.3.1 EIT simulation results to estimate the tidal volume

In order to calculate the changes in tidal volume of the lungs, two imaging modalities of EIT reconstructed images will be presented. One is the traditional conjugate gradient descent method of 3D imaging algorithm and the other is the deep learning based algorithm, RP-UNet.

a) CG algorithm simulation results

The lungs will be evenly divided into seven regions vertically, and the tidal volume of each region was calculated based on reconstructed EIT image of one layer, via the CG algorithm. Figure 6-6 shows the entire respiratory cycle of one of the layers, accompanied by 50 dB of noise. With the end-expiratory state as a reference, the tidal volume inside the lung gradually increases and then decreases. The first two rows show the inspiratory process, so that the blue area in the reconstructed image increases and the tidal volume increases, gradually allowing tidal volume changes in the lung to be observed. In the second two rows, during expiration, the blue area gradually changes to red and the volume inside the lung decreases gradually.

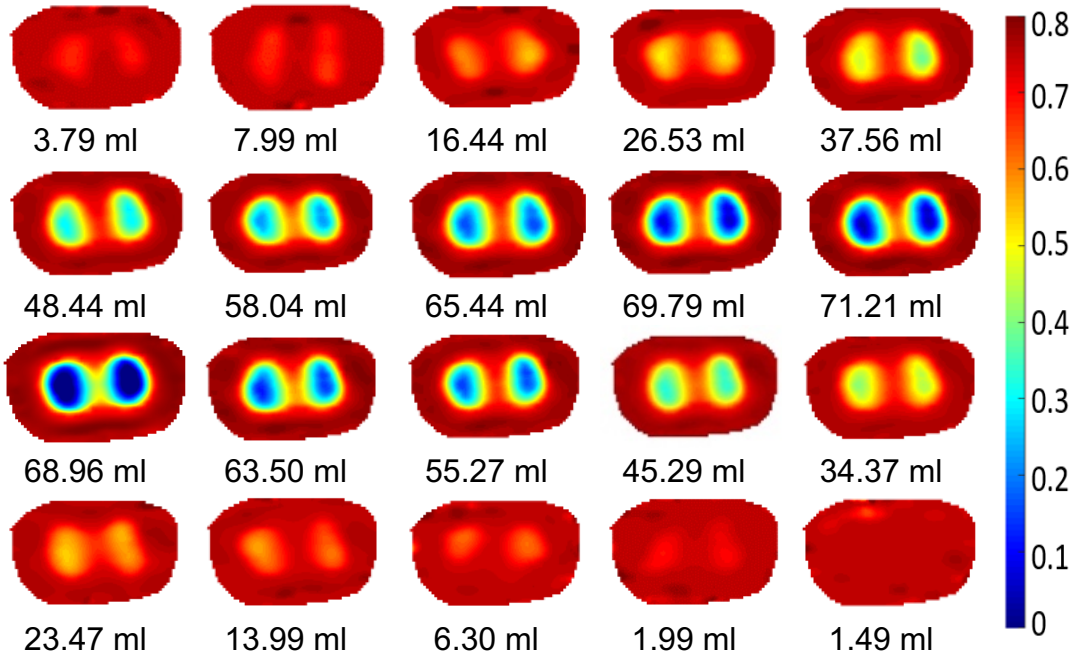

Figure 6-6: Simulation results of the breathing cycle with 50 dB noise in single layer.

Whereas the tidal volume of the entire lung changes over half a cycle as shown in Figure 6-7, the reconstructed images in each row are reconstructed by different layers of the lung at the same moment. The images in each column are the changes over half a cycle for the same layer. The average change in tidal volume for the whole lung is 500 mL, while the average change in each layer is 72 ml. Because the boundaries of the lungs are not clear in the reconstructed images, the error in estimating the cross-sectional area of the lungs will be related to the threshold value set.

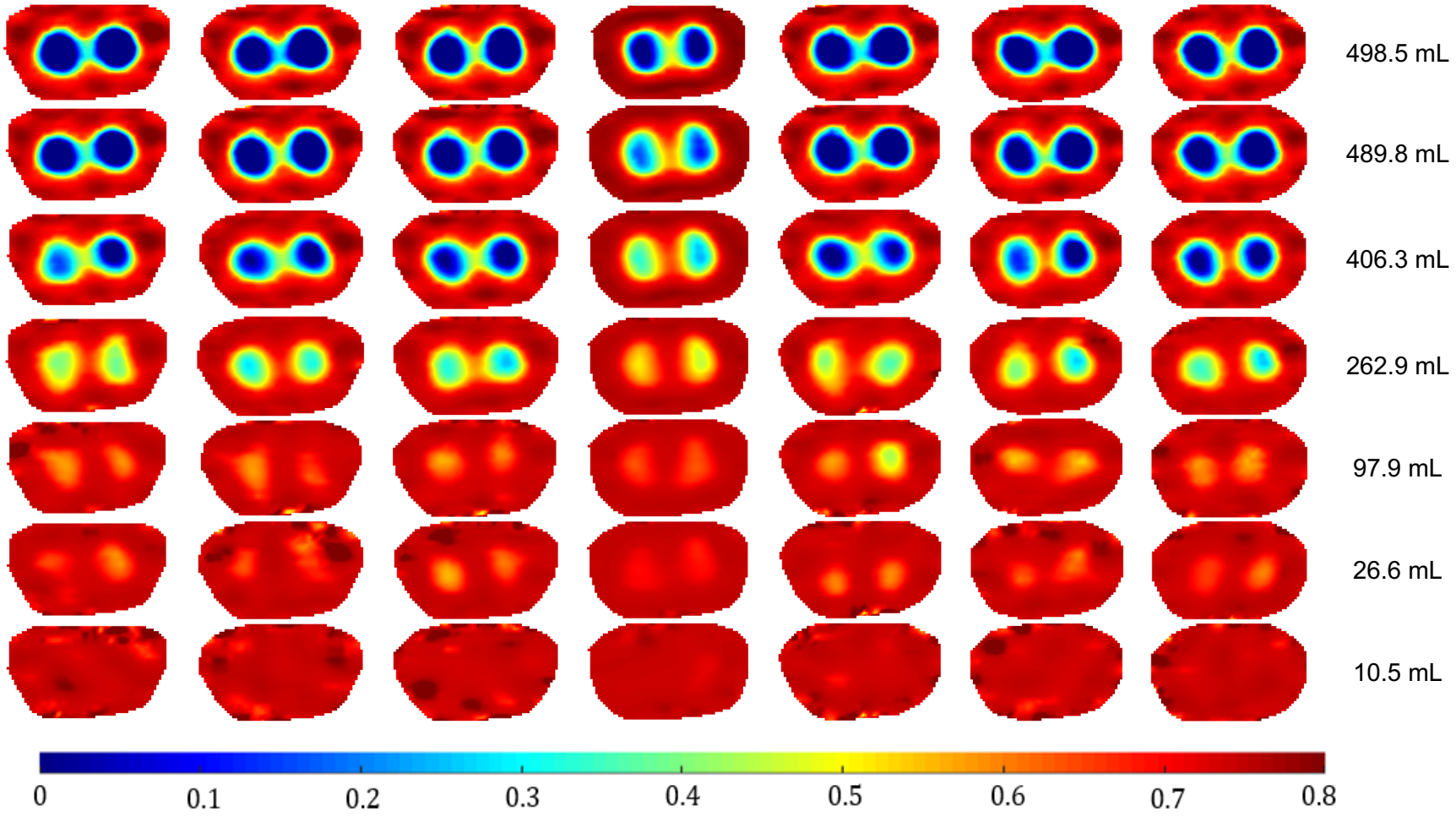

Figure 6-7: Change of the tidal volume of the entire lung with 50 dB during half breathing cycle.

b) The results of RP-Unet

As there are errors in the reconstructed images of the EIT via CG algorithm, the estimated volumes will be affected, especially if the contours of the lungs are not clear. Therefore, deep learning based algorithms for reconstructing images are applied to obtain more accurate reconstructed images of the EIT.

Based on the results of the reconstructed images in Chapter 4, the RP-UNet can find the contours of the lung more clearly. As shown in Figure 6-8, the color of the lungs is closest to the dark blue in the end-inspiratory state, when the tidal volume is greatest. During exhalation, the color of the lungs gradually changes from blue to red as the tidal volume decreases. Therefore, the estimated tidal volume corresponding to each stage is shown in Table 6-3. The table gives a clearer result of the progression of breathing as the tidal volume becomes larger and then smaller.

Table 6-3: Estimated tidal volume for a breathing cycle.

	Estimated tidal volume (mL)					
Inhalation	0.69	15.63	62.11	106.88	151.26	194.25
	238.77	282.17	328.66	378.58	418.50	463.79
Exhalation	489.49	442.22	399.69	351.18	307.07	259.75
	216.78	172.93	129.69	86.44	38.12	1.09

Table 6-4: The ground truth of tidal volume.

	The ground truth of tidal volume (mL)					
Inhalation	0	20	60	110	155	200
	240	285	330	380	420	460
Exhalation	490	440	400	350	305	260
	220	175	130	90	45	0

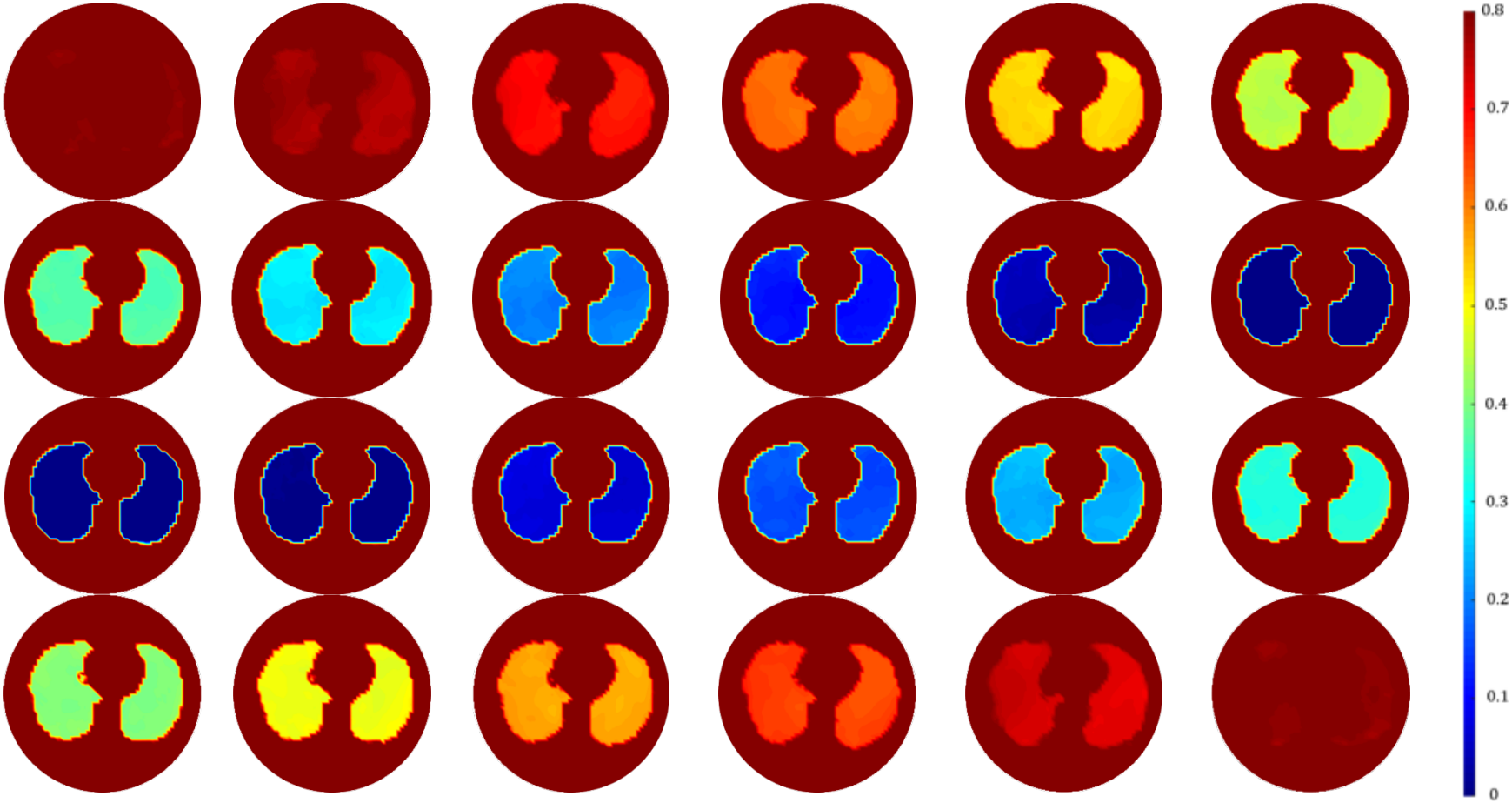

Figure 6-8: Simulation results of a whole breathing cycle with RP-UNet.

6.3.2 The results of single lung model control system

a) Mechanical ventilation based on CG algorithm

Based on the images of the EIT obtained by the CG algorithm as feedback, the tidal volume output curves for the single-lung model are shown in Figure 6-9 and 6-10. The two graphs show the curves of tidal volume over time for both the absence and presence of disturbance, respectively. The solid green line is the result of the tidal volume output, while the solid orange line represents the reference signal. At the peak of the curve there is a constant difference between the two, averaging 18.2 mL. What is more, there is a delay of 0.082s between the output curve and the reference signal.

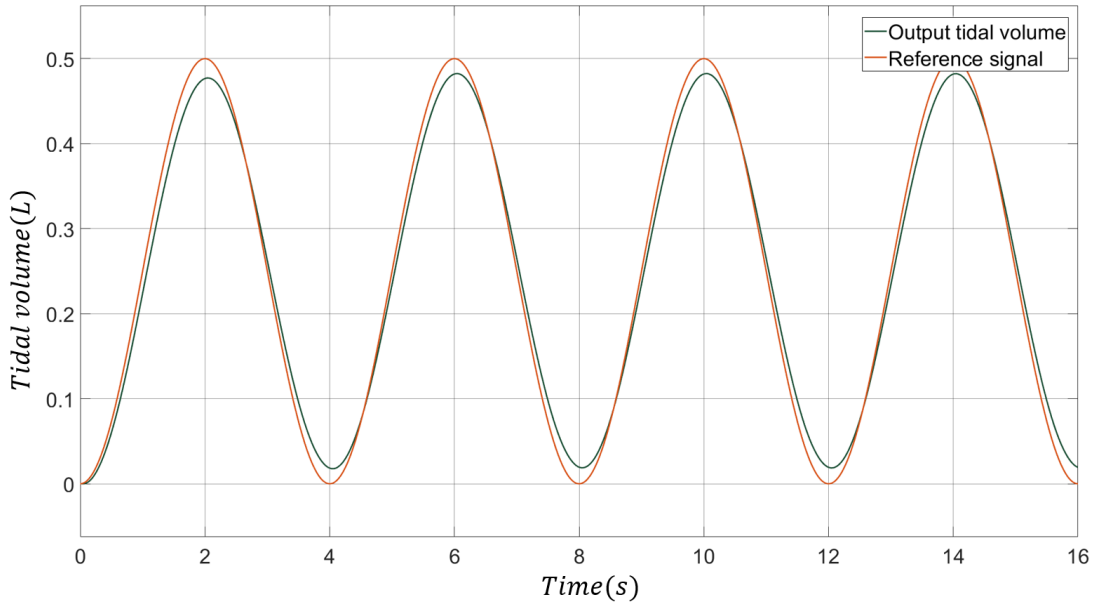

Figure 6-9: Tidal volume of the single lung model control system based on CG algorithm.

In Figure 6-10, a disturbance lasting 0.5 s occurs at the 10th second, then the output curve can respond quickly in order to eliminate the effect of the disturbance on the system rapidly. The error of the mechanical ventilation system, as shown in Table 6-5, is greater for the system subjected to the disturbance than for the absence of the disturbance.

Table 6-5: Error of the mechanical ventilation for different cases.

	Normal case	With disturbance
Error (mL)	56.5	60.0

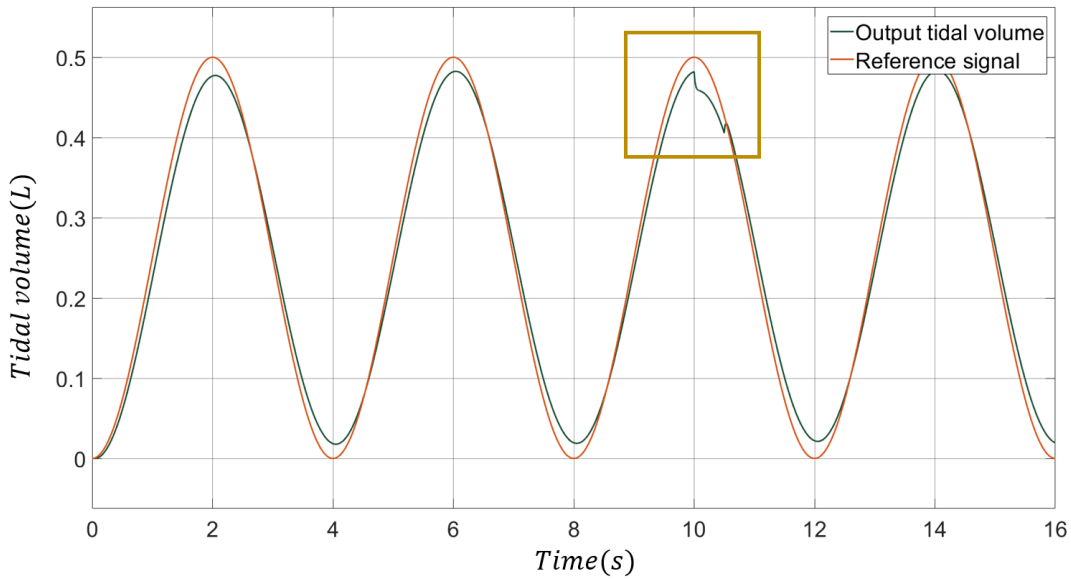

Figure 6-10: Tidal volume of the single lung model control system with a disturbance.

b) Mechanical ventilation based on RP-UNet algorithm

To compare the impact of the two algorithms on the system, the next experiments are done based on the deep learning algorithm, with the same cases in the Section 6.3.2.a), which have been demonstrated in Figure 6-11 and Figure 6-12.

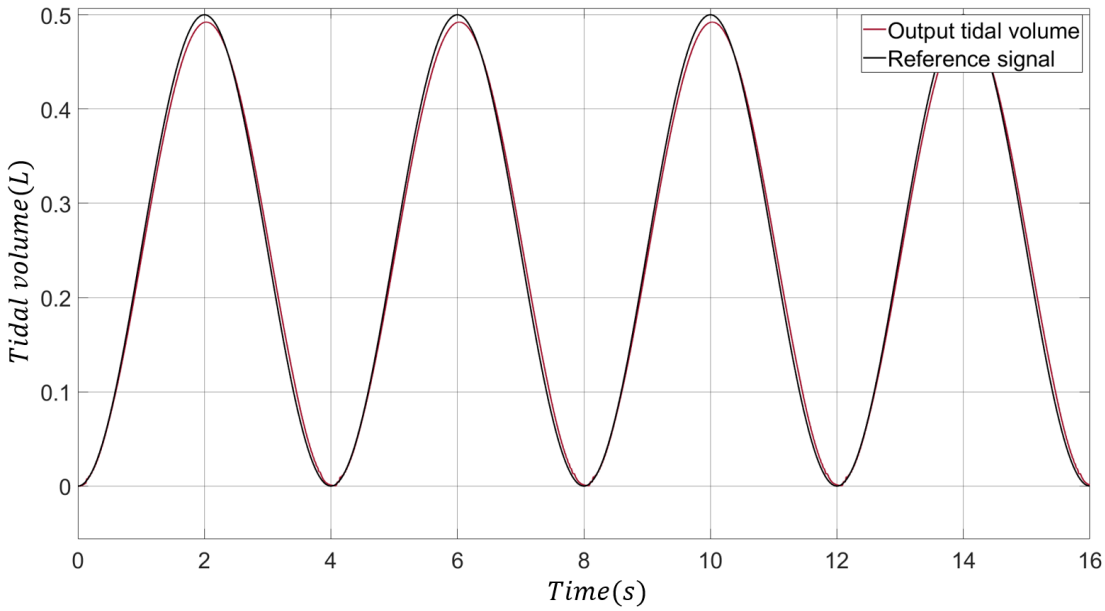

Figure 6-11: Tidal volume of the single lung model control system based on RP-UNet algorithm.

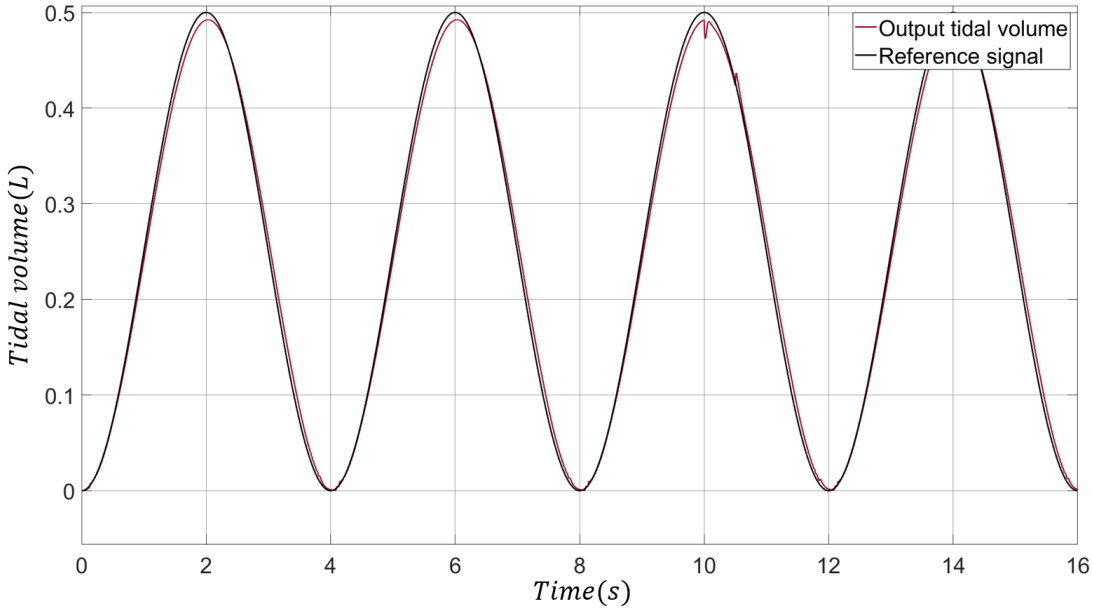

Figure 6-12: Tidal volume of the single lung model control system with a disturbance for RP-UNet.

The error of tidal volume based on RP-UNet is more accurate than CG algorithm as shown in Table 6-6.

Table 6-6: Error of the mechanical ventilation for two cases based on RP-UNet.

	Normal case	**With disturbance**
Error (mL)	29.4	30.0

The tidal volume results for the four different extreme respiratory conditions are shown in Figure 6-13 to 6-16. The red curve in the graph represents the output of the tidal volume and the black curve is the reference signal. It can be seen that there is a large error in the system during the initial start-up. This is because during the initial start-up the system goes from inactive to operational and the motor needs to be increased in speed to achieve the required conditions. The initialisation state in the system is the end-expiratory state in this case, so it starts with a tidal volume equal to 0. In fact, the desired initial tidal volume can be any value and the cases in this part are only the extreme examples in order to verify the reliability of the system. However, the response of the system is very fast, with a rise time of only 0.16 s. With the patient's breathing normally maintained and no interference obtained, there is a constant time delay of 0.05 s between the output tidal volume curve and the reference signal. In addition, there is a stable error at the peak, which is 8.1 mL. Delays and errors arise on the one hand from delays between system signal transmissions and on the other hand from errors in the system, for example in the process of EIT estimating the volume, which itself is subject to a certain amount of error.

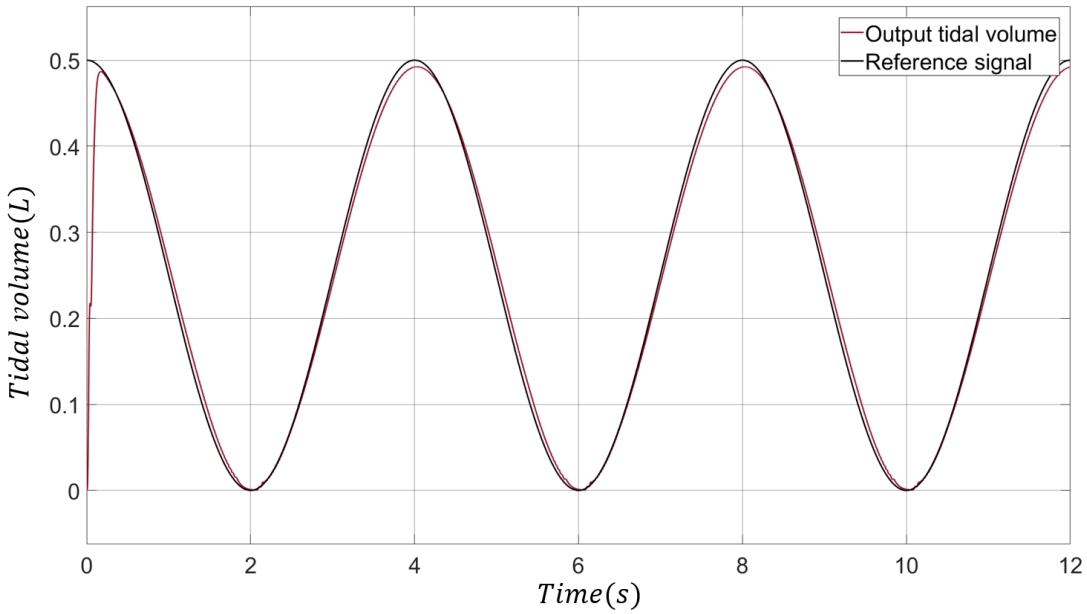

Figure 6-13: Tidal volume of single lung model about normal breathing cycle.

Figure 6-14 shows the results of the response to the input when the system is disturbed. When the disturbance occurs in the fourth second, the system can respond quickly and reach a steady state.

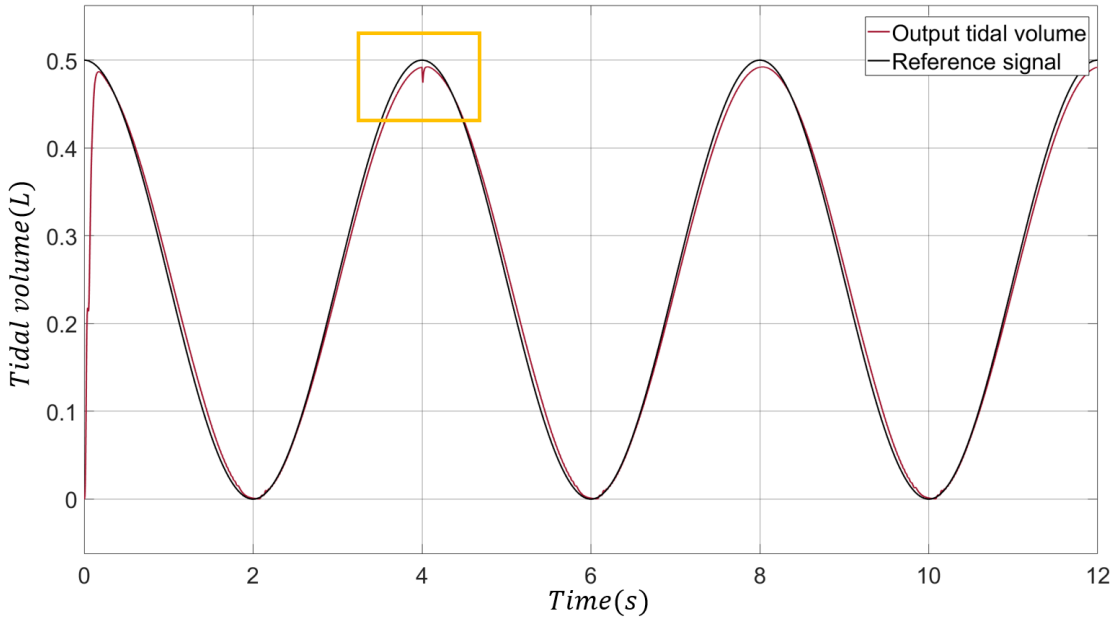

Figure 6-14: Tidal volume of single lung model with a disturbance.

Figure 6-15 depicts one of the scenarios in a general anaesthetic procedure where the patient's respiratory process is gradually weakening. As a result, the tidal volume provided by the ventilator gradually increases and finally stabilises. Similar to the previous two cases, there is an error during the initial start-up process, with a rise time of 0.14 s.

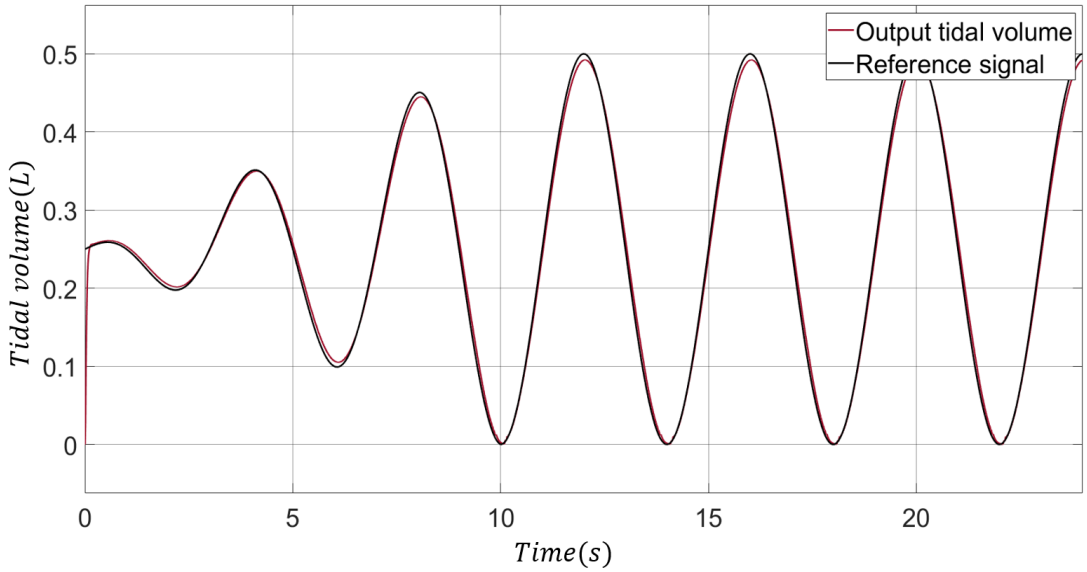

Figure 6-15: Tidal volume of single lung model for the general anaesthesia.

The final case is that of a new-born baby breathing, as shown in Figure 6-16. The respiratory rate of new-born is faster, and the intensity of breathing is weaker, compared to an adult. The rise time of the system during this process is 0.13 s. When the system is stable, the error between the output tidal volume curve and the reference signal is 3.9 mL and the time delay is 0.89 s.

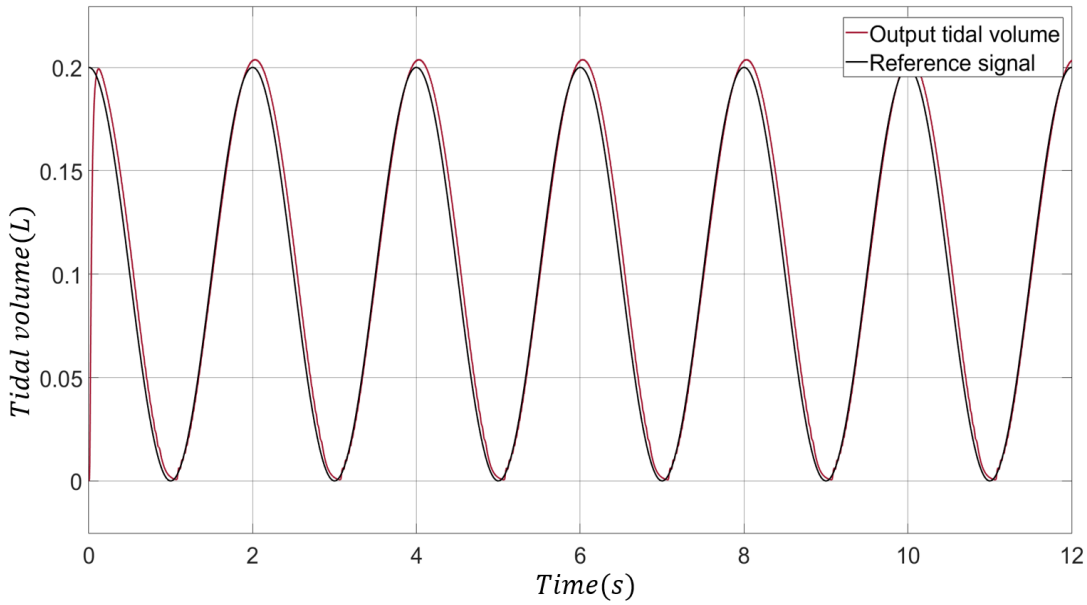

Figure 6-16: Tidal volume of single lung model for neonatal respiratory.

The error of the mechanical ventilation for different cases is shown in the Table 6-7. The large error is mainly due to a large error during start-up stage.

Table 6-7: Error of the mechanical ventilation for four cases based on RP-UNet.

	Normal breathing	With disturbance	Anaesthesia case	neonatal respiratory
Error (mL)	94.5	94.7	51.9	36.5

6.3.3 The results of multi-lung control system

In the multi-lung model, four lungs are simulated (two lobes in each of the left and right lungs) and the system observes the results of the four lungs as a whole. However, it is still possible to assign different parameters to different lungs to simulate different effects. To further realise a more realistic lung model, the reference signal also varies with the pressure curve generated by the muscle, similar to the RC charge and discharge curve, with the muscle contraction process corresponding to the charging process of the RC circuit and the muscle relaxation process corresponding to the discharging process

of the RC circuit [143]. According to Figure 6-17 there is a time delay of 0.018s in the response curve compared to the reference signal, and the error of the peaks is 62.0 mL.

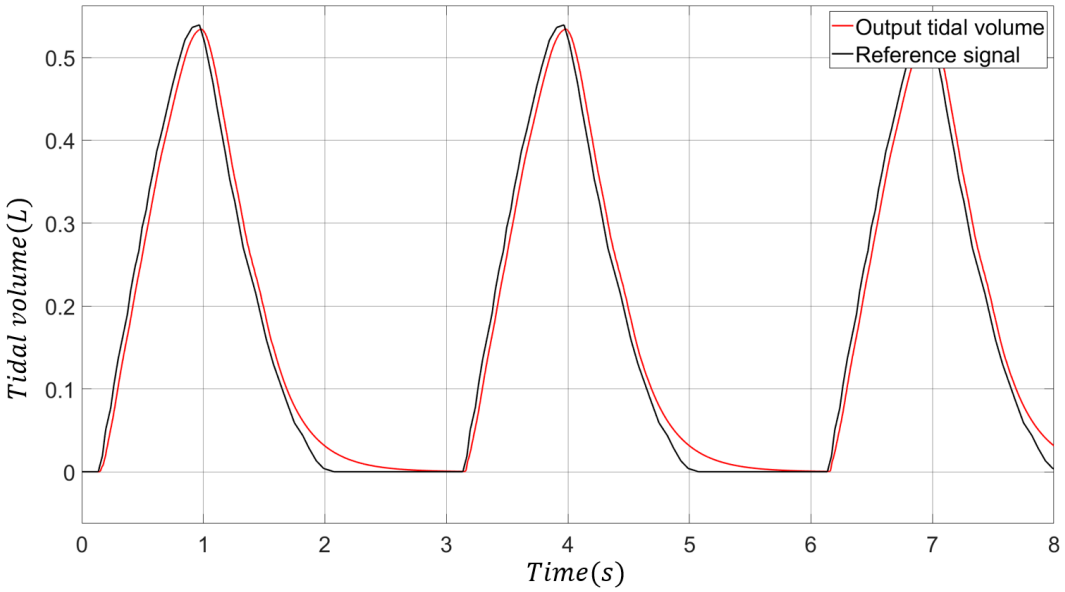

Figure 6-17: Tidal volume of multi-lung model without disturbance.

Figure 6-18 represents the curves of tidal volume over time for the four components of the lung. The results show that at the same airway resistance, the pressure into the lungs is the same. Therefore, the greater the compliance of the lung, the greater the ventilation capacity. When lung compliance is consistent, the greater the airway resistance, the greater the pressure, resulting in the poorer the ventilation capacity. This is because lung compliance is a response to the ease with which deformation can occur. Greater compliance indicates a greater capacity for deformation and the ability to cause greater deformation with less external force. That is means expandable, for example, it can cause a large change in lumen volume in response to a small transmural pressure, as the Equation 6.22 shows. The results in this chapter are consistent with medical research on lung [144] so the model proposed in this chapter can be shown to be valid and applicable. Furthermore, not only does each of the different lung sections agree with the expected results, but their sum is the tidal volume of the whole lung, which still

follows the objective function well. Therefore, it can be assumed from the joint results of the two aspects that the model works properly.

$$C = \frac{\Delta V}{\Delta P} \tag{6.22}$$

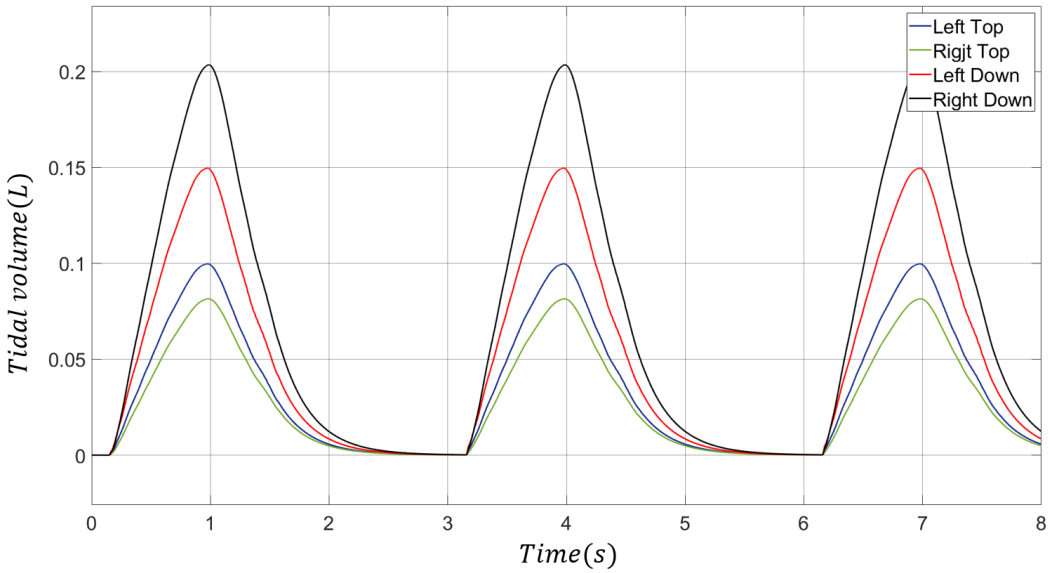

Figure 6-18: The tidal volume of different lung without disturbance.

The response curves subject to disturbance are shown in Figure 6-19 and 6-20. At the fourth second, the tidal volume suddenly increases, which is the external disturbance. Errors for mechanical ventilation in the multi-lung mode are shown in Table 6-8. In the presence of interference, the error remains a relatively small one. The system can respond quickly and eliminate the disturbance, which shows that the anti-disturbance capability and stability of the system are excellent.

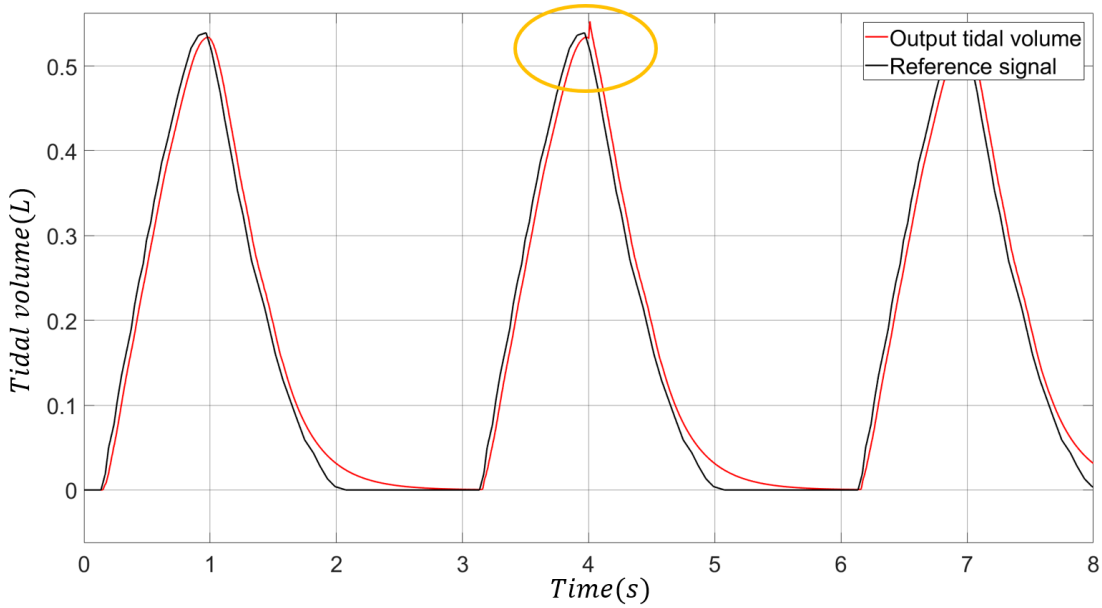

Figure 6-19: Tidal volume of multi-lung model with disturbance.

Table 6-8: Error of mechanical ventilation for multi-lung system.

	Without disturbed	With disturbed
Error (mL)	69.2	69.4

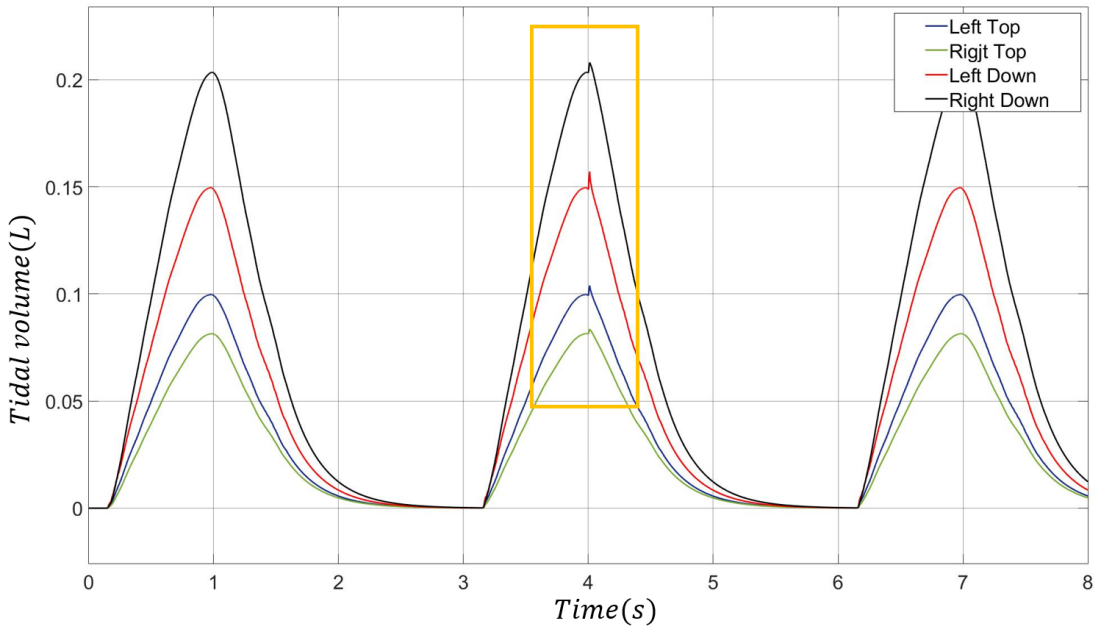

Figure 6-20: Tidal volume of different lung without disturbance.

6.4 Discussion

In this study, the EIT image reconstruction model, CG and RP-UNet, were applied to reconstruct images of the conductivity distribution of the lung. However, based on the analysis of the results, the RP-UNet allows for better monitoring and control of the effects. This setup converts the volume changes in the sensor into three-dimensional space. As the conductivity of the chest cavity is almost constant during the measurement, the conductivity changes in the sensor are mainly attributed to changes in the conductivity of the lung. This approach can provide more information than just a determination of whether damage has occurred within the lung. It can visualise the location of the lung damage and the extent of the damage. More importantly, it can monitor the functionality of the lung at any location in real time. In order to verify the stability and robustness of the control system, different breathing patterns are applied. In future studies, optimisations can be made to combine temporal information to make predictions about the tidal volume of the breathing process in order to improve the accuracy of the measurements.

In summary, the results show that changes in the tidal volume of the lungs during respiration can be monitored in real time by the EIT and converted into feedback signals for the control of mechanical ventilation systems. The EIT based mechanical ventilation control system is a new medical device with great potential and competitiveness. This approach is more intelligent and provides more effective medical information. The implementation of closed-loop control is an important part of advancing mechanical ventilation into intelligent control. Although it does not have the same spatial resolution as other imaging technologies such as CT and MRI, EIT has several distinct advantages over existing technologies, including non-destructive, high temporal resolution, low cost, portable portability, and long-term real-time monitoring. Overall, combining the benefits of EIT with more medical devices is an important direction to explore, such as real-time monitoring of the location and size of lung tumours.

6.5 Summary

In this chapter, an EIT imaging based mechanical ventilation system is developed to monitor the tidal volume of the lung with real-time imaging of the EIT and to act as feedback to the control system for closed-loop control. The technique is not only demonstrated in a single lung, but it is easily reused in multiple lung patterns. This chapter uses two EIT reconstruction algorithms to estimate lung tidal volumes, including the CG algorithm and the RP-UNet model, discussed in Chapters 3 and 4. The results show that RP-UNet is more advantageous in estimating tidal volumes because of the clear contours and more accurate conductivity distribution. For the first time, tidal volumes were estimated from cross-sections of lungs in the EIT and the relationship between lung conductivity and tidal volume was explored. More importantly, it was used to guide the control system in regulating parameters. The potential and applicability of the EIT as a feedback system was evaluated, along with the feasibility of a closed-loop control system to monitor tidal volume changes in real time for different types of respiratory states and under different lung models. This is the first mechanical ventilation system to regulate a control system based on feedback closed-loop of EIT images and to demonstrate real-time changes in tidal volume under different models. It is an important step towards intelligent mechanical ventilation to enable online monitoring of tidal volume changes and lung injury in 3D lungs. It also enables a perfect integration of the EIT imaging system with medical devices.

Chapter 7 Conclusions and future work

The focus of this thesis is to develop a methodological and theoretical basis for the application of EIT in real-time monitoring and guiding the controller of the mechanical ventilation system. The relationship between lung conductivity and tidal volume of EIT reconstructed images is investigated for real-time monitoring of lung tidal volume during respiration and regulating the control system. Based on the structure and functional of the lung, different lung models were developed to verify the robustness of the EIT imaging system and the mechanical ventilation system, as well as the feasibility of their fusion. Thus, the limitation and resolution of lung detection by the EIT were calculated from these models, while tidal volume changes were estimated and tested. As one

of the most important factors affecting the accuracy of EIT images, reconstruction errors were analysed by developing a joint simulation method using COMSOL Multiphysics software and MATLAB. Moreover, the lung model is also one of the most important factors affecting the control system, so a joint simulation with Simulink was combined to the system.

7.1 Summary of findings

Although EIT is very promising for medical applications, based on its advantages of non-invasiveness, low cost, high temporal resolution and no side effects, it still faces many challenges. The main challenges arise from spatial imaging resolution, sensing strategies, and information fusion with other medical devices. In light of these issues, this thesis explores the application of EIT as an emerging medical device in mechanical ventilation systems. A comprehensive study is conducted on innovative, high performance and fast image reconstruction algorithm research, fused sensor development and applications. The detailed work contributed in this thesis is summarised below.

In the Chapter 3, an improved method of reconstructing images in three dimensions is presented and the feasibility of a single layer electrode EIT device for three-dimensional imaging is demonstrated. The potential of EIT for lung monitoring is also explored, providing the basis for subsequent chapters. By adjusting the parameters of the algorithm and considering performance and results, the optimal settings of the improved algorithm for lung monitoring and ways to avoid amplification of measurement errors are derived. Additional improvements to the sensitivity matrix were made to assess the impact of the image reconstruction algorithm on the quality of the reconstructed images. The modified sensitive map can be used more effectively in the image reconstruction process to reduce artefacts in the images and improve image quality and robustness. The improved image reconstruction algorithm is suitable for long term monitoring and analysis of conductivity changes in the reconstructed object, as it achieves an increase in imaging speed with a little sacrificing resolution. This chapter serves as the foundations of the thesis for monitoring changes in tidal volume of the lung.

In the Chapter 4, two deep learning based image reconstruction algorithms are proposed for monitoring functional disorders of the lung. Multiple lung models of the combined CT images are built for simulating different patients as well as different diseases, while using these data to create a database. These models are then used to estimate the theoretical resolution of the different image reconstruction methods for lung imaging. Two algorithms for fast imaging were innovated with different perspectives to obtain well-defined lung boundaries and a homogeneous internal conductivity distribution. At the same time, quantitative estimation of conductivity changes can provide more detailed information about the lesion condition in different regions. More importantly, real-time reconstruction of small conductivity changes due to tidal volume changes in the lung can be achieved with the innovative models, which makes a significant contribution to real-time control of tidal volume with mechanical ventilation. Thus, the two proposed algorithms have the potential to be widely used for complex medical image segmentation tasks.

In the Chapter 5, a feasibility study is presented to investigate the potential of a closed-loop volumetric control strategy and the potential of monitoring tidal volumes in real time. The ultrasound sensor was used to measure the water level in the tank and estimate changes in tidal volume. The combination of multiple sensors and mechanical ventilation becomes an important milestone towards intelligent ventilation. The experimental results show that the system can monitor tidal volume changes in real time and implement a closed-loop control strategy. In addition, the developed device was thoroughly evaluated in terms of error analysis, system stability and response time. Thus, as a new fusion mechanical ventilation device, the system has more room for improvement and is a useful starting point for a fusion device with EIT.

In Chapter 6, a mechanical ventilation system based on EIT image control is developed to enable the closed-loop control system of the fusion device. The system allows real-time monitoring of tidal volume changes in the lung via the EIT and the relationship between lung conductivity and tidal volume. Different lung models and breathing patterns have been modeled to assess the suitability of the EIT system as feedback, as well as the feasibility and stability of the overall innovative system. This study establishes the platform for the integration of the EIT with other medical devices to provide more meaningful information to guide treatment. This emerging medical device allows visualizing the location of lung damage and tumours in real time over a long period of time to provide appropriate treatment options as early as possible. The fully automated control system is a sign of the progress towards intelligence.

In conclusion, the work of proofing the concepts presented in this thesis makes it possible to perform high quality and stable 2D/3D lung imaging, as well as long-term and high temporal resolution tidal volume monitoring. The high quality images ensure reliable control and quantitative analysis of the mechanical ventilation system.

7.2 Limitation and future work

This thesis focuses on progress in the development of an intelligent EIT-guided controlled mechanical ventilation system. It can be applied with different lung models to guide different breathing patterns, and its stability and accuracy have been verified in several ways. However, there are still some limitations in the experimental process that need to be addressed in future research.

7.2.1 Image reconstruction using spatiotemporal information

Regarding image reconstruction, the improved CG algorithm is currently proposed to be used for 3D imaging but its spatial resolution is lower compared to deep learning based methods, DSA-UNet and RP-UNet. The CG algorithm improves the 3D imaging speed, with measured voltages acquired through a single layer of electrodes, and ensures that all reconstructed images are not independent, as they imaged with the same measured voltages obtained from the same time points. However, the boundaries of the lung are not clearly defined and there is a certain amount of error in estimating the 3D image using multiple 2D images, due to errors in the measured voltage and the number of cross-sections. On the other hand, although the imaging speed has improved, there are limitations in terms of real-time performance. Therefore, in future work, 3D spatiotemporal regularisation methods for image reconstruction could be considered to add temporal and spatial information to improve the accuracy to observe conductivity changes in the lung.

7.2.2 Database extensions

The dataset in the experiment is based on CT images of 19 individuals. Although a lot of data can be derived by inverting, zooming in, zooming out and adding noise, there is still less diversity in the database. Therefore, more CT images of different patients at different stages can be added in future work to improve the robustness of the deep learning algorithm. In addition, the development of 3D DSA-UNet and RP-UNet is particularly important as conventional 3D reconstruction algorithms cannot specify the boundaries of

the lung. 3D models can provide a more accurate imaging of tidal volume changes and be used to control mechanical ventilation, which can improve the accuracy of the system. It is also simpler to observe whether the lung appears to be over-collapsing and over-expanding. What is more, the image reconstruction can also be predicted in conjunction with temporal information. If tidal volume changes and disease progression could be predicted in advance, then early intervention and treatment can be made when abnormalities are present in the tissues and organs to save patient's life.

In addition, the neural network model proposed in this work has relatively poor generalisation ability and can only be used for lung models. It cannot be applied directly to other applications. Therefore, there is a limitation in the application scenario. If the network needs to be used in other scenarios, such as the brain detection, more brain models and dataset of the brain are needed, and re-learning and re-tuning of parameters are required.

7.2.3 Multi-parameter controller

Currently, only tidal volume information is used for regulation in the proposed EIT-guided mechanical ventilation system. This resulted in a loss of spatial information in the EIT image. Without the aid of the EIT image, it is impossible to identify where the problem areas are from the tidal volume control results alone, and the original two-dimensional information is compressed to one dimension. However, information that EIT can provide is much richer and should be combined with a greater diversity of information to guide the movement of mechanical ventilation to improve the accuracy of the system. For example, the EIT can calculate the ventilation volume in the region of interest. If there is an over-collapse in the lung, then inputting too much tidal volume will only result in over-expansion of other regions. More functional lung information can therefore be combined to regulate the tidal volume. Meanwhile, neural network control could be developed to enable a non-linear multi-input control system. Intelligent EIT-guided control systems will be further refined.

7.2.4 More valuable experimental verification

The current closed-loop control is only available as simulation results, and further development is needed for real-time closed-loop control system based on EIT. Extensive and repeated cross-validation experiments with lung imaging are necessary to assess the reliability and reproducibility of the derived methods. In addition, long-term monitoring experiments should be performed with real lungs to evaluate lung functionality and device stability. Furthermore, at this stage, there is only a limited sense of information fusion. It is possible to extend this concept of fusion devices so that EIT can be combined with more medical devices to provide more image information and assist in treatment.

7.3 Conclusion

Although there are limitations in this work, it is these limitations that give us more scope and direction for future research. Overall, the proposed approach can provide more medical information. The implementation of closed-loop control is an important part of advancing mechanical ventilation into intelligent stage. Therefore, the EIT-based intelligent mechanical ventilation control system is a new medical device with great potential and competitiveness. In the future more information integration will be developed to ensure that medical devices can be safely put into clinical practice.

References

[1] Z. Zhao, F. Fu, and I. Frerichs, "Thoracic electrical impedance tomography in Chinese hospitals: a review of clinical research and daily applications," *Physiological measurement,* vol. 41, no. 4, p. 04TR01, 2020.

[2] K. Lee, E. J. Woo, and J. K. Seo, "A fidelity-embedded regularization method for robust electrical impedance tomography," *IEEE transactions on medical imaging,* vol. 37, no. 9, pp. 1970-1977, 2017.

[3] W. R. Lionheart, "EIT reconstruction algorithms: pitfalls, challenges and recent developments," *Physiological measurement,* vol. 25, no. 1, p. 125, 2004.

[4] M. Wang, Y. Ma, N. Holliday, Y. Dai, R. A. Williams, and G. Lucas, "A high-performance EIT system," *IEEE Sensors Journal,* vol. 5, no. 2, pp. 289-299, 2005.

[5] R. H. Bayford, "Bioimpedance tomography (electrical impedance tomography)," *Annu. Rev. Biomed. Eng.,* vol. 8, pp. 63-91, 2006.

[6] K. Y. Aristovich, B. C. Packham, H. Koo, G. S. Dos Santos, A. McEvoy, and D. S. Holder, "Imaging fast electrical activity in the brain with electrical impedance tomography," *NeuroImage,* vol. 124, pp. 204-213, 2016.

[7] G. K. Wolf *et al.*, "Mechanical ventilation guided by electrical impedance tomography in experimental acute lung injury," *Critical care medicine,* vol. 41, no. 5, pp. 1296-1304, 2013.

[8] A. Shono and T. Kotani, "Clinical implication of monitoring regional ventilation using electrical impedance tomography," *Journal of Intensive Care,* vol. 7, no. 1, pp. 1-10, 2019.

[9] P. Metherall, D. C. Barber, R. H. Smallwood, and B. H. Brown, "Three-dimensional electrical impedance tomography," *Nature,* vol. 380, no. 6574, pp. 509-512, 1996.

[10] B. M. Eyuboglu, B. H. Brown, and D. C. Barber, "In vivo imaging of cardiac related impedance changes," *IEEE Engineering in medicine and biology magazine,* vol. 8, no. 1, pp. 39-45, 1989.

[11] B. Liu *et al.*, "Non-invasive Imaging the Relative Changes in Cerebral Blood Volume during Total Aortic-arch Replacement Using Electrical Impedance Tomography: a First Study," in *Proceedings of the Third International Symposium on Image Computing and Digital Medicine*, 2019, pp. 308-313.

[12] I. Frerichs *et al.*, "Chest electrical impedance tomography examination, data analysis, terminology, clinical use and recommendations: consensus statement of the TRanslational EIT developmeNt stuDy group," *Thorax,* vol. 72, no. 1, pp. 83-93, 2017.

[13] J. Xiang, Y. Dong, M. Zhang, and Y. Li, "Design of a magnetic induction tomography system by gradiometer coils for conductive fluid imaging," *IEEE Access,* vol. 7, pp. 56733-56744, 2019.

[14] W. Yang and L. Peng, "Image reconstruction algorithms for electrical capacitance tomography," *Measurement science and technology,* vol. 14, no. 1, p. R1, 2002.

[15] M. Wang and W. Yin, "Electrical impedance tomography," ed: Google Patents, 2005.

[16] H. Wang, C. Wang, and W. Yin, "A pre-iteration method for the inverse problem in electrical impedance tomography," *IEEE Transactions on Instrumentation and Measurement,* vol. 53, no. 4, pp. 1093-1096, 2004.

[17] Y. Yang, J. Jia, N. Polydorides, and H. McCann, "Effect of structured packing on EIT image reconstruction," in *2014 IEEE International Conference on Imaging Systems and Techniques (IST) Proceedings*, 2014: IEEE, pp. 53-58.

[18] B. Jin, T. Khan, and P. Maass, "A reconstruction algorithm for electrical impedance tomography based on sparsity regularization," *International Journal for Numerical Methods in Engineering,* vol. 89, no. 3, pp. 337-353, 2012.

[19] S. Osher, M. Burger, D. Goldfarb, J. Xu, and W. Yin, "An iterative regularization method for total variation-based image restoration," *Multiscale Modeling & Simulation,* vol. 4, no. 2, pp. 460-489, 2005.

[20] R. G. Baraniuk, "Compressive sensing [lecture notes]," *IEEE signal processing magazine,* vol. 24, no. 4, pp. 118-121, 2007.

[21] T. Blumensath and M. E. Davies, "Iterative thresholding for sparse approximations," *Journal of Fourier analysis and Applications,* vol. 14, no. 5, pp. 629-654, 2008.

[22] M. Schmidt, "Least squares optimization with L1-norm regularization," *CS542B Project Report,* vol. 504, pp. 195-221, 2005.

[23] A. Borsic, B. M. Graham, A. Adler, and W. R. Lionheart, "In vivo impedance imaging with total variation regularization," *IEEE transactions on medical imaging,* vol. 29, no. 1, pp. 44-54, 2009.

[24] B. Chen, J. F. Abascal, and M. Soleimani, "Electrical resistance tomography for visualization of moving objects using a spatiotemporal total variation regularization algorithm," *Sensors,* vol. 18, no. 6, p. 1704, 2018.

[25] Z. Zhou *et al.*, "Multifrequency electrical impedance tomography with total variation regularization," *Physiological Measurement,* vol. 36, no. 9, p. 1943, 2015.

[26] A. R. D. S. Network, "Ventilation with lower tidal volumes as compared with traditional tidal volumes for acute lung injury and the acute respiratory distress syndrome," *New England Journal of Medicine,* vol. 342, no. 18, pp. 1301-1308, 2000.

[27] F. F. Cruz, L. Ball, P. R. M. Rocco, and P. Pelosi, "Ventilator-induced lung injury during controlled ventilation in patients with acute respiratory distress syndrome: less is probably better," *Expert review of respiratory medicine,* vol. 12, no. 5, pp. 403-414, 2018.

[28] G. F. Nieman *et al.*, "Prevention and treatment of acute lung injury with time-controlled adaptive ventilation: physiologically informed modification of airway pressure release ventilation," *Annals of intensive care,* vol. 10, no. 1, pp. 1-16, 2020.

[29] C. Dos Santos and A. Slutsky, "Invited review: mechanisms of ventilator-induced lung injury: a perspective," *Journal of applied physiology,* vol. 89, no. 4, pp. 1645-1655, 2000.

[30] M. R. Wilson, S. Choudhury, M. E. Goddard, K. P. O'Dea, A. G. Nicholson, and M. Takata, "High tidal volume upregulates intrapulmonary cytokines in an in vivo mouse model of ventilator-induced lung injury," *Journal of Applied Physiology,* vol. 95, no. 4, pp. 1385-1393, 2003.

[31] L. Gattinoni, A. Protti, P. Caironi, and E. Carlesso, "Ventilator-induced lung injury: the anatomical and physiological framework," *Critical care medicine,* vol. 38, no. 10, pp. S539-S548, 2010.

[32] K. Kuchnicka and D. Maciejewski, "Ventilator-associated lung injury," *Anaesthesiology intensive therapy,* vol. 45, no. 3, pp. 164-170, 2013.

[33] L. Brochard, A. Slutsky, and A. Pesenti, "Mechanical ventilation to minimize progression of lung injury in acute respiratory failure," *American journal of respiratory and critical care medicine,* vol. 195, no. 4, pp. 438-442, 2017.

[34] D. Chiumello *et al.*, "Respiratory support in patients with acute respiratory distress syndrome: an expert opinion," *Critical care,* vol. 21, no. 1, pp. 1-8, 2017.

[35] A. Pesenti, A. Zanella, and N. Patroniti, "Extracorporeal gas exchange," *Current opinion in critical care,* vol. 15, no. 1, pp. 52-58, 2009.

[36] N. González-Pacheco, M. Sánchez-Luna, P. Chimenti-Camacho, M. Santos-González, P. Palau-Concejo, and F. Tendillo-Cortijo, "Use of very low tidal volumes during high-frequency ventilation reduces ventilator lung injury," *Journal of Perinatology,* vol. 39, no. 5, pp. 730-736, 2019.

[37] K. L. Hamlington *et al.*, "Alveolar leak develops by a rich-get-richer process in ventilator-induced lung injury," *PLoS One,* vol. 13, no. 3, p. e0193934, 2018.

[38] D. L. Grieco, L. Chen, and L. Brochard, "Transpulmonary pressure: importance and limits," *Annals of translational medicine,* vol. 5, no. 14, 2017.

[39] J. J. Marini, P. R. Rocco, and L. Gattinoni, "Static and dynamic contributors to ventilator-induced lung injury in clinical practice. Pressure, energy, and power," *American journal of respiratory and critical care medicine,* vol. 201, no. 7, pp. 767-774, 2020.

[40] J. Grune, A. Tabuchi, and W. M. Kuebler, "Alveolar dynamics during mechanical ventilation in the healthy and injured lung," *Intensive care medicine experimental,* vol. 7, no. 1, pp. 1-20, 2019.

[41] A. S. Slutsky and V. M. Ranieri, "Ventilator-induced lung injury," *New England Journal of Medicine,* vol. 369, no. 22, pp. 2126-2136, 2013.

[42] H. F. Tregidgo, M. G. Crabb, A. L. Hazel, and W. R. Lionheart, "On the feasibility of automated mechanical ventilation control through EIT," *IEEE Transactions on Biomedical Engineering,* vol. 65, no. 11, pp. 2459-2470, 2018.

[43] P. P. Terragni *et al.*, "Tidal hyperinflation during low tidal volume ventilation in acute respiratory distress syndrome," *American journal of respiratory and critical care medicine,* vol. 175, no. 2, pp. 160-166, 2007.

[44] S. M. Maggiore, J. C. Richard, and L. Brochard, "What has been learnt from P/V curves in patients with acute lung injury/acute respiratory distress syndrome," *European Respiratory Journal,* vol. 22, no. 42 suppl, pp. 22s-26s, 2003.

[45] H. Luepschen, T. Meier, M. Grossherr, T. Leibecke, J. Karsten, and S. Leonhardt, "Protective ventilation using electrical impedance tomography," *Physiological measurement,* vol. 28, no. 7, p. S247, 2007.

[46] Z. Zhao, S. Pulletz, I. Frerichs, U. Müller-Lisse, and K. Möller, "The EIT-based global inhomogeneity index is highly correlated with regional lung opening in patients with acute respiratory distress syndrome," *BMC research notes,* vol. 7, no. 1, pp. 1-7, 2014.

[47] M. Bodenstein, S. Boehme, S. Bierschock, A. Vogt, M. David, and K. Markstaller, "Determination of respiratory gas flow by electrical

impedance tomography in an animal model of mechanical ventilation," *BMC pulmonary medicine,* vol. 14, no. 1, pp. 1-11, 2014.

[48] B. K. Walsh and C. D. Smallwood, "Electrical impedance tomography during mechanical ventilation," *Respiratory Care,* vol. 61, no. 10, pp. 1417-1424, 2016.

[49] Z. Zhao, D. Steinmann, I. Frerichs, J. Guttmann, and K. Möller, "PEEP titration guided by ventilation homogeneity: a feasibility study using electrical impedance tomography," *Critical Care,* vol. 14, no. 1, pp. 1-8, 2010.

[50] C. J. Roth *et al.*, "Correlation between alveolar ventilation and electrical properties of lung parenchyma," *Physiological measurement,* vol. 36, no. 6, p. 1211, 2015.

[51] T. Becher *et al.*, "Individualization of PEEP and tidal volume in ARDS patients with electrical impedance tomography: a pilot feasibility study," *Annals of intensive care,* vol. 11, no. 1, pp. 1-10, 2021.

[52] W. R. Lionheart, J. Kaipio, and C. N. McLeod, "Generalized optimal current patterns and electrical safety in EIT," *Physiological measurement,* vol. 22, no. 1, p. 85, 2001.

[53] A. V. Pigatto, T.-J. Kao, J. L. Mueller, C. D. Baker, E. M. DeBoer, and O. Kupfer, "Electrical impedance tomography detects changes in ventilation after airway clearance in spinal muscular atrophy type I," *Respiratory Physiology & Neurobiology,* vol. 294, p. 103773, 2021.

[54] A. M. Ambrósio *et al.*, "Assessment of Regional Ventilation During Recruitment Maneuver by Electrical Impedance Tomography in Dogs," *Frontiers in Veterinary Science,* p. 1692, 2022.

[55] D. Maciejewski, Z. Putowski, M. Czok, and Ł. J. Krzych, "Electrical impedance tomography as a tool for monitoring mechanical ventilation. An introduction to the technique," *Advances in Medical Sciences,* vol. 66, no. 2, pp. 388-395, 2021.

[56] S. Hannan, M. Faulkner, K. Aristovich, J. Avery, M. Walker, and D. Holder, "Imaging fast electrical activity in the brain during ictal

epileptiform discharges with electrical impedance tomography," *NeuroImage: Clinical,* vol. 20, pp. 674-684, 2018.

[57] T. K. Bera, "Applications of electrical impedance tomography (EIT): a short review," in *IOP Conference Series: Materials Science and Engineering*, 2018, vol. 331, no. 1: IOP Publishing, p. 012004.

[58] L. Cao *et al.*, "Real-time imaging of infarction deterioration after ischemic stroke in rats using electrical impedance tomography," *Physiological Measurement,* vol. 41, no. 1, p. 015004, 2020.

[59] M. Faulkner, S. Hannan, K. Aristovich, J. Avery, and D. Holder, "Feasibility of imaging evoked activity throughout the rat brain using electrical impedance tomography," *Neuroimage,* vol. 178, pp. 1-10, 2018.

[60] X. Shi *et al.*, "High-precision electrical impedance tomography data acquisition system for brain imaging," *IEEE Sensors Journal,* vol. 18, no. 14, pp. 5974-5984, 2018.

[61] S. Mansouri, Y. Alharbi, F. Haddad, S. Chabcoub, A. Alshrouf, and A. A. Abd-Elghany, "Electrical Impedance tomography–recent applications and developments," *Journal of Electrical Bioimpedance,* vol. 12, no. 1, pp. 50-62, 2021.

[62] N. M. Zain and K. K. Chelliah, "Breast imaging using electrical impedance tomography: correlation of quantitative assessment with visual interpretation," *Asian Pacific Journal of Cancer Prevention,* vol. 15, no. 3, pp. 1327-1331, 2014.

[63] W. Yin and Y. Xie, "Biomedical Sensing and Imaging," 2021.

[64] X. Bai, D. Liu, J. Wei, X. Bai, S. Sun, and W. Tian, "Simultaneous Imaging of Bio-and Non-Conductive Targets by Combining Frequency and Time Difference Imaging Methods in Electrical Impedance Tomography," *Biosensors,* vol. 11, no. 6, p. 176, 2021.

[65] T. Meier *et al.*, "Assessment of regional lung recruitment and derecruitment during a PEEP trial based on electrical impedance tomography," *Intensive care medicine,* vol. 34, no. 3, pp. 543-550, 2008.

[66] C. Zhang *et al.*, "Global and regional degree of obstruction determined by electrical impedance tomography in patients with obstructive ventilatory defect," *Plos one,* vol. 13, no. 12, p. e0209473, 2018.

[67] F. Braun, M. Proença, A. Adler, T. Riedel, J.-P. Thiran, and J. Solà, "Accuracy and reliability of noninvasive stroke volume monitoring via ECG-gated 3D electrical impedance tomography in healthy volunteers," *PloS one,* vol. 13, no. 1, p. e0191870, 2018.

[68] M. Graf and T. Riedel, "Electrical impedance tomography: Amplitudes of cardiac related impedance changes in the lung are highly position dependent," *PLoS One,* vol. 12, no. 11, p. e0188313, 2017.

[69] S. Mansouri, "Determination of cardiac output by peripheral electrical bioimpedance," *IEEJ Transactions on Electrical and Electronic Engineering,* vol. 15, no. 9, pp. 1321-1326, 2020.

[70] R. Pikkemaat, S. Lundin, O. Stenqvist, R.-D. Hilgers, and S. Leonhardt, "Recent advances in and limitations of cardiac output monitoring by means of electrical impedance tomography," *Anesthesia & Analgesia,* vol. 119, no. 1, pp. 76-83, 2014.

[71] C. Putensen, B. Hentze, S. Muenster, and T. Muders, "Electrical impedance tomography for cardio-pulmonary monitoring," *Journal of clinical medicine,* vol. 8, no. 8, p. 1176, 2019.

[72] Pulmotrace. https://www.crunchbase.com/organization/pulmotrace (accessed Aug. 01, 2021.

[73] H. Harmon. "CardioInspect Diagnostic and Monitoring Systems." https://slideplayer.com/slide/9270570/ (accessed Aug. 01, 2021.

[74] R. J. Halter *et al.*, "Real-time electrical impedance variations in women with and without breast cancer," *IEEE transactions on medical imaging,* vol. 34, no. 1, pp. 38-48, 2014.

[75] D. Haemmerich, S. T. Staelin, J.-Z. Tsai, S. Tungjitkusolmun, D. M. Mahvi, and J. G. Webster, "In vivo electrical conductivity of hepatic tumours," *Physiological measurement,* vol. 24, no. 2, p. 251, 2003.

[76] S. Hong *et al.*, "A 4.9 mΩ-Sensitivity Mobile Electrical Impedance Tomography IC for Early Breast-Cancer Detection System," *IEEE journal of solid-state circuits,* vol. 50, no. 1, pp. 245-257, 2015.

[77] S. Mansouri, T. Alhadidi, and M. Ben Azouz, "Breast Cancer Detection Using Low-Frequency Bioimpedance Device," *Breast cancer targets and therapy,* vol. 12, pp. 109-116, 2020.

[78] R. Poni, E. Neufeld, M. Capstick, S. Bodis, T. Samaras, and N. Kuster, "Feasibility of Temperature Control by Electrical Impedance Tomography in Hyperthermia," *Cancers,* vol. 13, no. 13, p. 3297, 2021.

[79] B. H. Brown, "Electrical impedance tomography (EIT): a review," *Journal of medical engineering & technology,* vol. 27, no. 3, pp. 97-108, 2003.

[80] Y. Shi, Z. Yang, F. Xie, S. Ren, and S. Xu, "The research progress of electrical impedance tomography for lung monitoring," *Frontiers in Bioengineering and Biotechnology,* vol. 9, 2021.

[81] B. Gong, S. Krueger-Ziolek, K. Moeller, B. Schullcke, and Z. Zhao, "Electrical impedance tomography: functional lung imaging on its way to clinical practice?," *Expert review of respiratory medicine,* vol. 9, no. 6, pp. 721-737, 2015.

[82] A. Zifan, P. Liatsis, and H. Almarzouqi, "Realistic forward and inverse model mesh generation for rapid three-dimensional thoracic electrical impedance imaging," *Computers in Biology and Medicine,* vol. 107, pp. 97-108, 2019.

[83] D. Liu, D. Gu, D. Smyl, J. Deng, and J. Du, "Shape reconstruction using Boolean operations in electrical impedance tomography," *IEEE transactions on medical imaging,* vol. 39, no. 9, pp. 2954-2964, 2020.

[84] Y. Wu *et al.*, "Shape reconstruction with multiphase conductivity for electrical impedance tomography using improved convolutional neural network method," *IEEE sensors journal,* vol. 21, no. 7, pp. 9277-9287, 2021.

[85] E. E. B. Adam and E. Babikir, "Survey on medical imaging of electrical impedance tomography (EIT) by variable current pattern methods," *Journal of ISMAC,* vol. 3, no. 02, pp. 82-95, 2021.

[86] J. Wagenaar and A. Adler, "Electrical impedance tomography in 3D using two electrode planes: characterization and evaluation," *Physiological measurement,* vol. 37, no. 6, p. 922, 2016.

[87] X. Li *et al.*, "Electrical-impedance-tomography imaging based on a new three-dimensional thorax model for assessing the extent of lung injury," *AIP Advances,* vol. 9, no. 12, p. 125310, 2019.

[88] N. Huang, Y. Ma, M. Zhang, H. Ge, and H. Wu, "Finite element modeling of human thorax based on MRI images for EIT image reconstruction," *Journal of Shanghai Jiaotong University (Science),* vol. 26, no. 1, pp. 33-39, 2021.

[89] T.-J. Kao, B. Amm, D. Isaacson, J. Newell, G. Saulnier, and J. L. Mueller, "A 3D Reconstruction Algorithm for Real-time Simultaneous Multi-Source EIT Imaging for Lung Function Monitoring," *bioRxiv,* 2020.

[90] G. Ye, K. H. Lim, R. George, G. Ybarra, W. T. Joines, and Q. H. Liu, "A 3D EIT system for breast cancer imaging," in *3rd IEEE International Symposium on Biomedical Imaging: Nano to Macro, 2006.*, 2006: IEEE, pp. 1092-1095.

[91] D. P. Riley, S. L. Henke, P. J. Lennon, and K. Aston, "Computer-aided design (CAD) of synzymes: use of molecular mechanics (MM) for the rational design of superoxide dismutase mimics," *Inorganic chemistry,* vol. 38, no. 8, pp. 1908-1917, 1999.

[92] J. E. Akin, *Finite element analysis concepts: via SolidWorks*. World Scientific, 2010.

[93] C. Gabriel, A. Peyman, and E. H. Grant, "Electrical conductivity of tissue at frequencies below 1 MHz," *Physics in medicine & biology,* vol. 54, no. 16, p. 4863, 2009.

[94] R. Kohn and M. Vogelius, "Determining conductivity by boundary measurements," *Communications on pure and applied mathematics,* vol. 37, no. 3, pp. 289-298, 1984.

[95] J. Lehr, "A vector derivation useful in impedance plethysmographic field calculations," *IEEE Transactions on Biomedical Engineering,* no. 2, pp. 156-157, 1972.

[96] M. Brühl and M. Hanke, "Numerical implementation of two noniterative methods for locating inclusions by impedance tomography," *Inverse Problems,* vol. 16, no. 4, p. 1029, 2000.

[97] M. Vauhkonen, D. Vadász, P. A. Karjalainen, E. Somersalo, and J. P. Kaipio, "Tikhonov regularization and prior information in electrical impedance tomography," *IEEE transactions on medical imaging,* vol. 17, no. 2, pp. 285-293, 1998.

[98] P. C. Hansen, *Discrete inverse problems: insight and algorithms*. SIAM, 2010.

[99] Q. Dai and W. Sha, "The physics of compressive sensing and the gradient-based recovery algorithms," *arXiv preprint arXiv:0906.1487,* 2009.

[100] H. C. Elman, *Iterative methods for large, sparse, nonsymmetric systems of linear equations*. Yale University, 1982.

[101] M. Wang, "Inverse solutions for electrical impedance tomography based on conjugate gradients methods," *Measurement Science and Technology,* vol. 13, no. 1, p. 101, 2001.

[102] S. Liu, J. Jia, Y. D. Zhang, and Y. Yang, "Image reconstruction in electrical impedance tomography based on structure-aware sparse Bayesian learning," *IEEE transactions on medical imaging,* vol. 37, no. 9, pp. 2090-2102, 2018.

[103] S. Pulletz *et al.*, "Comparison of different methods to define regions of interest for evaluation of regional lung ventilation by EIT," *Physiological measurement,* vol. 27, no. 5, p. S115, 2006.

[104] M. P. Sampat, Z. Wang, S. Gupta, A. C. Bovik, and M. K. Markey, "Complex wavelet structural similarity: A new image similarity index," *IEEE transactions on image processing,* vol. 18, no. 11, pp. 2385-2401, 2009.

[105] A. Hore and D. Ziou, "Image quality metrics: PSNR vs. SSIM," in *2010 20th international conference on pattern recognition*, 2010: IEEE, pp. 2366-2369.

[106] S. Ahn, T. I. Oh, S. C. Jun, J. K. Seo, and E. J. Woo, "Validation of weighted frequency-difference EIT using a three-dimensional hemisphere model and phantom," *Physiological measurement,* vol. 32, no. 10, p. 1663, 2011.

[107] L. Borcea, "Electrical impedance tomography," *Inverse problems,* vol. 18, no. 6, p. R99, 2002.

[108] I. Frerichs *et al.*, "Regional lung perfusion as determined by electrical impedance tomography in comparison with electron beam CT imaging," *IEEE transactions on medical imaging,* vol. 21, no. 6, pp. 646-652, 2002.

[109] J. Kuen, E. J. Woo, and J. K. Seo, "Multi-frequency time-difference complex conductivity imaging of canine and human lungs using the KHU Mark1 EIT system," *Physiological measurement,* vol. 30, no. 6, p. S149, 2009.

[110] H. J. Smit, A. Vonk Noordegraaf, J. T. Marcus, A. Boonstra, P. M. de Vries, and P. E. Postmus, "Determinants of pulmonary perfusion measured by electrical impedance tomography," *European journal of applied physiology,* vol. 92, no. 1, pp. 45-49, 2004.

[111] Z. Wei, D. Liu, and X. Chen, "Dominant-current deep learning scheme for electrical impedance tomography," *IEEE Transactions on Biomedical Engineering,* vol. 66, no. 9, pp. 2546-2555, 2019.

[112] Z. Liu and Y. Yang, "Multimodal Image Reconstruction of Electrical Impedance Tomography Using Kernel Method," *IEEE Transactions on Instrumentation and Measurement,* vol. 71, pp. 1-12, 2021.

[113] G. Alessandrini and S. Vessella, "Lipschitz stability for the inverse conductivity problem," *Advances in Applied Mathematics,* vol. 35, no. 2, pp. 207-241, 2005.

[114] D. Liu, V. Kolehmainen, S. Siltanen, A.-M. Laukkanen, and A. Seppänen, "Nonlinear difference imaging approach to three-dimensional electrical impedance tomography in the presence of

geometric modeling errors," *IEEE Transactions on Biomedical Engineering,* vol. 63, no. 9, pp. 1956-1965, 2015.

[115] X. Zhang *et al.*, "V-Shaped Dense Denoising Convolutional Neural Network for Electrical Impedance Tomography," *IEEE Transactions on Instrumentation and Measurement,* vol. 71, pp. 1-14, 2022.

[116] T. A. Khan and S. H. Ling, "Review on electrical impedance tomography: Artificial intelligence methods and its applications," *Algorithms,* vol. 12, no. 5, p. 88, 2019.

[117] J. K. Seo, K. C. Kim, A. Jargal, K. Lee, and B. Harrach, "A learning-based method for solving ill-posed nonlinear inverse problems: a simulation study of lung EIT," *SIAM journal on Imaging Sciences,* vol. 12, no. 3, pp. 1275-1295, 2019.

[118] C. Zhu, B. Wang, L. Li, and T. Li, "Deep Learning-Based CT Images in Pulmonary Function Assessment of Patients Who Underwent Laparoscopic Surgery under Guidance of Electrical Impedance Tomography," *Scientific Programming,* vol. 2021, 2021.

[119] Y.-F. Ko and K.-S. Cheng, "U-Net-based approach for automatic lung segmentation in electrical impedance tomography," *Physiological Measurement,* vol. 42, no. 2, p. 025002, 2021.

[120] K. Lee, M. Yoo, A. Jargal, and H. Kwon, "Electrical impedance tomography-based abdominal subcutaneous fat estimation method using deep learning," *Computational and Mathematical Methods in Medicine,* vol. 2020, 2020.

[121] S. Wang *et al.*, "Predicting EGFR mutation status in lung adenocarcinoma on computed tomography image using deep learning," *European Respiratory Journal,* vol. 53, no. 3, 2019.

[122] S. Liu, H. Wu, Y. Huang, Y. Yang, and J. Jia, "Accelerated structure-aware sparse Bayesian learning for three-dimensional electrical impedance tomography," *Ieee transactions on industrial informatics,* vol. 15, no. 9, pp. 5033-5041, 2019.

[123] H. Polat and H. Danaei Mehr, "Classification of pulmonary CT images by using hybrid 3D-deep convolutional neural network architecture," *Applied Sciences,* vol. 9, no. 5, p. 940, 2019.

[124] N. Siddique, S. Paheding, C. P. Elkin, and V. Devabhaktuni, "U-net and its variants for medical image segmentation: A review of theory and applications," *Ieee Access,* vol. 9, pp. 82031-82057, 2021.

[125] Z. Zeng, W. Xie, Y. Zhang, and Y. Lu, "RIC-Unet: An improved neural network based on Unet for nuclei segmentation in histology images," *Ieee Access,* vol. 7, pp. 21420-21428, 2019.

[126] S. Guan, A. A. Khan, S. Sikdar, and P. V. Chitnis, "Fully dense UNet for 2-D sparse photoacoustic tomography artifact removal," *IEEE journal of biomedical and health informatics,* vol. 24, no. 2, pp. 568-576, 2019.

[127] H. Huang *et al.*, "Unet 3+: A full-scale connected unet for medical image segmentation," in *ICASSP 2020-2020 IEEE International Conference on Acoustics, Speech and Signal Processing (ICASSP)*, 2020: IEEE, pp. 1055-1059.

[128] H. Cao *et al.*, "Swin-unet: Unet-like pure transformer for medical image segmentation," *arXiv preprint arXiv:2105.05537,* 2021.

[129] O. Ronneberger, P. Fischer, and T. Brox, "U-net: Convolutional networks for biomedical image segmentation," in *International Conference on Medical image computing and computer-assisted intervention*, 2015: Springer, pp. 234-241.

[130] G. Ye, J. Zhang, H. Li, Z. Tang, and T. Lv, "Android Malware Detection Technology Based on Lightweight Convolutional Neural Networks," *Security and Communication Networks,* vol. 2022, 2022.

[131] X. He, "Improved Music Recommendation Algorithm for Deep Neural Network Based on Attention Mechanism," *Mobile Information Systems,* vol. 2022, 2022.

[132] X. Ding, X. Zhang, N. Ma, J. Han, G. Ding, and J. Sun, "Repvgg: Making vgg-style convnets great again," in *Proceedings of the IEEE/CVF Conference on Computer Vision and Pattern Recognition*, 2021, pp. 13733-13742.

[133] H. Zhu and K. Moller, "Ventilator control based on a fuzzy-neural network approach," in *2008 2nd International Conference on Bioinformatics and Biomedical Engineering*, 2008: IEEE, pp. 747-750.

[134] R. L. Dellaca and C. Veneroni, "Trends in mechanical ventilation: are we ventilating our patients in the best possible way?," *Breathe,* vol. 13, no. 2, pp. 84-98, 2017.

[135] M. A. Denaï, M. Mahfouf, S. Mohamad-Samuri, G. Panoutsos, B. H. Brown, and G. H. Mills, "Absolute electrical impedance tomography (aEIT) guided ventilation therapy in critical care patients: simulations and future trends," *IEEE Transactions on Information Technology in Biomedicine,* vol. 14, no. 3, pp. 641-649, 2009.

[136] M. C. Bachmann *et al.*, "Electrical impedance tomography in acute respiratory distress syndrome," *Critical Care,* vol. 22, no. 1, pp. 1-11, 2018.

[137] E. Santangelo, S. Mongodi, B. Bouhemad, and F. Mojoli, "The weaning from mechanical ventilation: a comprehensive ultrasound approach," *Current Opinion in Critical Care,* vol. 28, no. 3, pp. 322-330, 2022.

[138] G. Bellani *et al.*, "Epidemiology, patterns of care, and mortality for patients with acute respiratory distress syndrome in intensive care units in 50 countries," *Jama,* vol. 315, no. 8, pp. 788-800, 2016.

[139] N. A. Rodríguez-Olivares, L. Nava-Balanzar, and L. Barriga-Rodríguez, "Differential Pressure Spirometry for Mechanical Ventilation Using Dichotomic Search," *IEEE Transactions on Instrumentation and Measurement,* vol. 70, pp. 1-10, 2021.

[140] B. J. Smith and J. H. Bates, "Assessing the progression of ventilator-induced lung injury in mice," *IEEE Transactions on Biomedical Engineering,* vol. 60, no. 12, pp. 3449-3457, 2013.

[141] G. Y. Jang *et al.*, "Real-Time Measurements of Relative Tidal Volume and Stroke Volume Using Electrical Impedance Tomography with Spatial Filters: A Feasibility Study in a Swine Model Under Normal and Reduced Ventilation," *Annals of Biomedical Engineering,* pp. 1-16, 2022.

[142] Z. Gao, "Scaling and bandwidth-parameterization based controller tuning," in *ACC*, 2003: Citeseer, pp. 4989-4996.

[143] E. Fresnel, J.-F. Muir, and C. Letellier, "Realistic human muscle pressure for driving a mechanical lung," *EPJ Nonlinear Biomedical Physics,* vol. 2, pp. 1-18, 2014.

[144] D. Papandrinopoulou, V. Tzouda, and G. Tsoukalas, "Lung compliance and chronic obstructive pulmonary disease," *Pulmonary medicine,* vol. 2012, 2012.